MINISTRY OF EDUCATION AND RESEARCH

TECHNICAL UNIVERSITY
OF CLUJ-NAPOCA, ROMANIA

FACULTY OF ELECTRICAL ENGINEERING

PhD THESIS

Synchronous Reluctance Machine for automotive applications

PhD Student:
Florin-Adelin Pop-Pîgleşan

PhD Supervisor:
Prof. Dr. Eng. Claudia Steluța Marțiş

Examination committee:

Chair: Prof. Eng. **Teodor Pană** PhD – Technical University of Cluj-Napoca;
PhD Supervisor: Prof. Eng. **Claudia S. Marțiş**, PhD – Technical University of Cluj-Napoca;

Members:

-Prof. Eng. **Elena A. Lomonova**, PhD – Eindhoven University of Technology
-Prof. Eng. **Leonard Livadaru**, PhD – Technical University of Iasi
-Prof. Eng. **Lorand Szabo**, PhD – Technical University of Cluj-Napoca

– Cluj-Napoca –
2020

AKNOWLEDGEMENT

This research was supported by the European Commission under the "Optimal Low-Noise Energy-Efficient Electrical Machines and Drives for Automotive Applications (EMDA_LoOP)" project which is an EU funded Marie Curie FP7-PEOPLE-2012_IAPP project (Industry Academia Partnerships and Pathways)

EMDA_LOOP

OPTIMAL LOW-NOISE ENERGY-EFFICIENT ELECTRICAL MACHINES AND DRIVES
FOR AUTOMOTIVE APPLICATIONS

ACKNOWLEDGMENTS

I would like to express my sincere gratitude to my scientific advisor prof. Claudia Marțiş for her support and continuous help. Her knowledge, invaluable guidance, understanding and patience helped me accomplish my thesis.

A significant part of my research was performed at *Brose Fahrzeugteile GmbH & Co* in Würzburg, Germany. I would like to thank Matthias Koch, the head of Advanced Development Department, for giving me the opportunity to work on interesting topics in the company.

I would like to express my gratitude to dr. Ioana Vintiloiu for her advice support and technical help. Also, for supporting my participation at seminars and trainings.

I would like to express my special appreciation and thanks to dr. Adrian-Cornel Pop, mentor and friend. I would like to thank him for encouraging my research and for allowing me to grow as a researcher, as an engineer and as person. His advice on my research as well as on my career has been priceless.

A special thank goes to my fellow colleagues and friends, Tiberiu Rusu, Sorin Cosman and Radu Marțiş for their support and for the beautiful time spent together that made this experience unforgettable. I honor their friendship and so many good memories.

I would like to extend my sincere appreciation to my beloved family, my parents and my sister Larisa for their patience, care and endless devotion.

Last but certainly not the least, I do not have the words to express my gratitude to my beloved fiancée Monalisa Pop, for her support, love and patience. As well as to my friends, Şerban Ursu, Daniel Şildan and Andreea Şildan for their support and encouragement that inspired me to be strong and to succeeded.

TABLE OF CONTENTS

ABBREVIATIONS 9
INTRODUCTION 11
MOTIVATION AND OBJECTIVES 14
THESIS ORGANIZATION 15
1. Automotive Electrification 17
  1.1. Electrical machines on board in automotive industry 17
  1.2. Synchronous Reluctance Machine 21
    1.2.1. State of the art 21
    1.2.2 SynRM for automotive – possible applications 24
  1.3. Conclusions 34
2. SynRM – an Overview 35
  2.1 SynRM – an Overview 35
  2.2. SynRM - equivalent circuit and mathematical model 36
  2.3. SynRM – design issues 41
    2.3.1. Guidelines for slot pole selection 41
    2.3.2. Winding technology 43
  2.4 Rotor Topologies 48
  2.5 Multiphysics design and optimization 50
  2.6 Conclusions 52
3. Electromagnetic Analysis 53
  3.1. One barrier design proposal 53
  3.2. Multi-barriers effect 59
  3.3. Workflow and reference machine 60
  3.4 Design of SynRM with concentrated windings 62
    3.4.1. Torque performances of the proposed SynRM with CW 67
    3.4.2. Inductances computation and saturation effect 69

3.4.3. Iron and copper losses 70
3.5. SynRM design with distributed windings..72
3.5.1. Torque performances of the proposed SynRM with DW....74
3.5.2 Inductances computation and saturation effect 77
3.5.3 Iron and copper losses 78
3.6 Performance comparison..79
3.7 Best design assessment further investigation 80
3.7.1. Re-optimization process 81
3.7.2. Key performance indicators 84
3.7.3 Comparison between 2D and 3D design..85
3.7.4. Active material cost and weight..88
3.8 Conclusions..89
4. Structural and vibroacoustic analysis of SynRM 91
4.1 Rotor dynamic calculation..92
4.3 Stator analysis - NVH behavior..95
4.3.1 Numerical Results 96
4.3.2 Experimental results..98
4.5 Conclusions..102
5. Experimental validation..103
5.1 Prototype – Fabrication and Assembly..103
5.2 Test bench layout..105
5.3 Results of the measurements 108
5.3.1 Key performance measurements..108
5.3.2 Vibroacoustic measurements..114
5.4 Conclusions..124
6. Final conclusions, contributions and future work 125
6.1 Final conclusions..125
6.2 Personal contribution..126

6.3 Future Work ... 127

REFERENCES ... 128

LIST OF FIGURES ... 139
LIST OF TABLES ... 145
APPENDICES ... 147
A. Parametric 2D FEM and optimization process ... 147

LIST OF PUBLICATIONS ... 156

ABBREVIATIONS

2D	Two dimensional
3D	Three dimensional
ABS	Anti-lock braking system
AFM	Axial flux machine
BBW	Brake-by-wire
CAD	Computer aided design
CFM	Cooling fan application
DC	Direct current
EV	Electric vehicle
ESP	Electric power steering
FEA	Finite element analysis
FEM	Finite element method
FMSC	Fiber Soft magnetic composites
GUI	Graphical user interface
HEV	Hybrid electric vehicle
HVAC	Heat, ventilation air conditioning
ICE	Internal combustion engine
MUT	Machine under test
NHV	Noise, harshness and vibration
PM	Permanent magnet
PMSM	Permanent magnet synchronous motor
PWM	Pulse width modulation
RMS	Root mean square
RTI	Real time interface
SPL	Sound pressure level
SM	Synchronous Motor
SRM	Switched reluctance machine
SynRM	Synchronous reluctance machine

INTRODUCTION

Even though it is often considered as a brand-new innovation, the idea to power vehicles with electric energy has a long history. According to the speech held in 1897 in Berlin, Germany by chief engineer Adolf Klose, the visionary president of the central European Motor Association, "among motor vehicles that carry the energy required for locomotion on board, three categories can currently be identified: engines driven by steam, engines driven by oil, and engines driven by electricity (…) while oil-powered engines will journey across the lands at high speeds (…) in major cities will be travelled accumulator-powered electric vehicles " [1], one can say that more than half a way is already gone, as following the steam engine disappearance, both oil-based technologies (i.e. gasoline and diesel) are losing terrain to the electrical one. According to a report of the International Energy Agency (IEA), until 2015, United States dominated the global electric car stock. In 2016, China overtook U.S. and became the country with the largest electric car stock, with a third of the global market [2]. Every year, when the Geneva International Motor Show opens, most of the world's biggest car manufactures are presenting their latest designs and concepts to the public. There are currently three million e-vehicles on the streets all around the globe with a continuous raise year after year, see Fig.1. Despite the fact that in the early years of the vehicle there seems to be a race between these later two propulsion technologies (i.e. electric and oil), ultimately oil-based ones won and established themselves as driving technology (over the next century), thanks to the significant higher energy density of gasoline in comparison with electricity obtain from batteries. Deservedly, the internal combustion engine proved to offer a higher flexibility and freedom-like feeling to the driver, and since then, the internal combustion engines (ICE) have dominated the market in terms of propulsion and his dominance is far away from being over. The transportation sector is the largest energy consumer in U.S., and yet 93% of the energy is based in fossil fuels [3]. Furthermore, this situation is not particular for U.S., similar numbers being reported all over the world. Thanks to the new technological improvements [4] ICE is being continuously improved, but simultaneously over the last two decades' important progresses are made in terms of electrification on the road transport [5], [6].

Global warming/climate change promoters focused primarily on the Carbon dioxide (CO_2) emissions as it is the main contributor to the greenhouse effect, however the combustion of hydrocarbon fuels produces several byproducts such as nitrogen oxides (NO_x), carbon monoxide (CO), sulfur dioxide (SO_x), methane (CH_4), nitrous oxide (N_2O), chlorofluorocarbons (CFC), perfluorocarbons (PFC), unburned particles HCs (benzene) and other heavy metals (zinc, chrome, copper, cadmium) [7], which are directly affecting the human health [8], [9]. In order to reduce the impact of vehicle emissions on both environmental and human health, European Union and United States have established a legislation on the maximum allowed emissions over the time. In spite of this legislation, there are other requirements for vehicle manufactures, which might include amongst others safety and roadworthiness of vehicles, environmentally safe treatment of vehicles at the end of their life, avoiding the use of hazardous or environmentally harmful materials in vehicles [10].

Another fundamental problem arises from the shrinking oil reserves Every year oil industry is producing more than it did the year before. According to the world trend of the oil consumption, it is expected that the oil resources to be depleted in the next 50-60 years [11]. Due to continuously increasing life standards, some tens of millions of cars are manufactured and sold yearly [12]. It is now clear that to prevent the climate change, the next generation of cars needs to be more environmentally friendly. According to this principle, a new race rises again – it is time for automotive electrification. Obviously, Klose was some steps ahead of his time, as 120 years of technological evolution were needed for his dream to come true, i.e. to have mass production electric cars (Tesla Cars) [13]. Nowadays, besides Tesla, the well-established automotive companies such as Toyota, BMW, Nissan, Renault etc., embraced this idea and thanks to huge investments and high-quality research, progress is made daily. As the electrical energy storage systems are still under the customer expectations, the transition from the conventional ICE to pure EV is done gradually, where different degrees of electrification (DOE), which lies between 0 and 1, are employed. This is defined as the ratio between the electric traction motor power and total motor power (combustion and electric) [14]. According to this ratio, electrical vehicles are classified [15] as follows:

  - Hybrid EVs (HEVs), DOE<1, they can be further differentiated in:
    - Conventional Hybrids, where the propulsion system comprises an ICE and an electric drive. The purpose of the electric drive is to achieve a better fuel efficiency or higher performances, e.g. acceleration times.
    - Plug-In Hybrid Vehicles (PHEVs): are a type of hybrid electric vehicle that use rechargeable batteries or another storage device. The batteries can be recharged by plugging them to an external source of electric power.
  - Battery EVs (BEVs) with DOE =1. They use as power sources only rechargeable battery packs and thus have no ICE for propulsion.

Fuel Cell EVs (FCEVs) with DOE =1. In terms of propulsion system, they are similar to BEVs, but their source of electrical energy differs as such an electric vehicle uses fuel cells (FCs), instead of batteries. The electrical energy is provided by means of a chemical reaction between hydrogen and oxygen, which produces the used energy (for propulsion) and water (non-polluting chemical by-product), thus the increased attractiveness of this technology.

MOTIVATION AND OBJECTIVES

Technological innovations in automotive industry trigger new developments in electric machines technology. Many electric drive systems have been developed for automotive applications [16], [17], traditionally for auxiliaries and recently for traction applications. As in a vehicle there are so many tough requirements, motors used for automotive applications should fulfill various conflicting requirements (i.e. high torque and power density, wide speed range, good torque quality and increased robustness). Several types of electric motors, the vast majority in radial flux configuration, are used in this industry depending on the application: Induction Machines (for traction, used in Tesla vehicles), Switched Reluctance Machines (used for high-speed applications such as turbocharging), brushed-DC Machines (used in applications demanding very low-power such as window lifters or various seat adjusters) and the most common type, Permanent Magnet Synchronous Machines (PMSMs). Their choice is generally imposed by three important factors: cost, weight and size [18], [19], at given torque and speed requirements as well as input power specifications. For high performance applications, PM-based synchronous machine represents main choice. This arises mainly because of the high torque density required by a drive used in such applications. Despite their attractiveness in this field, the limited availability and problems associated with the exploitation of rare earth permanent magnets, inherently imply higher cost of the PM-based machines [19], [20]. For these reasons and thanks to the development of new materials and concepts, PM-less motor topologies such as **Synchronous Reluctance Motors** (SynRMs) are perceived as a promising alternative.

This thesis deals with the designing, modeling, optimization, control and experimental testing for vehicle auxiliaries in general and for a cooling fan drive. The objective of this thesis is to contribute to the development of a SynRM based drive system for low power automotive applications.

THESIS ORGANIZATION

The thesis is structured in 6 chapters, which are briefly described below:

Chapter 1 presents an overview of an electrical vehicle architecture, highlighting different motors auxiliary electrical drive system. The key requirements and several specifications for such applications are highlighted. It also presents the state of the art of SynRM. In addition, the possibility of using SynRM in electric vehicles by pointing out the advantages and the main drawbacks of the motor drive system based on SynRM are described.

Chapter 2 is taking SynRM into study. The operating principle, a brief history and the standard machine equivalent circuit and mathematical model together with common figures of merit are presented. Guidelines for slot pole selection, winding configuration and topologies for performance improvements for SynRM are described.

Chapter 3 presents an investigation around a suitable barrier shape design by means of the finite element method (FEM). Different rotor topologies with one or multi-barrier design are taken into study. Different principles of designing the flux barriers shape and rotor topology are derived. A comparative study between all chosen topologies is done by means of FE-based electromagnetic analyses in order to evaluate their key-performance indicators, i.e. power to weight ratio, average torque and torque ripple as well as their speed-torque (and -efficiency, respectively) characteristics, while keeping the outer diameter fixed (installation space constraint). Finally, based on the obtained results, two SynRM were chosen to be experimentally developed.

Chapter 4 details the mechanical analysis of the motor parts (rotor and stator). For the rotor, a FE-based structural analysis is carried out using ANSYS Workbench, in order to evaluate the mechanical stress at maximum speed and over speed (double maximum speed). The rotor stress, deformation and safety factor are calculated in this section for each rotor design. Furthermore, typical natural modes of the stator core of both prototyped machines by means of FE analysis and experimental measurements are shown.

Chapter 5 is focused on the laboratory testing of the developed SynRM experimental models and the reference PMSM machine, by means of real-time control concept implemented on the test bench. Electromagnetic and vibroacoustic measurements were performed. Additionally, the reference PMSM machine is tested under the same conditions. It is mandatory to perform these tests in order to validate the functionality of the developed products.

Chapter 6 concludes the work in this thesis and sets the scene for future work research in this area. Personal contribution of the author is also described.

1. Automotive Electrification

1.1. Electrical machines on board in automotive industry

Traditionally, the vehicles were equipped mainly with mechanical systems. Electricity was limited to systems such as ignition, headlights and starting functions [21]. Historically, the earliest electronic system arises in 1950 with the introduction of the car radio, followed in 1955 with the first transistorized ignition system and then later on, the first on-board controllers and computers being introduced in the 1970s. Despite the very shy beginnings, some decades later everything changed in an exponential manner (see Fig. 1.1), all culminating in the current times (2018-2019) where a premium car can have more than 100 small and medium sized electrical motors (excluding traction) and millions of lines of code [22]. Obviously, the number of auxiliary motors per car depends on the type of comfort that the customer expects as well as on the type of expected automation/robotics level. The latter is easily justified when one thinks towards autonomous driving [23].

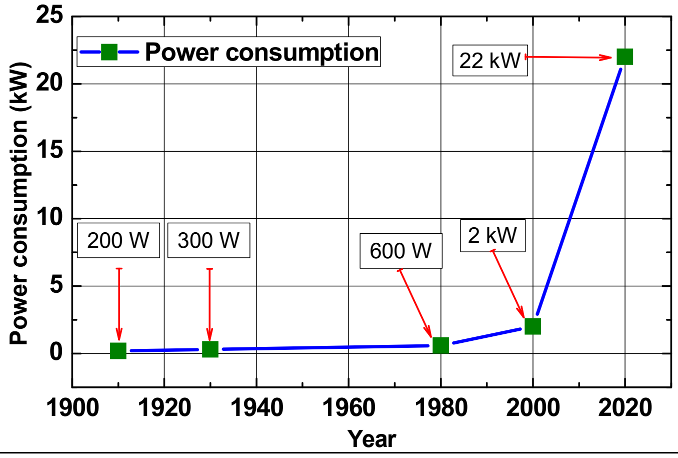

Fig. 1.1 The auxiliaries power consumptions in common automobiles

In Fig. 1.2 it can be seen the typical architecture of the electric system of a vehicle, highlighting different motors, which can be divided in two main groups:

- Traction motors
- Auxiliary motors, which power or assist the auxiliary mechanical systems of a vehicle. They are normally low torque/power electrical machines, fed with energy from the battery through a DC-bus (commonly 12V, with increasing electrification/hybridization also other systems are currently under investigation). Obviously, the electronically commutated AC motors will require an inverter. A short classification of the most common electrical machines-based systems and their role is summarized as follows:
    - Electric Power Steering (EPS) – assists the steering action
    - Air Conditioning (HVAC) – Heating, Ventilation and Air-Conditioning
    - Anti-lock Braking System (ABS) – brake assistance
    - Cooling Fan Module (CFM) – for combustion engine cooling
    - Vacuum Pumps – used for pneumatic accessories
    - Mirrors, sits and windows regulators
    - Turbochargers - increases an internal combustion engine's efficiency and power output

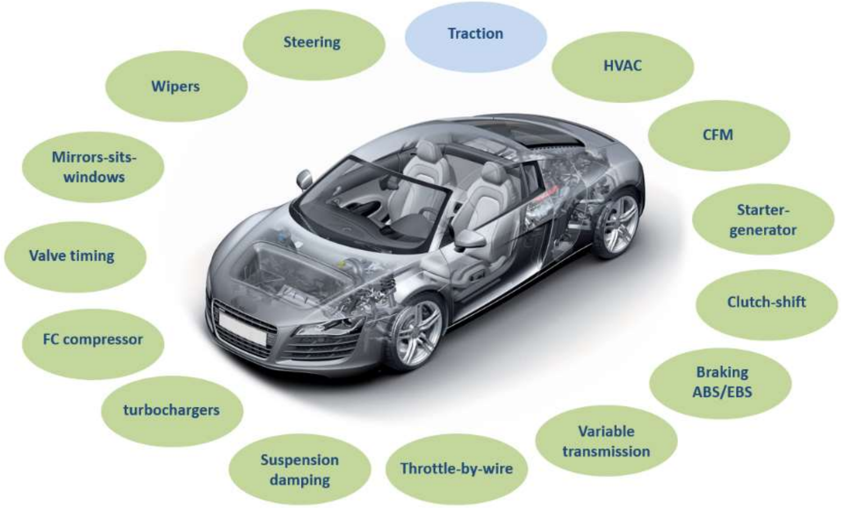

Fig. 1.2 Overview of automotive electric drives application [112]

As in a vehicle there are so many tough requirements, the electrical motors used for automotive applications should fulfil various contradictory specifications like:

- High torque and power density;
- Wide speed range;
- High efficiency over a wide torque-speed range;
- High robustness and reliability due the harsh condition of the vehicle environment (e.g. operation in oil for oil pump motors or environmental factors);
- Good torque quality (e.g. low torque ripple for all motors and low cogging torque for PM-based ones);
- Good thermal and acoustic behavior;
- Low weight, a crucial requirement to save mass, thus improving fuel consumption;
- Low cost (manufacturing and active materials).

Several types of electric motors are used in automotive applications such as: Induction Machines (e.g. for traction, used in Tesla cars), Switched Reluctance Machines (SRMs), Brushed-DC Machines and Permanent Magnet Synchronous machines (PMSM). The latter are the most popular due to their high-performance indicators and therefore they are preferred for both traction and auxiliary applications [18]. All these machines have advantages and disadvantages (see TABLE 1.1) of their own which render them interesting in different automotive applications.

TABLE 1.1 Machine technologies comparison

	DC	IM	PMSM	SRM	SynRM	Legend
Power density	⊖⊖	⊙	⊕⊕	⊙	⊙	⊕⊕ - very good
Efficiency	⊖	⊕	⊕⊕	⊕	⊕	⊕- good
Costs	⊕	⊕⊕	⊖	⊕	⊕⊕	⊙- neutral
Reliability	⊖	⊕⊕	⊙	⊕	⊕⊕	⊖- bad
Technical maturity	⊕	⊕	⊙	⊙	⊙	⊖⊖ - very bad
Control & costs	⊕⊕	⊙	⊕	⊖	⊙	

For many years auxiliary and traction systems were based on **DC machines** due to several advantages like; simplicity, good technical maturity at low cost and the simple and cheap control system. In spite of this advantage, these machines exhibit some drawbacks linked to the mechanical commutation. Therefore, they have insufficient reliability and require constant maintenance. Due to this, it offers the lowest power density and efficiency. Thanks to advancements in power electronics and microprocessors technology as well as the evolution in manufacturing and active materials, higher performance brushless machines are replacing the brushed ones in many applications. Thus, consequently Permanent Magnet Synchronous machines (**PMSMs**) represent nowadays one of the most attractive solution for automotive industry. Due to the high power/volume ratio (high power in restricted installation space) and high efficiency, PMSM can be designed to handle at the same time heavy loads at low and high speeds for a long-time operation. For these reasons PMSM is the most suitable electrical machine for any automotive application. However, due to limited availability of the rare earth permanent magnets which inherently determine a higher cost, it is the most expensive machine type as well.

Induction Machines (**IMs**) represent one of the most mature motor technologies that exhibits low cost, increased robustness and fault tolerance, maintenance-free operation and consolidated manufacturing technology [24]. On the other hand, IMs are recognized to have low efficiency and a rather poor power factor [25]. This can become even more critical for low-power applications, as it is the case in automotive field; therefore, they are used only for applications requiring higher power levels (e.g. traction or electric starter-generators).

Furthermore, due to the high costs of PMSMs, the rotor losses of IMs and the low efficiency of DC-machines, Reluctance Motors (RMs) can be considered as promising and attractive candidates. Moreover, the lack of the magnets, cage and windings on the rotor structure makes them cheaper and from the mechanical point of view, a robust and simple structure. There are two main categories of RMs, Switched Reluctance Motors (**SRMs**) and Synchronous Reluctance Motors (**SynRMs**). SRMs were always seen as having a great potential in automotive applications, due to some several positive features such as: simple to manufacture, robust magnet-free structure, which excels in higher speed or high temperature operation, low cost, fault tolerant and very good torque versus speed capability [24]. On the other hand, they are commonly known to exhibit an increased noise and vibration level as well as relatively high torque ripple and lower overall efficiency. Another drawback is that it requires a special inverter and control algorithm, that is different from any others electrical machines. The SRMs are using a non-standard converter that requires additional current sensors and motor connecting leads [26]. The second type of RMs is represented by the SynRMs. Their advantages are like SRMs, having no magnets or windings in the rotor, therefore avoiding magnets associated problems such as magnetization/demagnetization, temperature limitation, cogging torque, higher costs etc. The SynRM has good capabilities for a wide power range, as well as synchronous operating behavior with zero slip. In comparison to SRM, the noise generated by this type of motors is lower even than the one of an IM and it uses standard AC inverters.

Historical success has been limited by the technological inability to produce enough saliency, in order to achieve a high-power factor and high efficiency. Due to the complicated manufacturing process available now, the rotor configurations were not robust enough to withstand the forces that are required to sustain the torque which is produced and those centrifugal forces occurring at the maximum rotational speed. Nowadays, this technology has found its general acceptance for industrial applications, thus being mass-produced by companies like ABB and Siemens [27]. However, despite the significant progress that has been reported, for low power applications, there are still some drawbacks (provided hereafter) to be dealt with, before the market general acceptance. Things are a bit different when it comes to automotive industry. So far, no applications were designed for series production for SynRM in automotive industry, except research.

1.2. Synchronous Reluctance Machine

1.2.1. State of the art

This type of electrical machine is being around for a long time and it began to draw attention in the last decade and presently receives a great deal of interest, since the cost of active materials is much lower than for a PMSM (e.g. the rising costs and limited availability of rare-earth magnets in the last couple of years). The obvious advantage of this machine is that the cost is much lower in comparison with a PMSM. The latter is due mainly to the lack of magnets on the rotor side. Another advantage is the low value of losses in the rotor, in comparison with the IM that have copper losses from rotor currents [28]. The manufacturing process of this machine is very simple because the stator is similar to the one used for a standard AC induction motor [29]. Furthermore, the same facilities and tools in order to build them without any or minimal technological modifications (mainly industrial applications) are required. This machine has good capabilities for wide constant power range due to a good field weakening capabilities, as well as synchronous operating behavior with zero slip.

The first theoretical and technological attempt to realize the original patent for SynRM was made by Kostko in 1923 [30]. There are three different types of anisotropic rotor structure, see Fig. 1.3. The most common rotor structure is represented by transversally laminated (TLA) designs, Fig. 1.3 (c). The rotor lamination is punched in the traditional way and thin ribs are left behind after punching. Therefore, the rotor segments are connected to each other by tangential or radial ribs. Another rotor design from the same category is made by removing some iron material from each pole in the transversal region, see Fig. 1.3 (a). The third type is built with axial laminations, see Fig. 1.3 (b). The laminations are properly shaped at each pole and insulated from each other, using suitable passive materials (insulation). The axially laminated rotor (ALA) structure is the best design from the saliency ratio point of view, but the manufacturing process is very difficult and expensive at the same time. On the other hand, SynRMs with TLA are much cheaper, faster and easier to manufacture. Therefore, competitive designs for industrial applications are manufactured by big companies like ABB, Siemens and REEL [27,31-32].

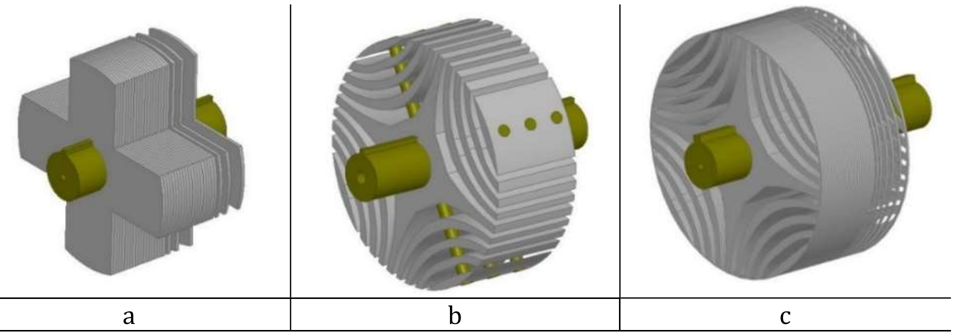

a b c

Fig. 1.3 SynRM rotor design: (a) Simple salient pole (SP) rotor, (b) Axially laminated anisotropic (ALA) rotor, (c) Transversally laminated anisotropic (TLA) rotor

Finding the appropriate rotor geometry for SynRMs has been the subject of high interest for major investigation in research and development field. The reluctance torque produced by the SynRM is directly related to the saliency effect. In order to increase the torque density, the saliency ratio (L_d/L_q) needs to be maximized. To fulfil this requirement, the geometry needs to be optimized. The saliency ratio of a SynRM can be increased by a proper arrangement of flux barriers on the rotor structure [29]. Reza Moghaddam [33] suggests in his work that increasing the number of barriers does not affect the d-axis inductance very much. Therefore, torque will not be affected if the number of barriers is increased more than a certain value (more than 9). On the other hand, torque ripple is directly influenced by the number of flux barriers. This fact can be noticed clearer on concentrated windings topologies, where in comparison to distributed winding the value of torque ripple is much higher. At the same time, a higher number of flux barriers will have a negative impact on the rotor structure and on manufacturing process. In addition, there are other factors that should be taken into consideration in order to increase the machine performances such as rotor diameter, air gap flux density and flux barriers design.

As possible alternative for IM drives, despite of all the advantages mentioned above, SynRMs are known for their lower power and torque densities, and for their poor power factor. SynRM power factor is 5% to 10% lower than IM [34]. In order to achieve a high-power factor for this machine, a large saliency ratio is needed. An acceptable power factor (e.g. 0.8) for this machine starts with a saliency ratio equal or higher than seven [33]. Otherwise, it requires large reactive power to reach a certain value of performance, which will cause the size of the inverter to increase. Inverter size is also related to the machine efficiency. Therefore, the required inverter size can be estimated by the product of the efficiency and power factor (η·cos φ).

Another way to improve the power factor is by adding a proper amount of permanent magnet (e.g. Ferrite) into the rotor, thus changing from a Synchronous Reluctance Machine to Permanent Magnet Assisted Synchronous Reluctance Motor (PM-SynRM). In this situation, excluding the parasitic component of the torque (cogging torque), the obtained torque can be divided in two components: the synchronous one (due to the presence of the PM) and the reluctance one (due to the saliency - REL). This kind of improvement gives about 20 % more electromagnetic torque in respect to the SynRM without PM. However, there are still some drawbacks do deal with and further developments are required to make it competitive in terms of performance/costs trade-off for automotive industry.

1.2.2 SynRM for automotive – possible applications

Nowadays, a vehicle needs several dozens of electric motors to operate several functions and fulfilling the same goals: comfort and safety. From wiper blades to power windows, from fuel pump to the starter motor, from brake assistance to turbochargers, the list is endless. Electrical motors, which are part of the electrical system in a vehicle may by classified by considerations such as power source type, internal construction, application and type of motion output [35]. Obviously, the number of these motors in cars is increasing progressively from one costumer to another according to their wishes for comfort, safety or additional features. Briefly, it is very hard to design a certain number of electrical motors that are part in a modern-day car. Nevertheless, it can be said with certainty that hundreds of small and medium size electrical motors (excluding traction) are part of different sub-systems of a modern car. A short classification in terms of requirements (e.g. torque and speed) for different applications is presented in Fig. 1.4 and TABLE 1.2.

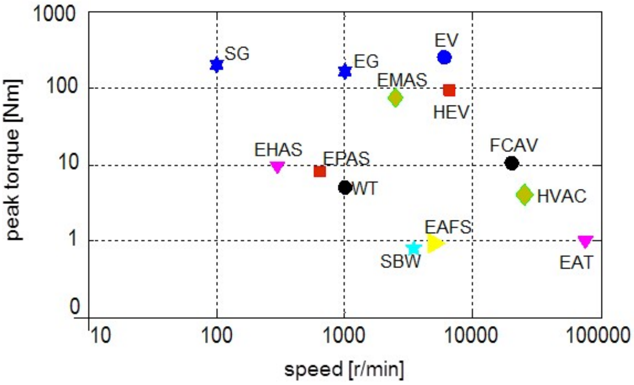

Fig 1.4 The electromechanical subsystems on board [19]

TABLE 1.2 The electromechanical subsystems on board explained

Appl.	Description
EPAS	**E**lectric **P**ower **A**ssisted **S**teering
EAFS	**E**lectric **A**ssisted **F**ront **S**teering
EMB	**E**lectro-**M**echanical **B**rake
CFM	**C**ooling **F**an **M**odule
HVAC	**H**eating, **V**entilation & **A**ir **C**onditioner

FCAC	**F**uel **C**ells **A**ir **C**ompressor
EG	**E**lectric **G**earbox
EHAS	**E**lectro-**H**ydraulic **A**ctive **S**uspension
EMAS	**E**lectro-**M**echanical **A**ctive **S**uspension
EAT	**E**lectrical **A**ssisted **T**urbochargers
VVT	**V**ariable **V**alve **T**iming
SG	**S**tarter **G**enerator
EVT	**E**lectric **V**ehicle **T**raction
HEVT	**H**ybrid **E**lectric **V**ehicle **T**raction

These drives need to meet various requirements such as high reliability, high torque and power density, low inertia, high dynamics, compactness, wide speed range, low torque ripple, good thermal and acoustic behavior and increased robustness. However, the choice of a motor for a certain application is governed by three dominant factors: cost, weight and size. When high performance criteria are required, PM-based synchronous machine are mainly preferred, due to their advantages such as higher torque density, high efficiency, low torque ripple and noise. Due to the continuously rising costs of the rare-earth magnets and the instability of the market, since some time, the magnet-free electrical machines have been brought back into the spotlight and thanks to some more-innovative designs, advancement of materials technology and electronics, they are becoming a serious competitor for Permanent Magnet Synchronous Machines.

However, despite the significant progress that has been reported, for low power applications there are still some drawbacks (provided hereafter) to deal with, before the market general acceptance. SynRM drives doesn’t fit for all automotive applications mentioned above, especially in very low power applications where power to weight ratio and installation space constraints are required (e.g. Variable Valve Timing, Electro-Mechanical Brake). Other applications, where SynRM does not seem appropriate at first sight are High Speed Applications (e.g. Electrical Assisted Turbochargers) where the working speed is around 60.000-100.000 r/min [36]. Even if SynRM appears to be an interesting choice for this application because of its small rotor losses at high speed, the rotor cannot withstand forces while ensuring full integrity. There are several studies (simulation results) in the literature [37], [38] that reports a speed around 20 to 48krpm offered by solid rotor SynRM, but special manufacturing processes and special materials are needed to achieve desired performances in terms of torque density and efficiency.

Another study [39] reported results on a conventional TLA SynRM design that is simulated and tested. In this study, a design procedure to realize a high speed SynRM for aeronautical applications is described. The considered case study is 5kW, 50.000 rpm SynRM, designed for an electrically driven compressor for two strokes aeronautical diesel engine. According to experimental results, the authors [39] report: "The results of a no-load speed acceleration from zero to 30.000 rpm that is the **maximum speed** reached at this time of writing".

At this stage, unfortunately there are no SynRM manufactured (mass production) for any kind of automotive application. Before the SynRM is completely ruled out as an option in this field, some further studies related to design, control and maybe in the near future new core materials need to be performed. Moreover, state of the art for several electric drives for automotive industry like electric vehicle traction, electric power assisted steering and cooling fan module, with the possibility of using SynRM drives is presented. A detailed classification for such applications in terms of requirements, is carried out in TABLE 1.3 [40].

TABLE 1.3 Requirements of several electric drives in automotive applications

Application	Power [kW]	Voltage [V]	n_{max} [r/min]	Machine type
EVT	35-225	300-800	16000	DC/PMSM/IM
EPAS	0.2-2	12-24	2000	DC/PMSM/IM
CFM	0.2-1	12-24	2700	DC/PMSM

A. Electric Vehicle Traction

Vehicle electrification is a topic that will lead to revolutionary improvements on energy resource conservation and pollutant emissions. During the last decade, electric vehicles have entered the mainstream, and market share is expected to increase significantly soon. Finding the proper electric motor for EVs is a very important step that requires special attention. Automotive industry is still seeking for the best motor drive for EVs or HEVs. Therefore, finding the most suitable motor for an EV is a challenging issue. Actual motor technology on pure electric vehicles can be reflected in TABLE 1.4.

TABLE 1.4 Technical specifications of electric vehicles [47]

Electric car	Motor Type	Motor Power	All electric range	Battery
Renault ZOE R90	SM	41 kW	403 km	41 kWh
Citroen C-ZEROs	PMSM	47 kW	127 km	16 kWh
Peugeot iON	PMSM	47 kW	127 km	16 kWh
Nissan Leaf	PMSM	80 kW	378 km	40 kWh
BMW-i3	PMSM	125 kW	285-310 km	42.2 kWh
Mitsubishi i-MiEV	PMSM	49 kW	150km	16 kWh
Tesla S	IM	225 kW	502 km	85 kWh
Tesla Roadster*	IM	1000 kW	970 km	200 kWh

So far, according to Table 1.4 there are three types of motor drives that have been applied to EVs. According to the advantages of permanent magnet (PM) materials mentioned above, PMSMs are the most used traction drives on the market these days. Thanks to the constant power speed range (CPSR) and high efficiency system, a special attention has been given to these types of electrical machines in a variety of automotive applications, (e.g. traction and auxiliaries drives). The choice of voltage levels for different EV is determined by the vehicle class. From small vehicle (e.g. Renault Zoe) to sports car (e.g. Tesla Roadster) results a great variation and individuality. Electric powertrain performances of more than 12 kW are now reserved for high voltage range. In automotive industry, high voltage is considered to voltages above 60 V. A classification of voltages for small, medium and sport cars can be seen in TABLE 1.5 [42].

TABLE 1.5 Vehicles and power categories considered

		Small car	Medium car	Sports car	Unit
Max. power		60	80	180	kw
Torque		200	300	500	Nm
DC Voltage	max.	450	400	800	V
	min.	300	300	600	V
Max. current	DC	200	333	550	A
	AC	250	450	1000	A

The vehicle performance is completely determined by the profile of torque produced in respect with the vehicle speed on the driven wheels. For an internal combustion engine, a multi-gear transmission is needed to shape the torque versus speed profile. On the other hand, the choices of an electric traction drive system in an EV could be according to Fig. 1.5 [43].

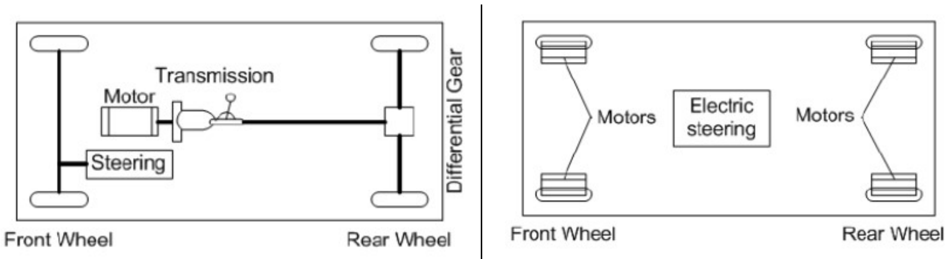

a) Conventional Type

b) Four- wheel Direct-drive

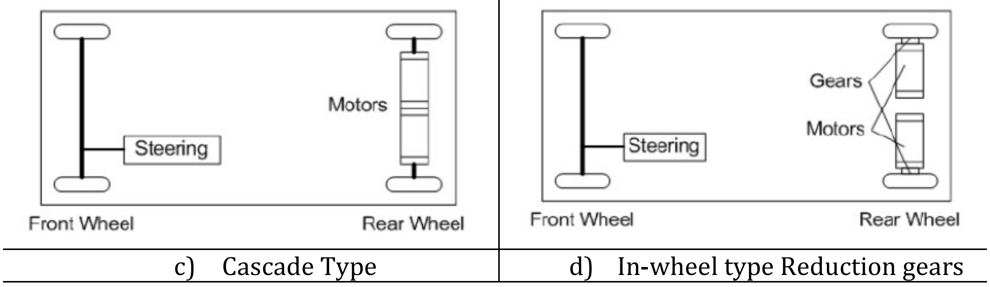

c) Cascade Type

d) In-wheel type Reduction gears

Fig. 1.5 Choices of drivetrain system in an EV [43]

The specification data of an electric drive used for traction in EV, along with their specifications is described in TABLE 1.6. The demanded torque-speed characteristic is depicted in Fig. 1.6.

TABLE 1.6 Specification data for an BMW I3 42.2 kWh

Parameter	Units	Value
Dc-bus Voltage	V	200 to 400
Max. Phase Current	A	400
Motor type	-	PMSM
Peak Torque	Nm	250
Constant Torque	Nm	88
Base Speed	rpm	4500
Max speed	rpm	11,400

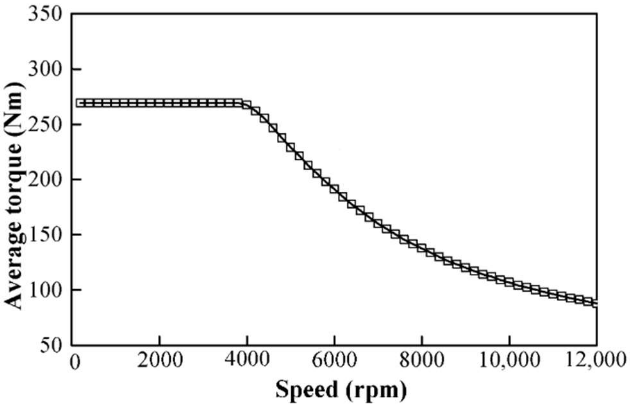

Fig 1.6 Required Torque vs Speed characteristic for an BMW I3 powertrain [44]

A SynRM, without or with assistance of PMs, can be suitable for traction application [50]. Due to the high-power density obtained at lower costs (compared to a PMSM) and good efficiency (better than IM) at high speeds (low value of iron losses) turns this topology in a strong candidate for such automotive drive.

Finally, some other problems associated with the usage of magnets (e.g. magnetization/demagnetization, cogging torque, etc.) can be avoided. However, the challenge of achieving a good CPSR is directly related and dependent on the mechanical aspects of the design.

B. Electric Power Assisted Steering

Before any kind of driving assistance, steering was purely mechanical, using a rack and a pinion system linked directly to the steering wheel. In the early of 1950s, Hydraulically Assisted Steering (HAS) was introduced to vehicles, which dominated the automotive world [19]. This type of system uses a hydraulic pump, which is powered through a belt connected to the combustion engine. Although it is very efficient and used even today, hydraulically assisted steering has some drawbacks. The latter is given mainly, because the pump is driven always by the engine, even if it is used occasionally during vehicle operation. This means that a small amount of power is shifted from the combustion engine to the pump, which generally reduces the efficiency of the propulsion system. Therefore, hydraulic assistance is deemed as a parasitic loss due to a penalty of fuel consumption up to 4% [16] and it needs maintenance on mechanical components (i.e. transmission belt, hydraulic pump, fluid leakage). Therefore, another alternative form of steering must be used. Passing from hydraulic to full electric assistance has a significant boost. Power on demand and less maintenance, higher efficiency from the engine side and low fuel consumption have significant advantages above all. However, other obstacles, mainly cost, torque ripple and safety must be considered.

Electric power steering has a simple architecture: an electric motor is usually placed either at the base of the steering column (Fig. 1.7a) or directly on the steering rack (Fig. 1.7b). Sensors (especially torque sensors) are mounted on the motor and steering wheel side, to provide input data from the driver to control unit. For safety reasons, a mechanical link from the driver (via steering wheel) to the steering rack is available as a fall back in case of failure. Torque ripples generated by the electrical machines could also be a concern. Even if they are small in comparison to other active parts (i.e. combustion engine, pumps, cooling fan modules, heat-ventilation, and air conditioning), it can be felt by the driver through the steering wheel and it can lead to a distraction or a concern for a customer who was accustomed with a smooth hydraulic steering system [35]. For all these, to provide safety and comfortable driving assistance, the development of reliable electric motors and their control strategies is needed.

a b

Fig 1.7 Electric Power Assisted Steering system [44], [45]

The specification data for the electric motor of an electric power assisted steering placed directly on the steering rack along with their values as described in the literature [35] is given in TABLE 1.7. The required torque-speed characteristic is depicted in Fig. 1.8.

TABLE 1.7 specification data for the electric motor for an electric power assisted steering [35]

Parameter	Units	Value
Dc-bus Voltage	V	13
Motor Type	-	PMSM
Rated Current	A	175
Torque	Nm	24
Rated Speed	rpm	1000

For such an application, SynRM can be a proper candidate as it presents advantages in terms of NVH (Noise, Vibration and Harshness). As it is mentioned above, the main parameters for this application are high torque density and very low cogging torque. Furthermore, for this speed operation (1000 r/min) SynRM has no problem to ensure the rotor integrity. Before taking into consideration this alternative solution, space constraints limitations need to be investigated.

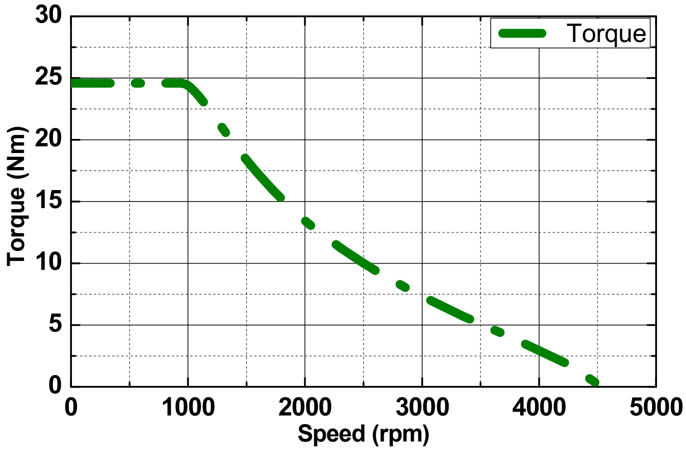

Fig 1.8 Required Torque vs Speed characteristic for a drive used in electric power assisted steering

C. Cooling Fan Module – engine part

The cooling system is one of the key parts for internal combustion engines, having the function to maintain the desired coolant temperature for proper operating conditions [46], [47]. To accomplish this task, it needs to reject the heat from the engine components and its surrounding to the local environment rapidly enough to keep the engine temperature for enhanced performance. The thermostat valve, radiator, radiator fan(s) and the water pump are all parts of the most used cooling system, based on the liquid cooler. Nowadays, all conventional cars are equipped with a cooling fan that is driven by a separate electric motor. The reason why electric-cooled cooling fans are preferred instead of a mechanical belt fan is fuel economy and better acoustic performance. A belt-driven fan can absorb up to 12 or more horsepower from the engine power, depending on engine speed and cooling load [48]. Electric fans are controlled either with a thermostatic switch or by the engine computer. The fan speed is directly related to the coolant temperature when it goes above a set point. Extra cooling is not needed when a cold engine is first started, so the fan is idle until the engine reaches normal operating temperature (195 to 215 degrees) [47].

In Fig. 1.9 a typical engine cooling system is presented. The cooling system of Hybrid or Full EV is similar to the one of the conventional internal combustion engines. In addition, the electrical motor, its inverter, and the battery pack need to be cooled down at a lower temperature than for an ICE. Cooling systems need to be able to keep the battery pack in the temperature range of about 20-40 degrees Celsius, as well as keeping the temperature difference within the battery pack to a minimum (no more than 5 degrees Celsius) [48]. The requirements for such an application targeting an ICE cooling fan includes high efficiency, high reliability and good NVH behavior. So far, there are two types of electrical machines that are used in a cooling fan system, PM brushed and Brushless DC motors.

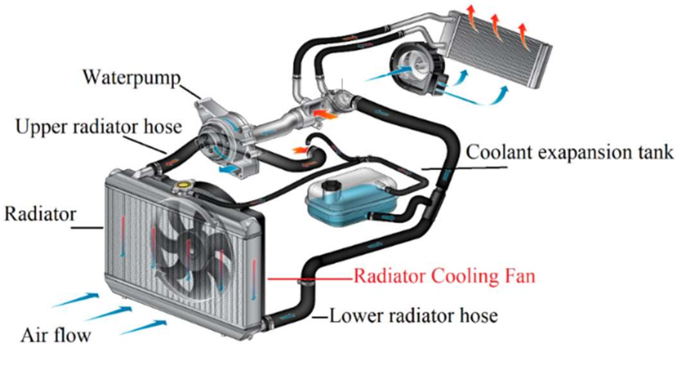

Fig 1.9 Engine cooling system diagram [47]

The specification data for an electric drive used for CFM application, along with their values as described in the literature [67] is given in TABLE 1.8. The required torque-speed characteristic is depicted in Fig. 1.10.

TABLE 1.8 Specification data for a cooling fan motor [54]

Parameter	Units	Value
Dc-bus Voltage	V	13
DC Current	A	24
Motor Type	-	PMSM
Torque	Nm	0.85
Rated Speed	rpm	2700

For this application, SynRM was taken into account. The objective of the thesis is to integrate SynRM in low power automotive applications. The CFM drive may be a possible application in which SynRM can reflect its advantages.

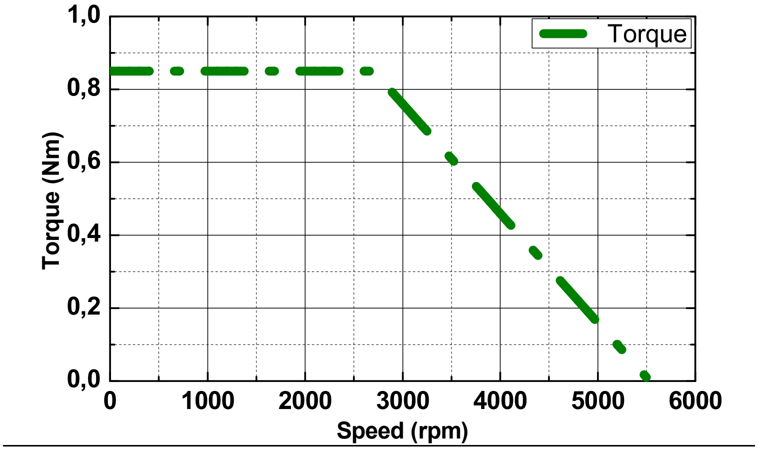

Fig 1.10 Required Torque vs Speed characteristic for a CFM

1.3. Conclusions

The automotive industry comprises a wide range of possible applications where an electrical motor can be used. For each application, different requirements are imposed, therefore a electrical machine cannot fulfill all of them. In general, for light electric vehicle applications is mostly used PMSMs. This thesis aims to tackle some of these challenges, and thanks to the development of new materials and concepts, PM-less motor topologies such as SynRMs are perceived as promising alternative. Such machines can be used in power steering, engine cooling fans, traction applications, and in several other automotive applications.

The SynRMs taken into study in the frame of this thesis are intended to be used for a car`s cooling fan application. The basic specifications for this type of machine have been presented above.

2. SynRM – an Overview

2.1 SynRM – an Overview

SynRM is an electrical machine that uses for its torque production the reluctance concept. The main idea can be explained using Fig. 2.1. A simple method to envision it is with a single winding, a stator core and a one pole-pair rotor. When the coil is energized, a variable magnetic field passes through the stator core to the rotor part. The rotor will turn to minimize the air gap in the magnetic circuit. In order to produce torque, an angular difference between d-axis and the magnetic field is needed ($\delta \neq 0$, see Fig. 2.2). The level of torque depends on the saliency effect and is proportional to the difference between the inductances L_d, L_q of the d-q axis. To achieve a high torque density, the saliency ratio between L_d/L_q needs to be maximized.

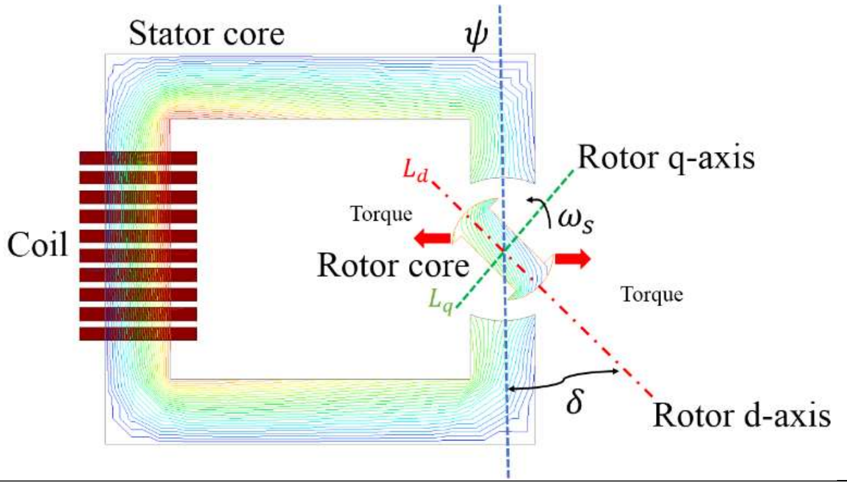

Fig. 2.1 Reluctance concept explained

In a SynRM the electromagnetic field is produced by a three-phase concentrated or distributed winding in a slotted stator and it links the stator and the rotor through a small airgap.

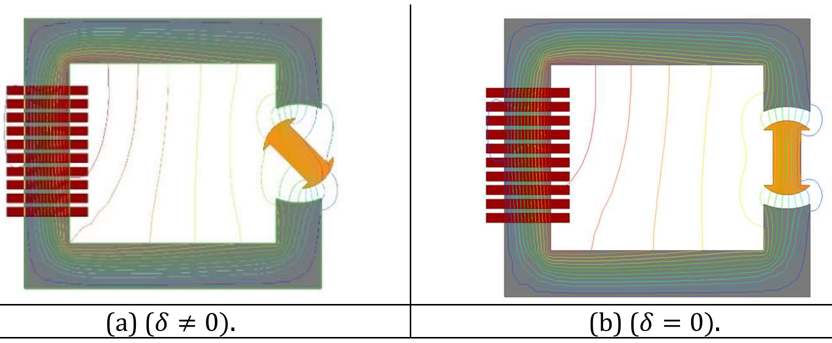

(a) ($\delta \neq 0$). (b) ($\delta = 0$).

Fig. 2.2 Magnetic field and reluctance torque production

The electromagnetic field is rotating at synchronous speed, ω_s and can be assumed to have a sinusoidal distribution. According to Fig. 2.3, while it rotates, the inductance goes from maximum in the d-axis to minimum in q-axis. Therefore, the rotor position with respect to the stator has also an impact on the machine's inductances. Moreover, the SynRM performance is mainly affected by these two inductances, which are directly related to the rotor topology.

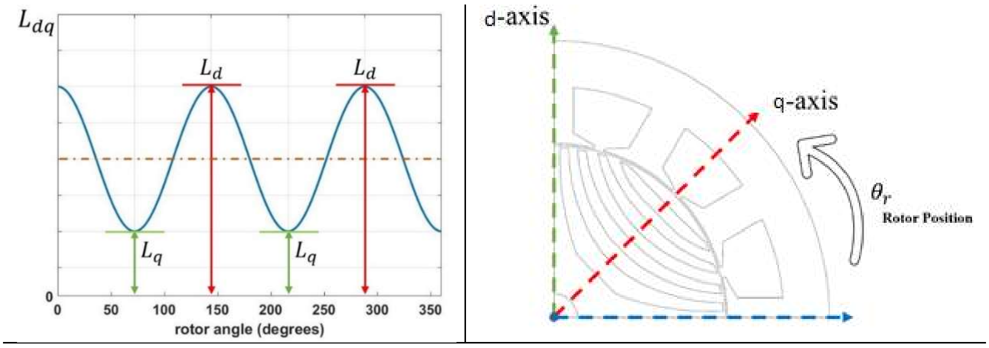

Fig. 2.3 Variation of inductance with respect to rotor position

2.2. SynRM - equivalent circuit and mathematical model

For analysis, in many studies the three-phase a-b-c frame of reference is converted into a synchronously rotating rotor frame, using Park's transformation. The d-q equivalent circuit and the phasor diagram of a SynRM in steady state is shown in Fig, 2.4 [26] and Fig. 2.5 [49], respectively.

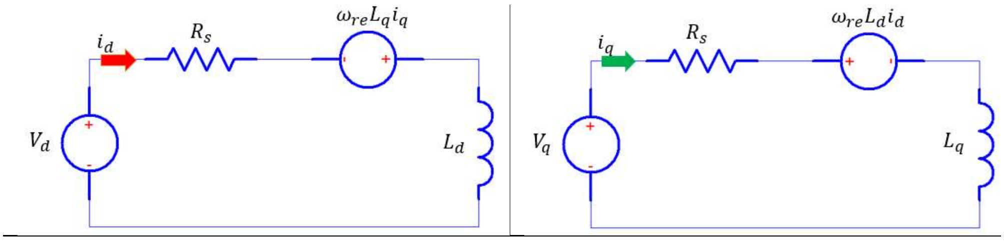

Fig. 2.4 d-axis (left) and q-axis (right) equivalent circuit of SynRM

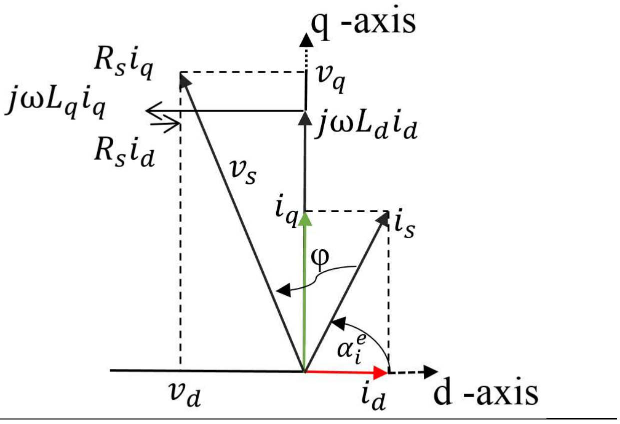

Fig. 2.5 SynRM phasor diagram

where,

i_s	represents the phase current, [A]
v_s	represents the phase voltage, [V]
i_d, i_q	are the reference frame d-q axes supply currents, [A]
V_d, V_q	are the d-q axis terminal voltages, [V]
v_d, v_q	are the reference frame d-q axes voltages, [V]
L_d, L_q	d-q axes inductances, [H]
R_s	is the stator phase resistance, [Ω]
ω_{re}	rotor angular speed, electrical [rad/s]
ω	rotor angular speed, mechanical [rad/s]
α_i^e	Current vector angle, [deg]
φ	power factor angle, [deg]
j	total mechanical inertia, [kg·m^2]

The module of the stator current (I_s) is given by equation 2.1 and a phasor representation is illustrated in Fig. 2.6.

$$I_s = \sqrt{I_{sd}^2 + I_{sq}^2} \tag{2.1}$$

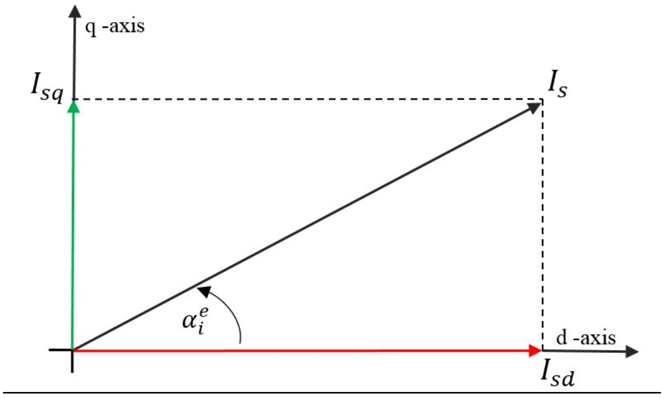

Fig. 2.6 Stator current position in d/q frame

The phase current I_s is split in its I_{sd} and I_{sq} components so as to achieve the maximum torque per given current by the variation of the current vector angle, α_i^e. Furthermore, they produce the flux linkages $L_d i_d$ and $L_q i_q$ respectively. Easily it can be said that both L_d, L_q inductances are directly depended only on self-currents. However, this affirmation is not true since the inductances are depended on both i_d, i_q currents. The effect of magnetic saturation is called cross-saturation and has been analyzed in [51]. Here, the authors showed that the d-axis flux linkage varies linear with i_d for small values of d-axis current and when the i_d current increases, the flux linkage in the d-axis gets saturated. Thus, L_d inductance is reduced.

The cross-saturation has a major effect on the performance of the sensor-less control system, and it should be considered when such a control is developed for SynRM [51]. The corresponding equations for a SynRM in *dq* reference frame fixed to the rotor are given as follow [26-52]:

$$
\begin{aligned}
V_d &= \mathrm{R_s} i_d + L_{ds}\frac{di_d}{dt} - \omega_{re} L_q i_q \\
V_q &= \mathrm{R_s} i_q + L_q\frac{di_q}{dt} + \omega_{re} L_d i_d
\end{aligned}
\tag{2.2}
$$

Further, the electromagnetic torque equation is given by:

$$T_{dq} = \frac{3}{2} p\, (\psi_d i_q - \psi_q i_d) \tag{2.3}$$

Where, p is the number of pole pairs, ψ_d, ψ_q, i_d and i_q are the d and q components of the flux linkage and current. Therefore, the flux linkage can be expressed as follow:

$$
\begin{aligned}
\psi_d &= L_d i_d \\
\psi_q &= L_q i_q
\end{aligned}
\tag{2.4}
$$

Furthermore, the inductance of d-axis and q-axis can be defined as:

$$
\begin{aligned}
L_d &= \frac{\psi_d}{id} \\
L_q &= \frac{\psi_q}{iq}
\end{aligned}
\tag{2.5}
$$

The corresponding electromagnetic torque, T_e, according to the relationship between the flux linkage and the current, equation (2.2) can be written as:

$$T_e = \frac{3}{2} p\, (L_d - L_q)\, i_d i_q \tag{2.6}$$

The corresponding motor dynamic equation is:

$$T_e - T_L = J_m \frac{d\omega}{dt} + B_m \omega \tag{2.7}$$

where, T_L is the load torque, J_m is the inertia moment of the rotor and B_m is the viscous friction coefficient and ω represents the mechanical speed. The electromagnetic torque and the power factor (cosφ) of the SynRM it is direct dependent on the saliency ratio effect (ξ) defined as the ratio between d-axis over the q-axis inductances.

$$\xi = \frac{L_d}{L_q} \tag{2.8}$$

The power factor as a function of the current angle γ for any saliency ratio $\xi = L_d/L_q$ can be written as:

$$cos\ \varphi = \frac{\xi-1}{\sqrt{\xi^2 \frac{1}{sin^2\gamma} + \frac{1}{cos^2\gamma}}} \tag{2.9}$$

According to equation (2.7), the power factor has the highest value when the current angle is equal to:

$$\gamma_{max} = \text{atan}\sqrt{\xi} \tag{2.10}$$

moreover, the maximum power factor is:

$$cos\ \varphi_{max} = \frac{\xi-1}{\xi+1} \tag{2.11}$$

The total losses in a SynRM consist of copper losses, core losses and mechanical losses.

$$P_{tot} = P_{Cu} + P_{Fe} + P_{mec} \tag{2.12}$$

Copper losses can be computed using the already know relation i^2R, applied for all three phase windings as:

$$P_{Cu} = \Sigma_m (i_{ph(RMS)})^2 R_{ph} \tag{2.13}$$

where, $i_{ph(RMS)}$ represents the RMS value of the phase current, m is the number of phases, and R_{ph} is the calculated phase resistance.

The temperature rise on the phase resistance can be also calculated using:

$$R_{T_2} = R_{T_1}\left[1 + \propto_{T_1} (T_2 - T_1)\right] \tag{2.14}$$

where, $\propto_{T_1}$ is the temperature coefficient and R_{T_1} is the resistance, both at temperature T_1. At high speeds the copper losses have the tendency to increase due to the skin effect and proximity effects as explained in [79].

2.3. SynRM – design issues

Finding an appropriate electromagnetical design for the SynRM has been a subject of interest since 1923 [30] until present. In this chapter, based on several studies [28], [33], [50-53] the optimal slot/pole/phase combination, winding technology and rotor designs that can fit for a SynRM, will be analyzed.

2.3.1. Guidelines for slot pole selection

Excluding some special cases, in general, the number of phases is the first decision that must be made when starting a machine design process, followed by the selection of the slot/pole combination. Each group or set phase coils must be located symmetrically spaced around the stator (e.g. TABLE 2.1). Large machines (e.g. generators) are using multiple 3 phase circuits. Nevertheless, in industry the most common machines are the 3-phased ones (e.g. PMSM, IM, SynRM). The number of slots and poles and the winding configuration are interdependent degrees of freedom for a specific machine design. Nevertheless, only certain combinations are possible for a symmetrical 3-phase windings. Several considerations must be taken into account before choosing the optimum slot/pole combination for a SynRM is chosen. For SynRMs and IMs, the issues related to the number of rotor poles are following the same guidelines.

TABLE 2.1 Phase number for balanced windings

Phases	Phase coil set spacing
2	180°
3	120°
4	90°
5	72°
6	60°

It’s been proven [54-57] that the 4 pole rotor topologies exhibit the highest torque and efficiency for these machines. For a higher number of poles, the efficiency and power factor drop considerably due to the leakage and synchronous reactance. Typical SynRM designs have the tendency to keep the same number of poles equal to an existing IM and uses the same stator lamination. For machines with larger diameters, a higher number of poles can be used and a different slot pole combination, thus obtaining a high saliency (ξ) design (2.8).

Advantages and disadvantages of increasing number of poles in electrical machines [58] are as following:

- Advantages:
  - Reduction of active materials
  - Higher torque density
  - Higher efficiency thanks to the phase resistance reduction (for concentrated winding designs) obtained by shorter overall copper wire length.

- Disadvantages:
  - Higher flux leakage
  - Increased iron losses
  - Higher commutation (e.g. PWM) frequency is needed

In TABLE 2.2 a list of several possibilities for three phase symmetrical windings together with the maximum fundamental winding factor for each combination, is presented. The number of slots (column 1) must be divisible by the number of phases (in this situation 3 phases) and the number of poles (line 1) must be divisible by two [59]. The winding selection for any given slot/pole combination should be chosen as function of winding factor (as high as possible).

TABLE 2.2 slot and pole combination for three phase balanced windings

Qs/p	2	4	6	8	10	12	14
3	🟩 0.866	🟩 0.866	⬛	🟩 0.866	🟩 0.866	⬛	🟩 0.866
6	🟥 1	🟩 0.866	⬛	🟩 0.866	🟩 0.5	⬛	🟩 0.5
9	🟧 0.945	🟩 0.617	🟩 0.866	🟩 0.945	🟩 0.945	🟩 0.866	🟩 0.617
12	🟥 0.966	🟥 1	⬛	🟩 0.866	🟩 0.966	⬛	🟩 0.966
15	🟧 0.951	🟧 0.951	⬛	🟩 0.711	🟩 0.866	⬛	🟩 0.951
18	🟥 0.96	🟧 0.945	🟥 1	🟩 0.617	🟩 0.735	🟩 0.866	🟩 0.902
21	🟧 0.953	🟧 0.953	⬛	🟩 0.538	🟩 0.65	⬛	🟩 0.866
24	🟥 0.958	🟥 0.966	⬛	🟥 1	🟩 0.588	⬛	🟩 0.766
27	🟧 0.954	🟧 0.954	🟧 0.945	🟧 0.941	🟩 0.525	🟩 0.617	🟩 0.695
30	🟥 0.957	🟧 0.951	⬛	🟧 0.951	🟥 1	⬛	🟩 0.64
33	🟧 0.954	🟧 0.954	⬛	🟧 0.954	🟧 0.946	⬛	🟩 0.551
36	🟥 0.956	🟥 0.96	🟥 0.966	🟧 0.945	🟧 0.942	🟥 1	🟩 0.551

Legend	🟥	Integer- slot winding	🟧	Distributed winding
	🟩	Concentrated winding	⬛	Unbalanced winding

2.3.2. Winding technology

The available literature is only focused on SynRM with distributed winding and very few studies [26], [60] on SynRM with concentrated winding have been carried out. Most of the studies [61], [62] illustrate that distributed winding arrangement exploit the magnetic saliency better, as that it produces higher saliency ratio due to lower space harmonics content of stator magneto-motive force (MMF). However, in this study an attempt to underline the design features of 3-phase SynRM proposed for automotive application with tooth wound coils (concentrated windings) and distributed windings, taking into consideration different slot/pole combinations, it is investigated. Furthermore, TABLE 2.3 presents a summary of both winding topologies, concentrated windings (CW) and distributed windings (DW) [26].

TABLE 2.3 Comparison between selected winding types

	CW	DW
Fundamental Winding Factor	++	+++
Harmonics	+	+++
Fill Factor	+++	+
End Length	+++	+
Manufacturing	+++	+
Perceived Cost	++	+
Maturity	++	+++

A. Concentrated windings

Several definitions are used in literature for windings having non-overlapping coils with. These terms might be [62]: concentrated windings [63], [64], tooth concentrated fractional windings [65], non-overlapping concentrated windings [66], tooth concentrated windings [67], fractional slot wound [68], fractional-slot with non-overlapped coils [69], fractional slot pitch concentrated windings [26]. Normally, concentrated windings have the coil span equal to 1 and the number of slots/poles*phases is fractional and inferior to 1 [67].

$$q = \frac{Q_s}{2pm} \in \mathbb{Q} < 1 \qquad (2.15)$$

Two configurations can be used when it comes to choose the number of layers for a winding design. Single layer windings have coils only on alternate teeth, whereas each tooth of the double layer windings is wounded [62]. This winding layer distribution can be seen in Fig. 2.7 and 2.8. For this study 12 slots /4 poles topology is investigated.

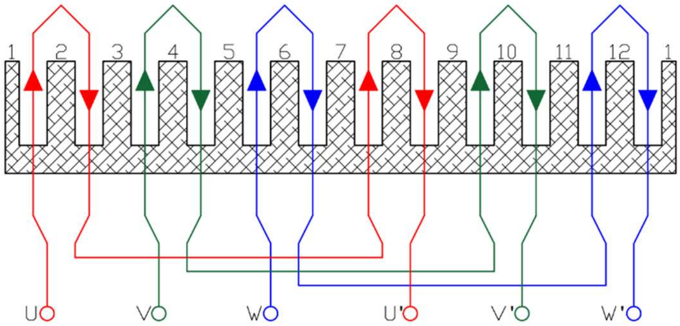

a) One-layer distribution

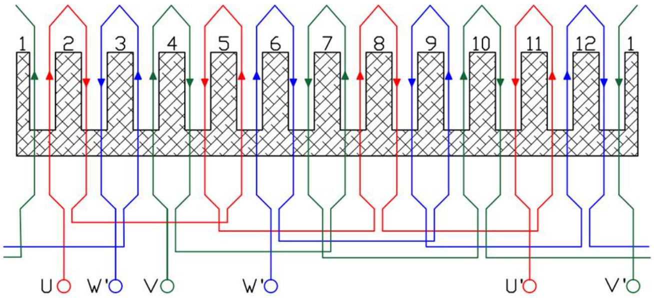

b) Double-layer distribution

Fig. 2.7 12 slots / 4 poles CW layout

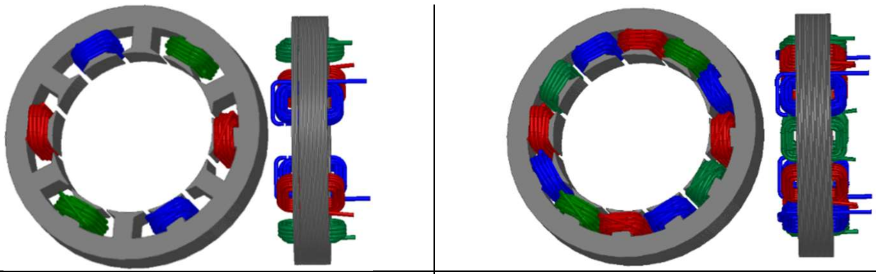

(a) Single layer and end windings design

(b) Double layer and end windings design

Fig. 2.8 12 Slots/4 poles topology stator design with one (a) and (b) double layer

Number of layers' selection depends mostly on the application. The difference is that the single layer winding has just one coil per slot and the double layer winding has two coil sides per slot. Advantages and disadvantages characteristics of single- and double-layer concentrated windings are reflected in TABLE 2.4 [62].

TABLE 2.4 Comparison between single and double – layer concentrated windings

	Single - layer	Double - layer
Fundamental winding factor	Higher	Lower
End – turns	Longer	Shorter
Slot fill factor	Higher	Lower
Self – inductances	Higher	Lower
Mutual – inductances	Longer	Higher
EMF	Trapezoidal	Sinusoidal
Harmonic content of MMF	Higher	Lower
Eddy current losses in PM	Higher	Lower
Overload torque capability	Higher	Lower
Slot pole combination	Lower	Higher
Ease of Manufacture	Very good	Good

Single layer windings are preferred instead double layer winding when a high fault tolerance is required. Hence, the coils are individually isolated (thermally and electrically) and the configuration leads to a high self-inductance and a very low mutual inductance. Due to their higher self-inductance, single layer is preferred in applications where a CPSR is required. On the other hand, double layer windings are preferable to minimize the copper losses and torque ripple [62]. Moreover, a double layer winding offers more slot/pole combinations than the single layer winding. In automotive applications, electrical machines are most of the time manufactured with three phases in delta or star connection, and for coils production in most of the cases the needle-wound technique is used (see Fig. 2.9). There are several advantages when needle winding technology is used:

- Wires with diameter < 2.5 mm can be used
- Direct winding without the necessity of coil insertion
- Possibility of process automation
- Reduction of joints

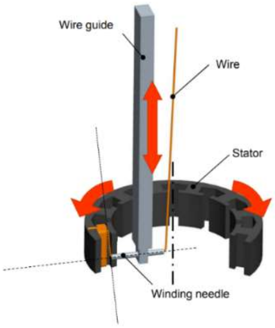

Fig. 2.9 Needle winding technique for CW-machines [62]

B. Distributed windings

Distributed windings are well known for their lower harmonics content and a higher winding factor, thus, an improved torque density and a better efficiency compared to concentrated windings. However, in spite of these advantages, the obtained winding layout is rather complicated and expensive to be manufactured, which is often a showstopper, for small, low power electrical machines used in automotive applications. Distributed windings are defined by the number of slots per pole and phase, but in this situation the value obtained is either integral or fractional:

$$q = \frac{Q_s}{2pm} \in \mathbb{Q} \tag{2.16}$$

For a fractional distributed winding, the shape of the MMF distribution along the airgap is close to a sinusoid and it can be finely controlled so that the magnitudes of applicable field harmonics can be further refined [26]. Fig. 2.10 presents the distributed winding diagram for 27 slots /4 poles topology.

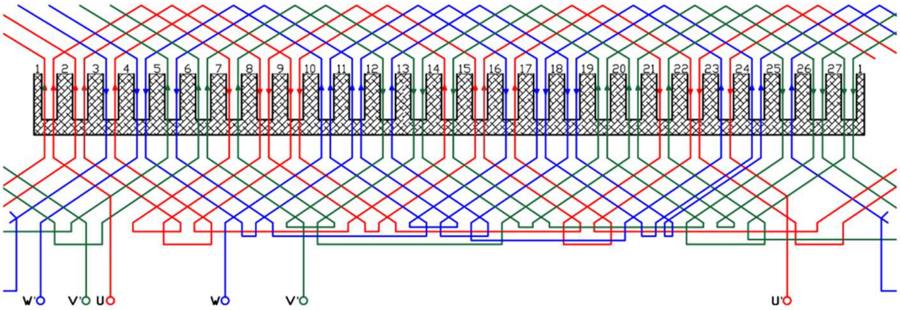

Fig. 2.10 27 slots / 4 poles distributed winding layout

It can be stated that distributed windings require a laborious winding process with an increased difficulty in manufacturing/assembly. Nevertheless, another snag comes due to the overlapping coils. It can be seen in Fig. 2.11 (b), that for small power applications (e.g. pumps, fans), end-windings represent a drawback when it comes to installation space constraints (total axial length).

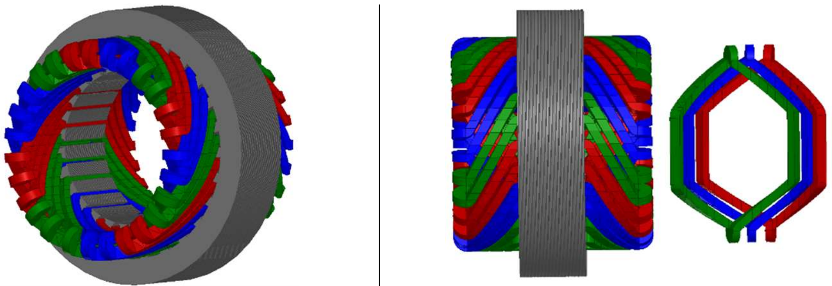

(a) double layer winding design | (b) End windings and Lap-Coils design

Fig. 2.11 27 Slots / 4 poles topology stator design with one (a) and (b) double layer distribution

2.4 Rotor Topologies

A short description regarding the historical evolution of rotor geometries that can be useful to understand the SynRM functionality, is presented in Fig. 2.12 [29]. The rotors in Fig. 2.12 (a, c) are derived from a conventional induction rotor design. The very first designs were obtained by removing certain teeth from the induction rotor. This operation can be achieved either by milling after casting the cage, or by punching before casting the cage (Fig. 2.12 a). This type of rotor has a simple construction, but the saliency ratio is too small. However, these rotors have poor performances to make them competitive in comparison with other alternative rotors. Fig. 2.12 (b) shows a salient pole synchronous motor with no windings. In literature it is mentioned [32] that no value of saliency ratio higher than 3.8 has been achieved with this rotor design. Therefore, considering the low performances of previous designs, other type of rotor configurations is considered, as the one barrier (Fig. 2.12 c, d) or multi-barriers design (Fig. 1.5 e, f).

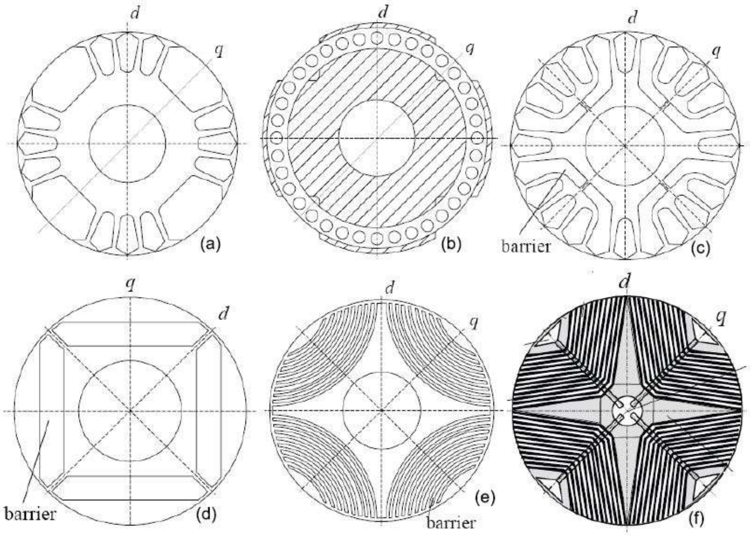

Fig 2.12 (a, b, c, d, e and f) Historical evolutions of different alternative rotor geometries [29]

The current market of SynRMs is based on a rotor topology with TLA laminated flux barriers (e.g. ABB, Siemens, REEL-KSB, see Fig. 2.13).

This rotor design is frequently used due to its great torque performances that can be achieved by guiding the flux lines with its unique design.

ABB – SynRM | Siemens – SynRM | REEL-KSB - SynRM

Fig. 2.13 Current market of SynRM [27,31,32]

The rotor design, which is confirmed in several applications, is presented and described in Fig. 2.14.

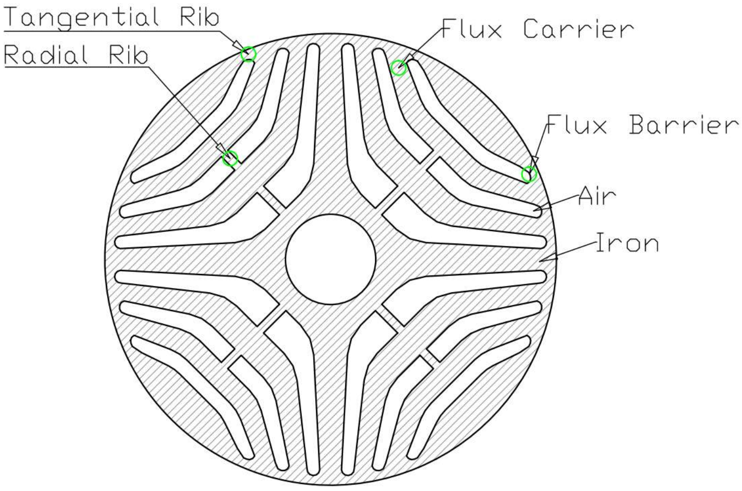

Fig. 2.14 4-pole TLA SynRM rotor design

In this thesis, based on several studies [26], [16] and [28], different slot/pole combinations using the same rotor design will be investigated and analyzed.

2.5 Multiphysics design and optimization

By definition, multiphysics studies the simultaneous interactions between more than one physical fields. When it comes to a modern product, the understanding of how these phenomena interact is the way to ensure safe and reliable function [71]. Fluid forces, thermal effects, electromagnetics and structural integrity might all have an impact on product performances. In case of electrical machines, multiphysics analyses can help the designer to examine the mechanical, thermal and acoustic behavior of the studied machine beside the electromagnetic analysis. All these aspects can be isolated and analyzed separately in order to get an accurate prediction of the machine behavior in each field.

For clarity, a diagram that includes the multiphysics-workflow is shown in Fig. 2.15.

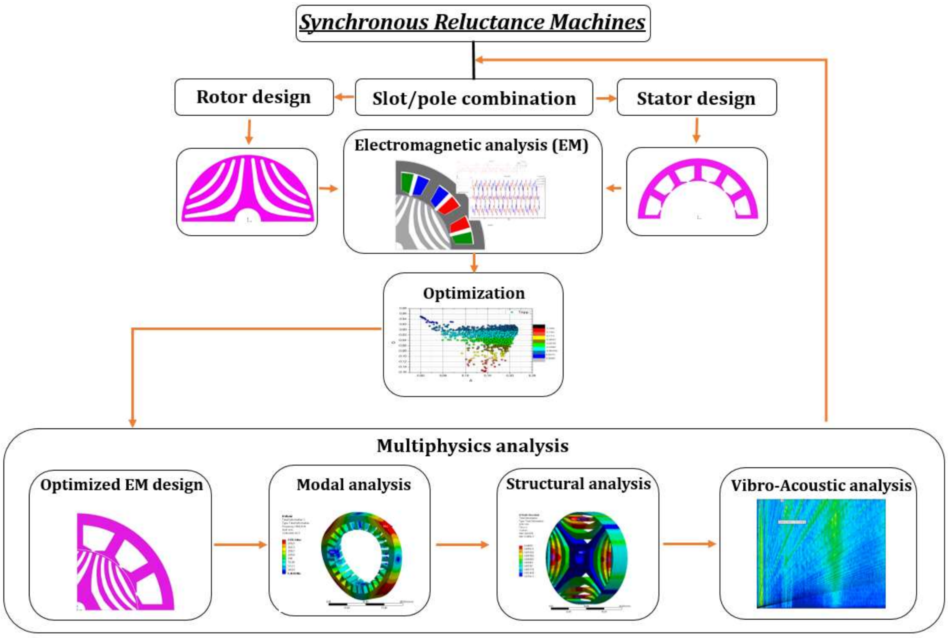

Fig. 2.15 Multiphysics workflow for studied SynRM

The performance characteristics of the SynRM is directly related to the geometry of the machine. Due to the complex rotor structure of this machine an advanced design optimization based on different techniques [72-

74] is implemented. The main objective of the optimization process is to maximize the average torque while minimizing the torque ripple.

An artificial intelligence approach using Particle Swarm Optimization (PSO) coupled with FEM models is used for the characterization and design optimization for all studied SynRMs. Fig. 2.16 shows the proposed optimization procedure where the parametrized FE model is coupled with the optimization algorithm. The implementation was done in Python code in the scripting language of the ANSYS/Maxwell software, which is employed as the FEA computational software.

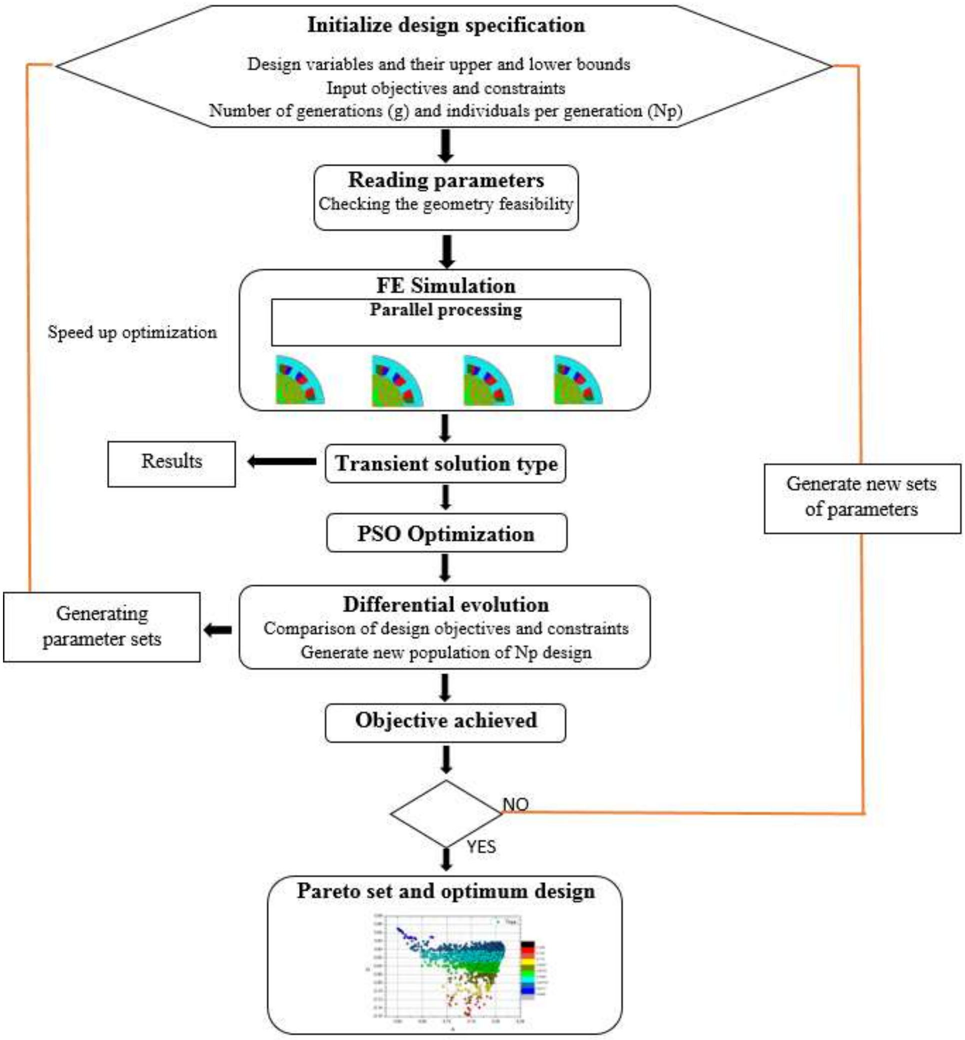

Fig. 2.16 Flowchart of the optimization process

2.6 Conclusions

This chapter reviewed the fundamental working principle of the SynRM. The machines mathematical model, vector diagram, and main design characteristics were discussed. Moreover, different rotor topologies were introduced and compared. A brief comparison of two winding types (concentrated and distributed) were presented. The application of concentrated windings appears to be worthy of investigation by potential manufacturing improvements of the SynRM.

3. Electromagnetic Analysis

It is well-known that the magnetic field characteristics of SynRMs are non-linear, therefore their analysis based on analytical equations is not enough to validate a certain design. Nonetheless, numerical magnetic field computation based on Finite Element Method (FEM) is preferred.

In this chapter, the SynRM motor structure is investigated using FEM sensitivity analysis. First, 2D transient electromagnetic field simulations are performed on different motor topologies. The main goal is to reveal the most important design parameters of the motor topology that affect the machine performances (torque and torque ripple).

3.1. One barrier design proposal

The rotor structure must be flexible, simple and robust enough and, at the same time, easy to be manufactured. Based on [33] all the parameters are shown in Fig. 3.1. This procedure will be used to investigate one-flux and multi-flux barriers effect, mainly on torque maximization and torque ripple reduction

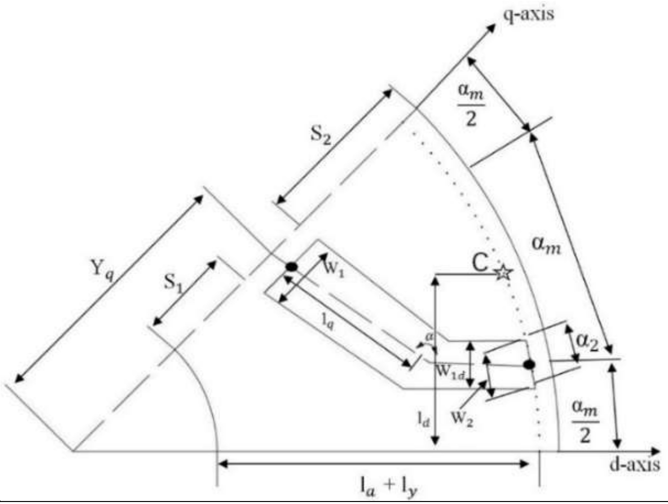

Fig. 3.1 Parameter definition for one barrier sizing and position in d-q axis

where,

Y_d,	radial position of the barrier in the q-axis
S_1, S_2,	iron segment in the q-axis
W_1,	barrier width in the q-axis
W_{1d},	barrier width in the d-axis
l_a,	total air in q-axis
l_d,	total air in d-axis
l_y,	total iron in q-axis

In order to achieve a high saliency ratio, different types of rotor structures such as: single or multi barrier rotor, different rotor lamination (axially or transversally) and slot/pole combination can be employed. Furthermore, to achieve the required saliency ratio, the insulation ratio in the q-axis and d-axis can be calculated according to Fig. 3.1. The amount of the insulation is given by the variables k_{wd} and k_{wq}, respectively, which are explained in (3.1) and (3.2).

The total amount of the insulation is given by the following parameters:

$$k_{wq} = \frac{l_a}{l_y} = \frac{W_1}{S_1 + S_2} \tag{3.1}$$

where, l_y represents the total iron in the q-axis (l_y = S_1+S_2), and l_a is the total air in q-axis (l_a =W_1)

$$k_{wd} = \frac{l_{ad}}{l_y} = \frac{W_{1d}}{l_d - (W_{1d})} \tag{3.2}$$

where, l_{ad} is the total air in d-axis and l_y is the total iron in d-axis.

To find optimum insulation ratio, or the total air in the q-axis (l_a) is a challenge. Rotor topologies with more than two pole pairs have insulation ratio in the d-axis smaller than the insulation ratio in the q-axis.

Independent studies are performed hereafter against a rotor geometry with one flux barrier and multi-flux barriers, in order to investigate the effect of rotor dimensions on the machine performance, mainly average torque and torque ripple. A short description regarding the parameters that are involved in this particular study is presented in

Fig.3.2. Hence, three main parameters are selected, to study their influence: B_{th}(barrier thickness), Y_d (barrier position in q-axis) and α angle which represents the opening angle. Moreover, all these parameters will be investigated by means of FEM and all the SynRMs that are part in this study have the same geometric constraints and operating condition, as given in TABLE 3.1.

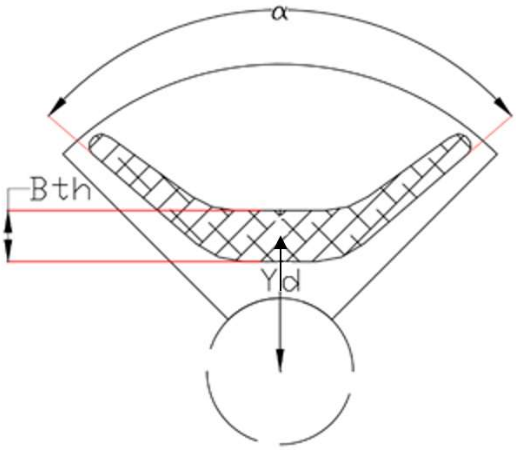

Fig. 3.2 Flux barrier parameters

TABLE 3.1 Main geometrical and electrical parameters for the studied SynRM

Parameter	Units	Quantity
Rated current	A	38
Rated speed	rpm	2700
Outer Stator diameter	mm	119
Outer Rotor diameter	mm	84
Axial Length	mm	17
Topology	-	27-slots/4-pole

A) Analysis on the q-axis barrier thickness influence

Changing the barrier size in the q-axis is done while keeping the Y_d and α fixed. In this situation, B varies between 5 mm (minimum) and 23.5 mm (maximum value). These boundaries of the search intervals are determined to ensure the feasibility of the rotor geometries used for the designs developed in the following sections. Four different barrier widths are considered in order to emphasize the insulation ratio effect, on machine's torque and torque ripple. The obtained results, together with the barrier design for each simulation are exposed in Fig. 3.3. It can be noticed that the maximum average torque is around 0.71 Nm (design nr. 3) and it is obtained for an optimum barrier thickness of 15 mm which is three times bigger than the starting value of 5 mm (design nr. 1). Moreover, the same design has the lowest value in terms of torque ripple 15%, half in comparison with the fourth design where values around 31 % are reported, see Fig. 3.4. When the number of flux barriers is higher, the width of the segments is preferably to be constant for achieving a constant flux density along each segment.

Capturing more flux in the d-axis leads to increase L_d inductance, and directly a higher saliency ratio. However, according to (2.8), saliency is direct dependent on the ratio L_d/L_q and the maximum torque obtained needs maximum possible iron in the rotor structure and this comes with an optimum barrier design.

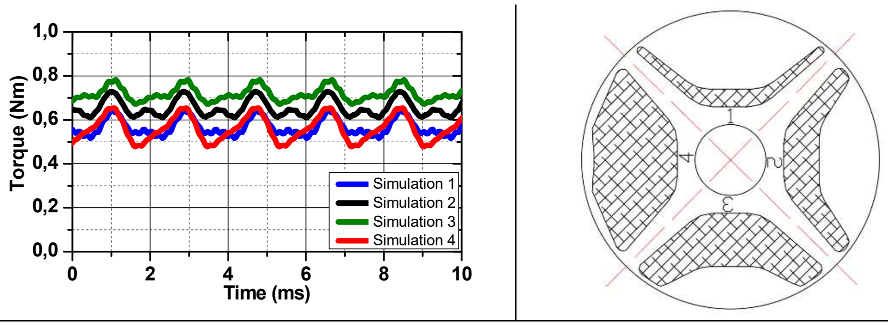

Fig 3.3 Electromagnetic torque for different barrier thickness in q-axis (left) and simulated designs (right)

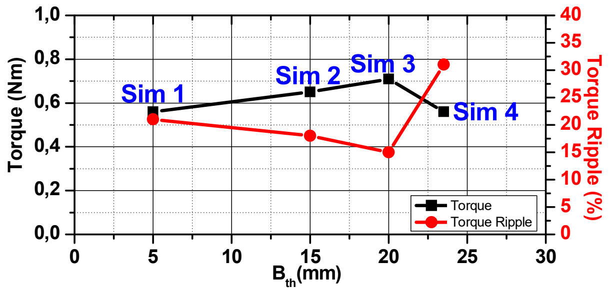

Fig. 3.4 Average torque and torque ripple for all simulated scenarios

B) Barrier position in the q-axis, Y_d parameter influence

In the second part of this study, the barrier position in the q-axis (Y_d) is modified, while B_{th} and α are frozen. A barrier with a constant width along the q-axis, with an Y_d starting point of 18.5 mm to a maximum value of 33.5 mm is analyzed and reported in Fig. 3.5 (left) as well the barrier displacement in the q-axis (right). The obtained torque and barrier geometry are shown in Fig. 3.5 (left) and Fig. 3.5 (right), respectively, when varying Y_d from 18.5 mm to 33.5 mm with an equidistant step. Analyzing the torque performance according Fig. 3.5, it can be noticed that torque sensitivity as function of Y_d between the first and the fourth design does not vary more than 8 %. On the other hand, torque ripple suffers a variation around 19 %. In this case, the optimum value of Y_d is 33.5 mm (the fourth design) where an average value of 0.72 Nm and 21 % torque ripple is registered. Parameter Y_d is an important parameter to achieve the required torque ripple without interference with the average torque.

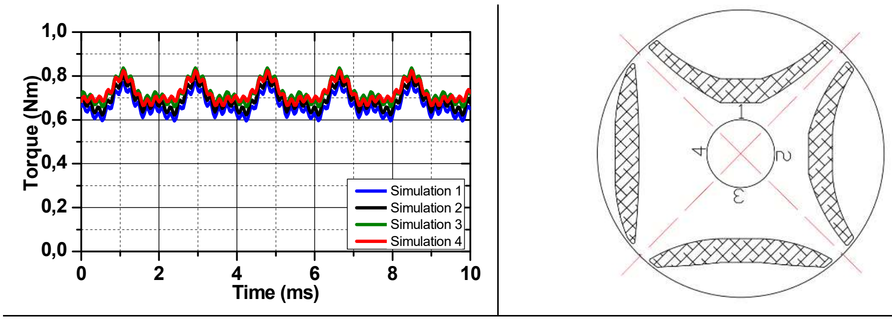

Fig. 3.5 Electromagnetic torque for different barrier position in q-axis (left) and simulated designs (right)

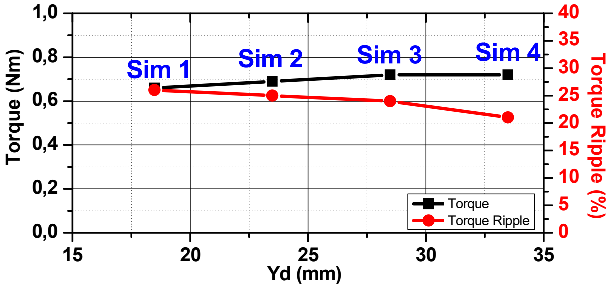

Fig. 3.6 Average torque and torque ripple for all simulated scenarios

C) Barrier α angle, the opening angle influence

The analysis in the last section assumes that the angle α in Fig. 3.7, which seems to be 70° is the best choice. The influence of this angle on machine's torque behavior when B_{th} and Y_d are constant are presented in Fig. 3.8 (left) together with the angle variation on barrier design (right). For this part of the study a variation starting from 80° to 40° is considered. It can be seen in Fig. 2.14 that torque and torque ripple are both affected when this parameter is modified. Torque variations from 0.66 to 0.45 Nm and torque ripple values from 19 % to 27 % are registered.

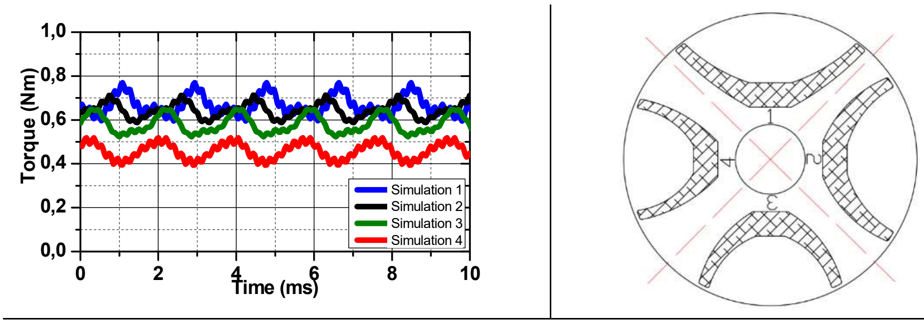

Fig. 3.7 Electromagnetic torque for different barrier angle (left) and simulated designs (right)

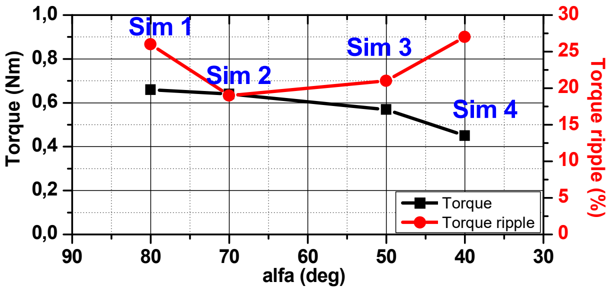

Fig. 3.8 Average torque and torque ripple for all simulated scenarios

3.2. Multi-barriers effect

In the following, the multi-flux barriers effect for SynRM machine will be analyzed, in order to investigate its electromagnetic performance in terms of average torque and torque ripple. To have a fair comparison, according to (3.1) and (3.2), the same insulation ratio is kept for different number of flux barriers. Moreover, the same input parameters, geometrical and electrical in respect to TABLE 3.1 are used.

Increasing the number of barriers reduces the q-axis flux component but at the same time it does not affect the d-axis inductance that much, see Fig. 3.9. Therefore, torque will not go higher if the number of barriers is increased after a certain value, according to Fig. 3.11 more than 4 barriers.

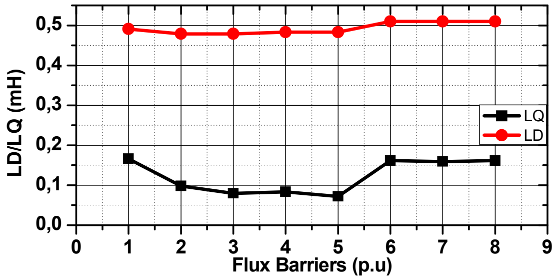

Fig. 3.9 Inductances in d and q-axis for different number of flux barriers

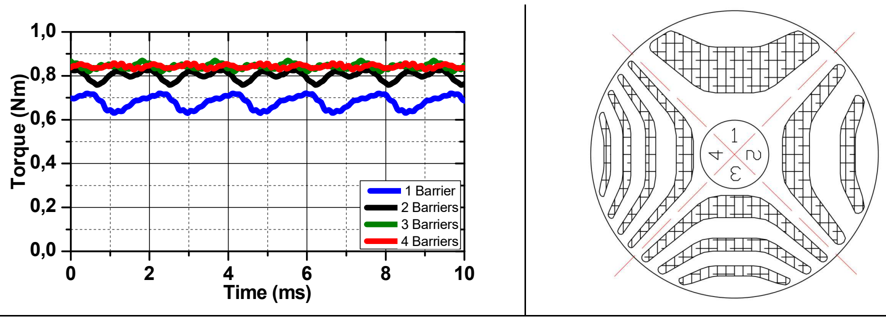

Fig. 3.10 Electromagnetic torque from 1 until 4 flux barriers per pole (left) and simulated designs (right)

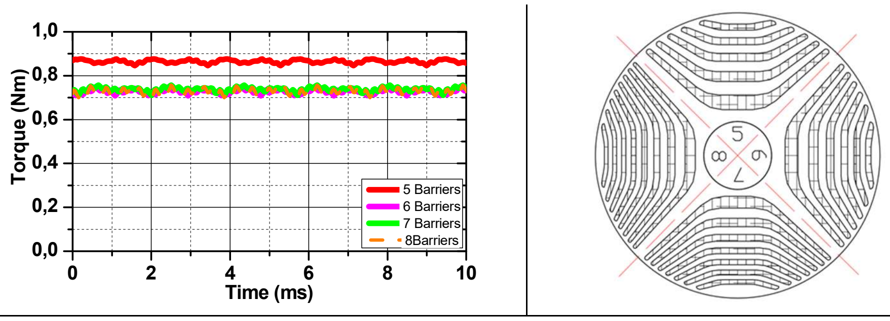

Fig. 3.11 Electromagnetic torque from 5 until 8 flux barriers per pole (left) and simulated designs (right)

According to Fig. 3.12 (b), this ratio expressed as saliency ratio has the same variation as electromagnetic torque, while the number of barriers is increased. Hence, for the highest saliency ratio value of 6.5 corresponds the maximum torque achieved 0.85 Nm by value. On the other hand, small values of torque ripple are registered by increasing the layer number up to a certain value, (maximum 6 layers), see Fig. 3.11.

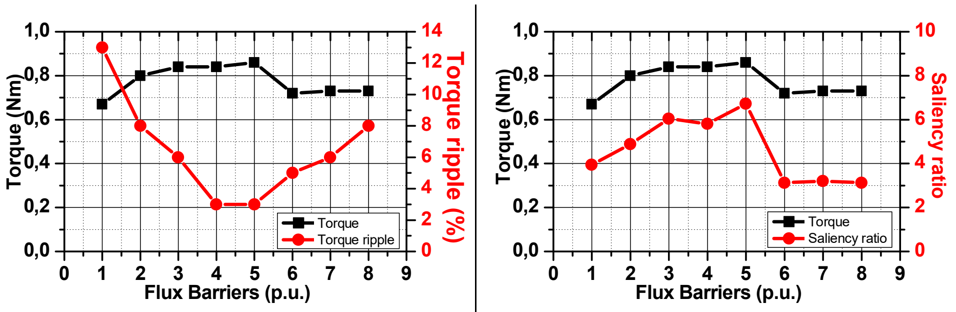

(a) Toque and torque ripple

(b) Torque and saliency ratio

Fig. 3.12 Effect of number of barriers on torque ripple (left) and saliency ratio (right) in respect to electromagnetic torque

3.3. Workflow and reference machine

Currently, in the field of SynRMs design, most of the efforts are being done on proposing different innovative solutions for their distributed winding (integral slot) versions. With few exceptions [25, 26], much less attention is being paid to the CW-SynRM. Therefore, the aim of this thesis is to comprehensively analyze the various attributes of the FSCW-SynRM. For that, at first the influence of key geometry parameters is analyzed by means of optimal design for fully understanding the electromagnetic behavior of the machine. Knowing that a higher electromechanical output directly affects the mechanical robustness of the rotor, special attention is dedicated to the structural aspect. A further topic, which is becoming increasingly important in the context of modern electrical drives, is the NVH-behavior. The latter has been addressed both at theoretical and practical level.

For better understanding the capabilities of the proposed FSCW-SynRM designs, they are compared with the DW-SynRM and ultimately with a FSCW-PMSM. Since the rated characteristics and parameters of the PMSM are used as design specifications, this machine if often referred to as the reference machine. The motivation behind the work is related to the magnet-free structure (and thus low cost of the machine’s active materials) of SynRM and the efforts are being focused on the minimization of its drawbacks. Therefore, to highlight the limitations of this technology, analysis is being carried out for answering the question: What should one undertake to design a FSCW-SynRM with the same output as a PMSM? The answer lies most of the time in either an increased installations space or higher input power. This should be very useful for the final mapping of the SynRMs into the synchronous machines class.

Therefore, a comparative study between eight topologies (concentrated and distributed windings designs) is done by means of FEM electromagnetic analysis, while keeping the same electrical and geometrical parameters in respect to the reference machine, see Fig. 3.13 and TABLE 3.2. Moreover, their key-performance indicators, i.e. power to weight ratio, average torque and torque ripple as well as their speed torque (and -efficiency, respectively) characteristics will be analyzed. For this study, an interior PMSM (IPMSM), spoke design, is used as reference. As design requirements, all SynRM should have the same outer diameter D_{out}, and the same length on Z-axis L_{stk} as the reference machine. Furthermore, the input power should be the same, i.e. battery voltage and RMS phase current. The cross section along with the requirements and specification of a 300 W (DC input power) drive used for a car`s cooling fan is shown in Fig. 3.13. All the parameters along with their values are listed in TABLE 3.2.

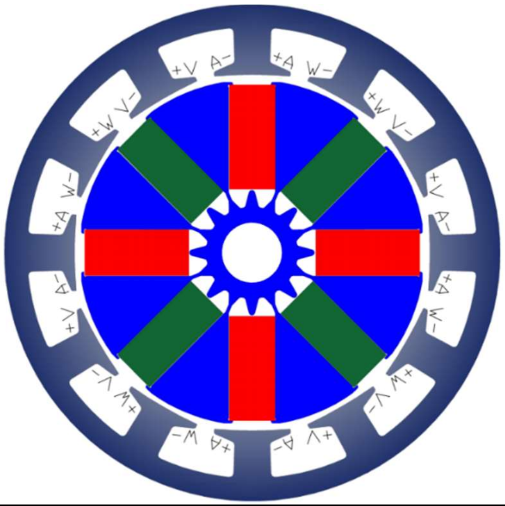

Fig. 3.13 Cross-section of the analyzed PMSM-spoke design

TABLE 3.2 Configurations, magnetic materials and electrical circuit parameters of the reference motor

Name	Value	Unit
Number of stator slots	12	-
Number of rotor poles	8	-
PM material	Ferrite	-
PM remanence B_r	0.4	T
Radial air-gap width	0.6	mm
Winding connection	delta	-
Wire diameter	1.18	mm
Number of turns	22	-
Number of parallel paths	2	-
Phase resistance	8.8	mΩ
Stack length	18	mm
Battery voltage DC-Link	13	V
RMS phase current	17	A
Rated speed Ω_b	2700	rpm
Rated torque T_b	0.85	Nm
Torque ripple T_{ripple}	9	%

3.4 Design of SynRM with concentrated windings

The machines under study, shown in Fig. 3.14, have been modelled using the electromechanical software package, provided by

ANSYS. This application details the simulation of an electrical machine by means of two-dimensional (2D) FE-models. In order to investigate the influence of slot/pole number combinations on electromagnetic performance of SynRM machine, the design parameters (rotor and stator) of each machine have been optimized to have the maximum torque and the lower value of torque ripple according to the constraints mentioned above. Several methods of optimization such as genetic algorithm and particle swarm optimization algorithm are used to achieve the best design (see appendices A). The geometry of the rotor lamination (number of flux barriers and their shape design) has been optimized to meet the maximum saliency ratio.

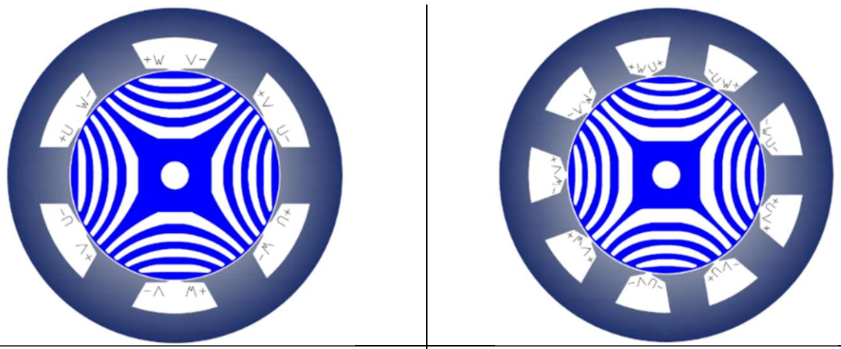

SynRM 6 slots 4 poles design | SynRM 9 slots 4 poles design

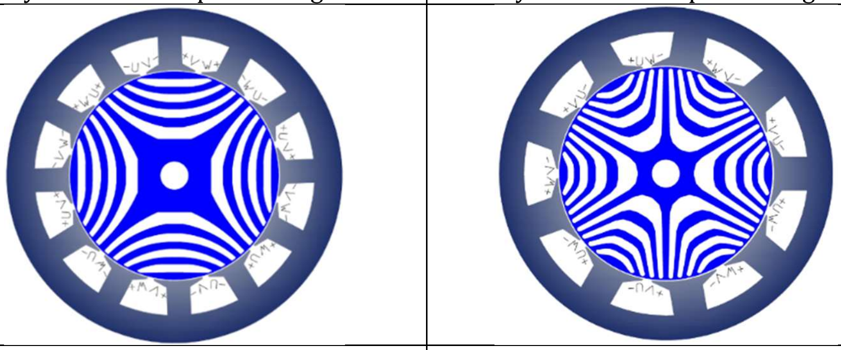

SynRM 12 slots 4 poles design | SynRM 9 slots 6 poles design

Fig. 3.14 Cross section of the analyzed SynRMs

SynRMs are using two types of materials for their construction. In this situation the materials assigned for this simulation are:

- Laminated steel M800_50A for the stator and rotor cores;
- Copper for coils;

Furthermore, Fig. 3.15 shows the maximum number of turns per slot calculated for each machine and the calculated filling factor.

The filing factor k_{Cu} is defined as the ratio of total wire cross section and the effective slot area (blue border) A_{eff}, which is the total slot are, A_{slot}, minus the cross section occupied by the insulation.

The filing factor is calculated based on:

$$k_{cu} = \frac{n_{wire} \cdot S}{A_{eff}} \tag{3.3}$$

where n_{wire} is the number of wires within the slot, S is the wire section including the insulation.

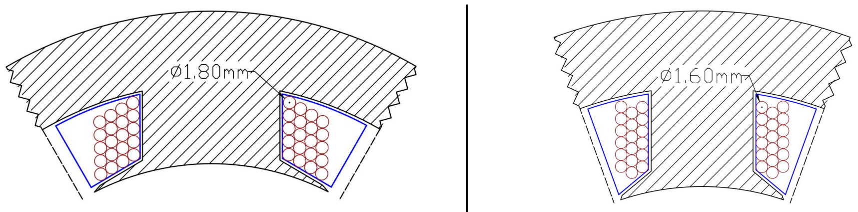

6 slots 4 poles design | 9 slots 4 poles design

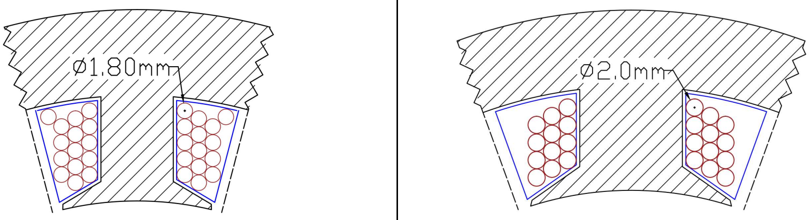

12 slots 4 poles design | 9 slots 6 poles design

Fig. 3.15 Maximum number of turns per slot

The wire diameter was chosen in order to obtain the minimum phase resistance in order to minimize the copper losses.

The winding parameters are summarized in TABLE 3.3

TABLE 3.3 Winding parameters for CW-SynRM

Topology	6s/4p	9s/4p	12s/4p	9s/6p
Phase Resistance Ω	0,0172	0,0217	0,0151	0,0289
Wire diameter mm	1.8	1.6	1.8	2
Nr. turns/slot	19	18	15	12
Filling factor	0.48	0.52	0.63	0.49
Total copper mass	170 gr.	140 gr.	150 gr.	250 gr.

Electromagnetic FEM simulations are done while using an external current source operation. External winding type enables users to assign excitations directly from either Maxwell Circuit Editor, or Simplorer (both ANSYS external coupling software's). The circuit diagram is presented in Fig. 3.16 where, (I_A, I_B, I_C) is the sinusoidal current source, (L_{Phase_A}, L_{Phase_B}, L_{Phase_C}) are the winding inductances and (R_A, R_B, R_C) are the winding resistances.

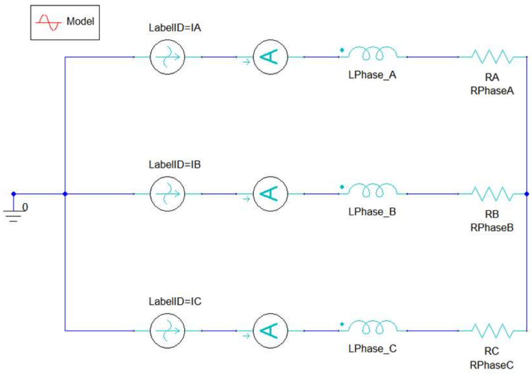

Fig. 3.16 Circuit diagram of the current source simulation method

The mesh used for the FEA is given in Fig. 3.17 a. A moving band around the airgap was created. In order to increase the number of elements between the moving band and the stator, another two "moving bands" before and after the original moving band are added, which will lead to a numerically efficient meshing method. The number of elements is calculated according to the number of rotor poles and number of calculation steps during a complete electrical period. In Fig. 3.17 b the mesh in the air-gap region is illustrated.

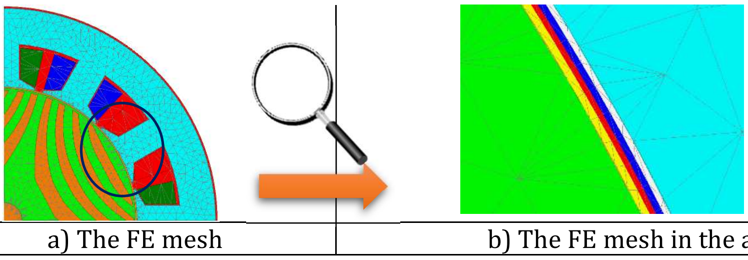

a) The FE mesh | b) The FE mesh in the airgap

Fig. 3.17 The mesh in the air-gap region

As it can be seen, the air-gap region was divided in three layers (yellow, red and blue) in order to achieve an accurate computation of the electromagnetic torque. The flux lines and flux density distribution in the cross-section for all four-concentrated winding SynRMs structure in the aligned position of the rotor are given in Fig. 3.18. The flux density (B) values in different regions are illustrated in order to show which part from both, rotor and stator structure is affected by the saturation.

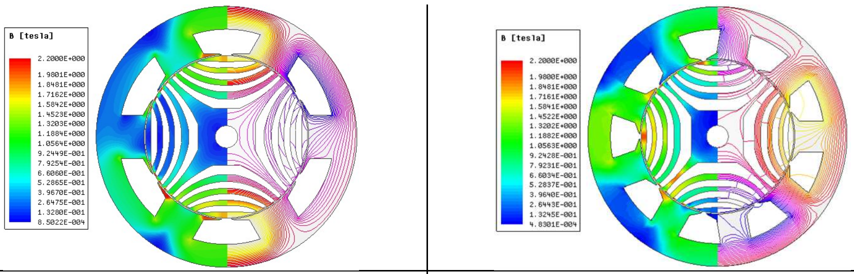

SynRM 6 slots 4 poles design | SynRM 9 slots 4 poles design

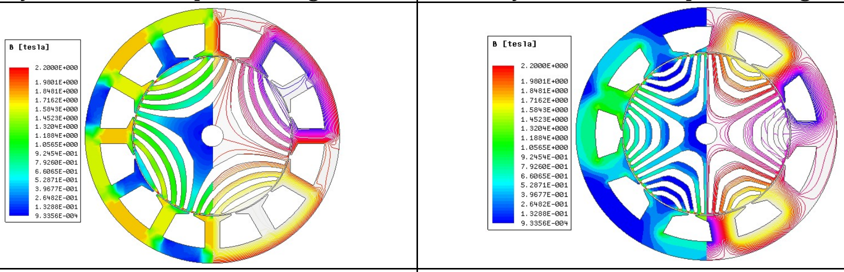

SynRM 12 slots 4 poles design | SynRM 9 slots 6 poles design

Fig. 3.18 Flux density and flux lines in aligned position at RMS phase current 17A

There are several ways to compare the performances of electrical machines. Here, constant torque condition for a certain speed range (2700 rpm) is proposed. The machines performance with the same winding structure, electromagnetic torque and efficiency is also calculated to compare the effect of pole number on d- and q- axis inductances. The dominant losses in the machines are the copper losses and at constant current it is expected that all four topologies will have almost the same temperature and temperature rise.

3.4.1. Torque performances of the proposed SynRM with CW

The output torque is set to a constant value until 2700 rpm for all four CW-SynRMs. The reluctance machine current source excitation in this condition has the same value as the corresponding PMSM, see TABLE 3.5. The simulation results are summarized in Figure 3.19 (a) and (b). As it can be seen, the 12 slots 4-pole topology has the highest average torque over the entire speed range, and the 9 slots 6-pole topology exhibits the lowest average value of the electromagnetic torque. Increasing the number of pole pairs reduces the power factor and the saliency ratio due to the negative effect of the magnetizing current that is needed for a higher pole number of machines [33], [75]. By means of torque ripple as a percentage of the average torque the 9 slots 4-pole design has the minimum value of 24 % and at the other end a value of 96 % is given by the 6 slots 4-pole topology. The torque versus speed characteristic is computed using FE analysis combined with analytical computation and corresponds to the rated current. The machine speed increases until the voltage limit is reached, which is at the base speed (2700 rpm) at the end of the constant torque region.

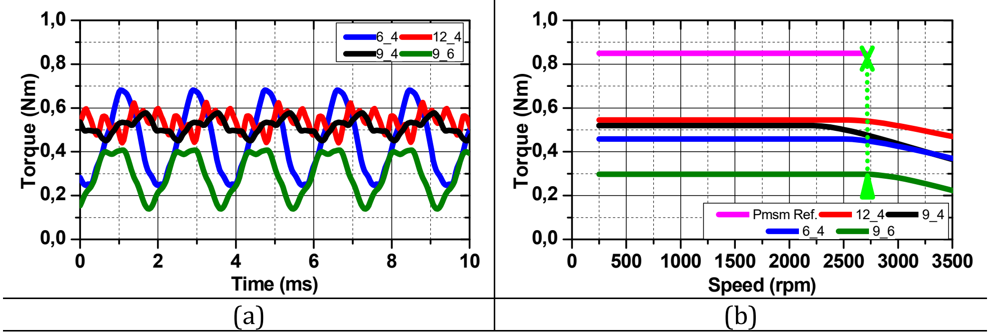

(a) (b)

Fig. 3.19 Electromagnetic torque waveforms (a) and torque vs speed for rated current limit (b)

The machine stator current angle varies between 40^0 and 45^0 electrical degrees (depending on the topology) and represents the optimal α_i^e angle (see Fig. 3.20) where the maximum torque can be achieved by the SynRMs. Fig. 3.21 shows the torque delivered by the SynRMs versus the current angle α_i^e, at different values of the stator current. To take notice of the saturation effect on the torque variations, the calculations are performed for three values of the stator current 24A 36A and 48A.

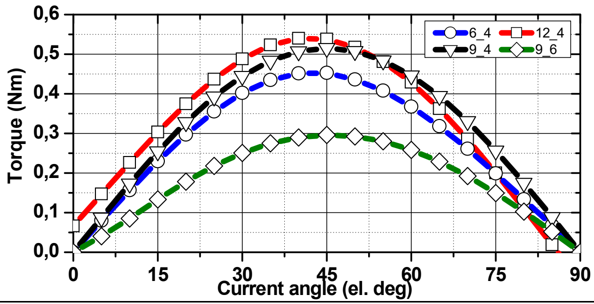

Fig. 3.20 Electromagnetic torque vs current angle, optimum current angle

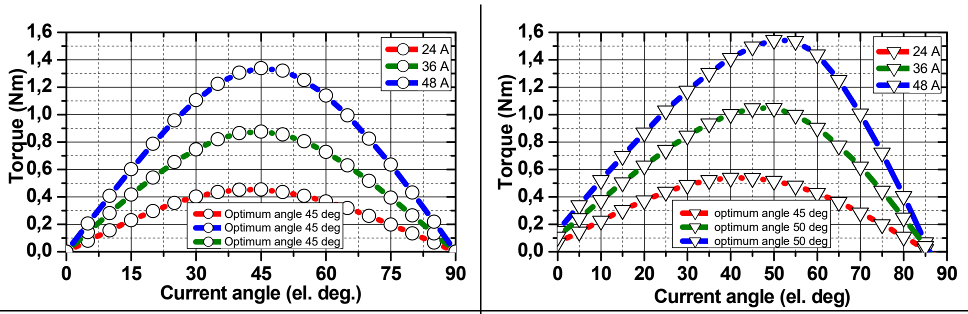

6 slots 4-poles design

9 slots 4-poles design

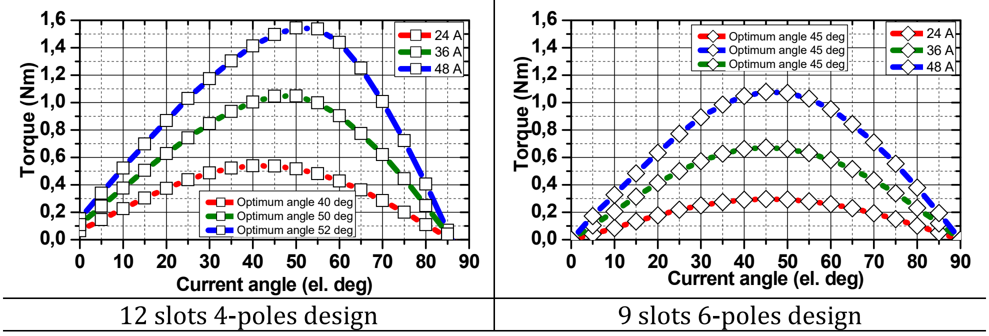

12 slots 4-poles design

9 slots 6-poles design

Fig. 3.21 Torque versus current angle, for different stator current amplitude

A disadvantage of the SynRM is the poor power factor, see Fig. 3.22. From the figure, the power factor is directly related to the saliency ration of the machine. Thus, a higher value of saliency ratio gives a high-power factor. In this situation, using concentrated winding, the SynRM has a power factor between 0.4 and 0.64 under maximum torque per Ampere condition. The superiority of the 12 slots 4– pole topology results from the saliency ratio (equal to 3.9). Thus, it has the highest power factor and a good efficiency vs. speed characteristic (neglecting iron and copper losses). It has to be specified that the saliency ratio in CW-SynRM is lower compared to distributed windings due to the high stator leakage inductance [70].

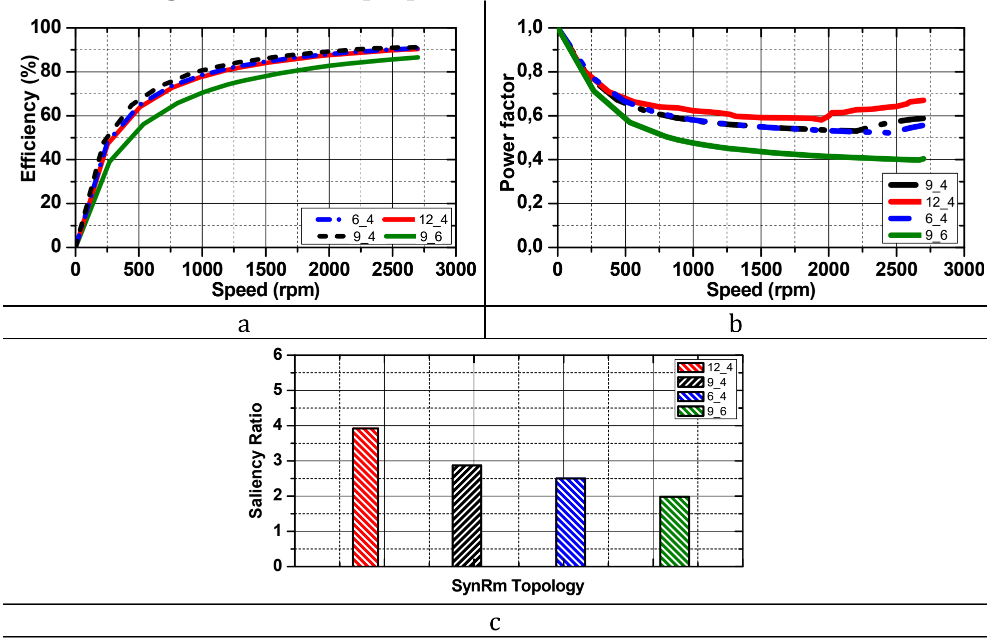

Fig. 3.22 Calculated Efficiency vs Speed characteristic, Power Factor (b) and Saliency Ratio (c), for rated current

It is a well-known fact that achieving both high efficiency and high-power factor is difficult (and costly) for low-power machines. However, the power factor is proportional with the machines power rating and for low power drives a low power factor is experienced. Therefore, to reach the same performances a larger reactive energy is needed, and the size of the required inverter increases proportionally.

3.4.2. Inductances computation and saturation effect

The machine inductances are calculated using FEA and a detailed analysis and comparison of their dependence with the saturation is presented in Fig 3.23. Here, the stator is aligned with phase-A and the rotor is rotated into d- and q- axis position. For each machine the inductances L_d and L_q for a range of current between 0 to 70 A are calculated (three times higher than the rated current). This method allows the computation of the machines d- and q-axis inductances as a function of current.

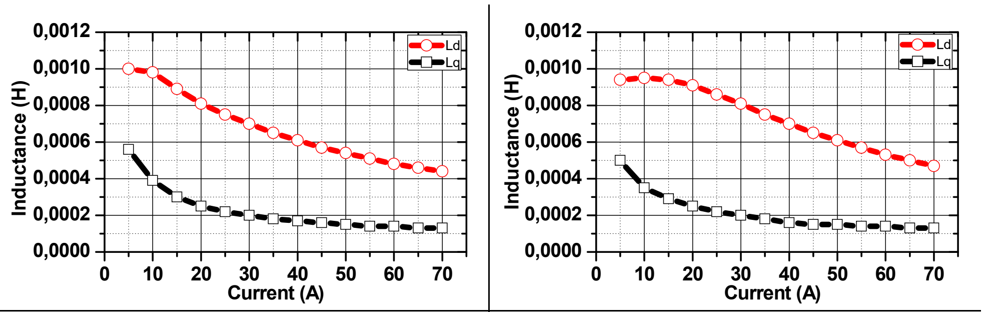

6 slots 4-poles design

9 slots 4-poles design

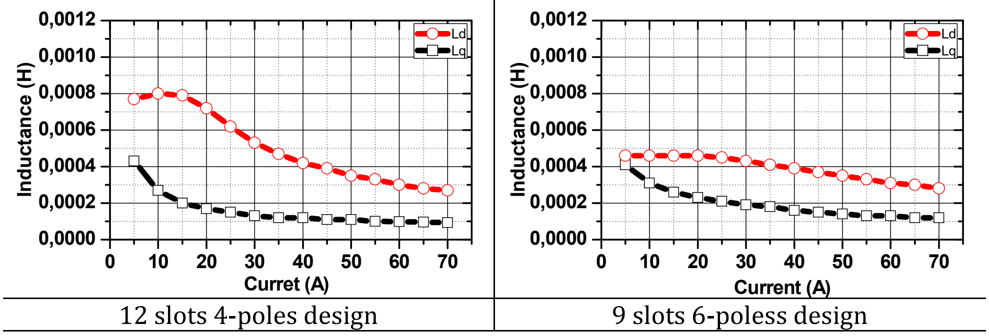

12 slots 4-poles design

9 slots 6-poless design

Fig. 3.23 FEA calculated d- and q-axis inductances

3.4.3. Iron and copper losses

All four SynRM topologies will be compared in this section from iron losses point of view, by considering the same lamination material. The specific core losses data of the electrical steel used, namely M800-50 A is described in Fig. 3.24.

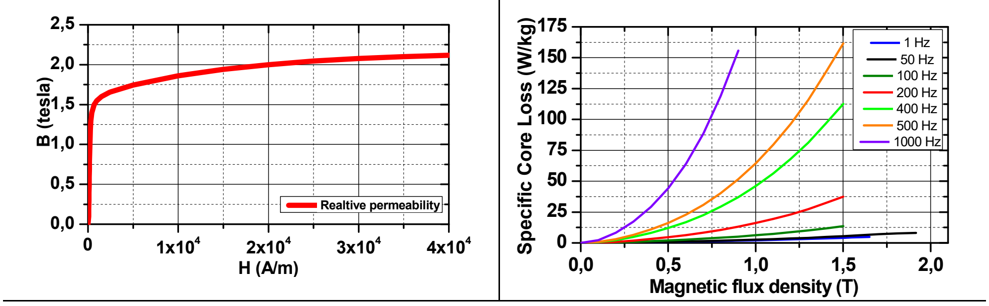

Fig. 3.24 BH-Curve and the Specific core losses versus magnetic flux density plots for M800-50A lamination

In Fig. 3.25 core losses calculation considering the same lamination material and operating conditions were performed by means of FEA software. The comparison of iron losses is done to 2700 r/min speed (rated speed).

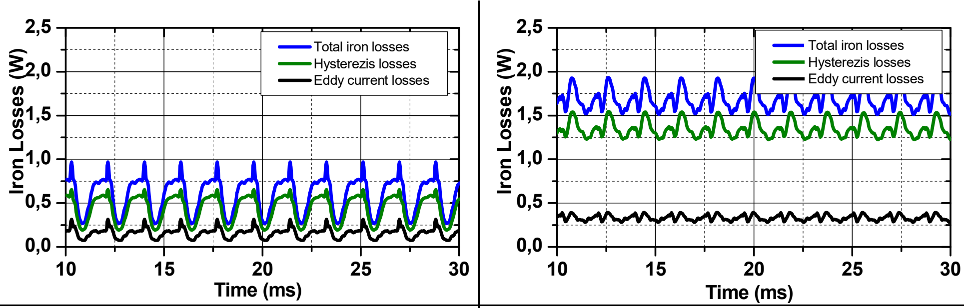

6 slots 4-poles design

9 slots 4-poles design

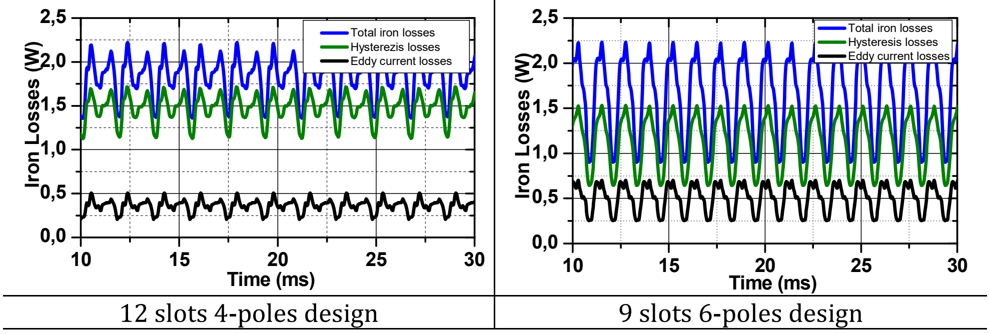

12 slots 4-poles design

9 slots 6-poles design

Fig. 3.25 Iron core losses results

The results given in Fig. 3.25 are showing that the 6 slots 4-poles topology exhibits the lower iron losses than 12 slots – 4 poles configuration. This is mainly due to the fact that the fundamental frequency of the magnetic field of the 6 slots 4-poles topology is half than the 12 slots one. Overall, it is clear that the maximum value of iron losses for all four topologies is less than 15% per topology. However, when considering a higher speed application, it can be expected that iron losses become higher. Total losses (neglecting mechanical losses) are shown in TABLE 3.4.

TABLE 3.4 Total losses (neglecting mechanical losses)

Topology	6s/4p	9s/4p	12s/4p	9s/6p
Copper losses [W]	14.91	18.7	13	25
Iron losses [W]	0.7	1.5	1.66	1.5
Total losses [W]	15.61	20.2	14.66	26.5

3.5. SynRM design with distributed windings

A similar procedure will be used in this section to simulate the proposed DW-SynRM in order to investigate each topology performance using the same constraints (electrical and geometrical parameters) mentioned above in this chapter. Thus, three SynRM machines with different stator slot number but the same rotor pole configuration (4 poles) are shown in Fig. 3.26. The fourth topology employs a distributed winding stator with 27 slots, but this time a higher number of poles (6 poles) was considered.

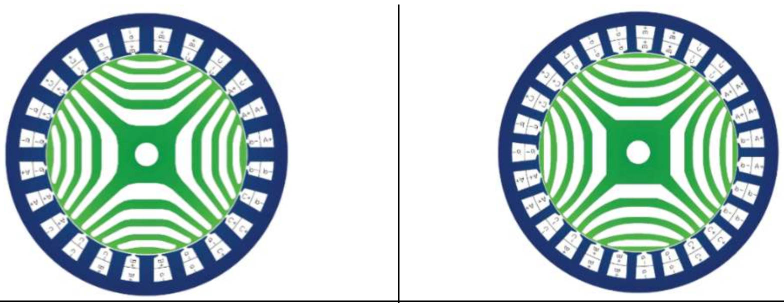

SynRM 24 slots 4 poles design

SynRM 27 slots 4 poles design

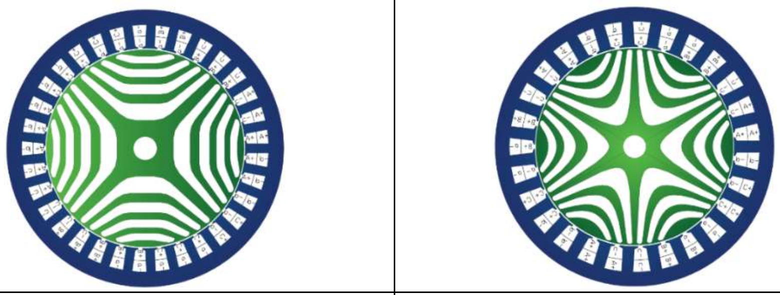

SynRM 33 slots 4 poles design

SynRM 27 slots 6 poles design

Fig. 3.26 Cross section of the analyzed DW-SynRMs

For a machine with distributed windings, the shape of the airgap MMF is closer to a sinusoid and it leads to a reduced harmonic content of the air-gap magnetic field, increasing the value of the fundamental winding factor. Most of the studies on SynRM are focused on structures with distributed winding type and they are preferred in many applications instead of concentrated type, due to their higher torque density and lower torque ripple. Nowadays, different manufacturing techniques are used for this winding arrangement. From needle winding (< 2.5 mm diameter) to a fast-individual coil automatized process.

However, from the geometry of the windings, there are several observations that can discussed:

- Leakage inductances due to the end windings
- Overlapping of the coils
- Complex geometry of the coils
- End windings and their impact on the axial length of the machine.

Further, Fig. 3.26 and TABLE 3.5 show the maximum number of turns per slot calculated for each topology and the best filling factor obtained for this type of winding.

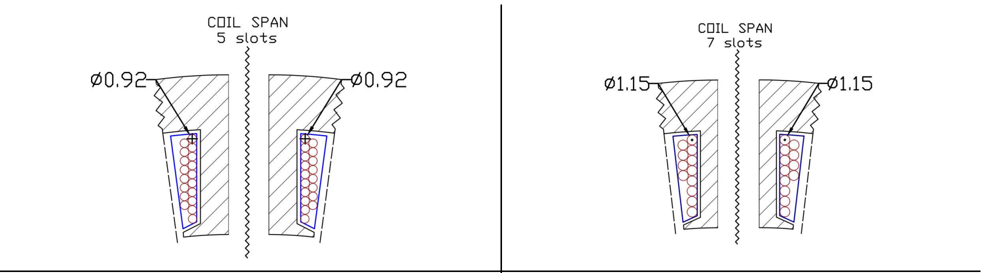

24 slots 4 poles design | 27 slots 4 poles design

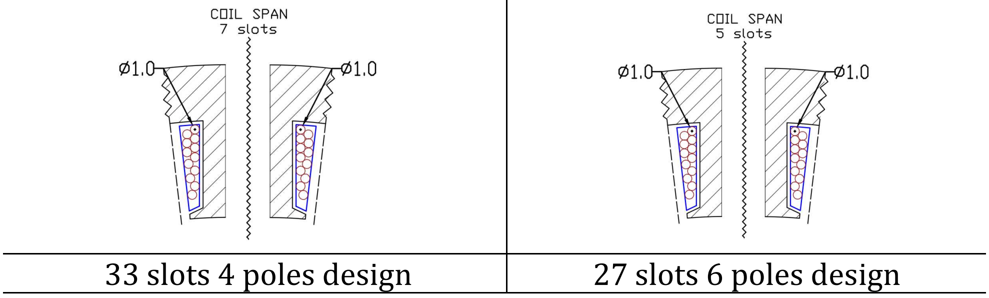

33 slots 4 poles design | 27 slots 6 poles design

Fig. 3.27 Maximum number of turns per slot

TABLE 3.5 Winding parameters for DW-SynRM

Topology	24s/4p	27s/4p	27s/6p	33s/4p
Phase Resistance Ω	0,0568	0,0273	0,0337	0,0309
Wire diameter mm	1.6	2	1.8	1.8
Nr. turns/slot	6	4	4	3
Eq. wire mm	***0.92***	***1.15***	***1***	***1***
Parallel cond./turn	***3***	***3***	***3***	***3***
Filling factor	0.61	0.54	0.59	0.56
Total copper mass	360 gr.	440 gr.	340 gr.	340 gr.

To achieve a maximum filling factor while still having a low-cost and robust manufacturing process, the wires that are forming a coil have been recalculated, and an equivalent number of wires for each coil has been recomputed, as it can be seen in Table 3.5. The flux lines and the magnetic flux density distribution, respectively, for all DW- SynRMs topologies in aligned position of the rotor are given in Fig. 3.28.

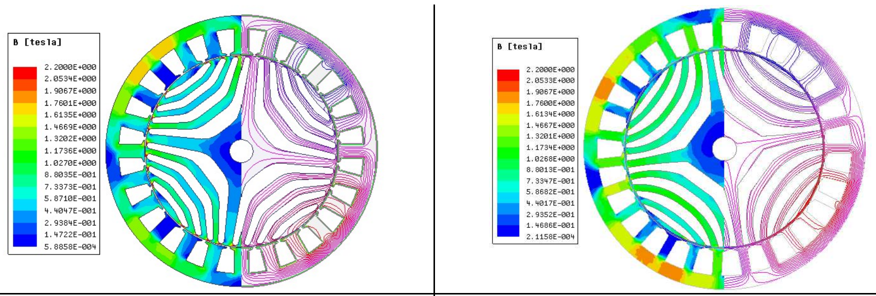

SynRM 24 slots 4 poles design

SynRM 27 slots 4 poles design

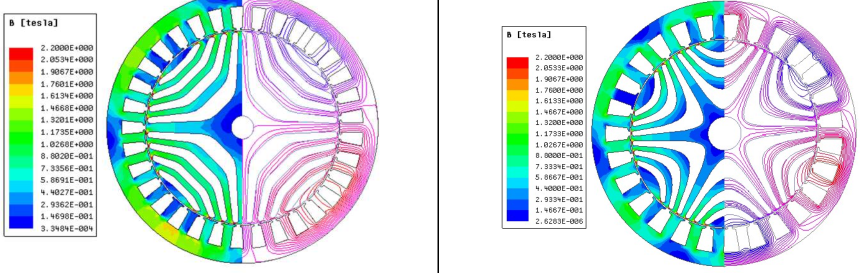

SynRM 33 slots 4 poles design

SynRM 27 slots 6 poles design

Fig. 3.28 Magnetic field density and flux lines in aligned position at RMS phase

3.5.1. Torque performances of the proposed SynRM with DW

In this section, DW-topologies have been analyzed in order to evaluate their electromagnetic performances for the same output parameters mentioned above and under the same simulation conditions the. The computed torque and torque versus speed characteristic for each DW-SynRM is shown in Fig. 3.31 a and b. It can be noticed that distributed winding type is superior to concentrated winding due to a better torque ripple content. Higher torque density and lower value of torque ripple are the main reasons to prefer DW instead of CW-designs. However, taking into consideration the obtained results, not all the topologies have scored the credits mentioned above. For instance, the 27 slots 6 pole design exhibits an average value of 0.35 Nm, close to the 9 slots 6 pole CW- design. Therefore, it can be stated that increasing the number of poles for both winding configurations, will not lead to a better torque performance.

If we summarize Fig. 3.29 a, the highest electromagnetic torque is obtained by the 24 slots 4 pole design, with an average value of 0.64 Nm. On the other hand, this design exhibits the highest level of torque ripple, 43 %, in comparison to the 33 slots 4 pole design, where a value of 2 % torque ripple is registered for a 23 % smaller value of the average torque. The only design that exhibits good torque performances is the 27 slots 4 pole, with an average torque of 0.6 Nm and an acceptable level of 6 % torque ripple. In Fig. 3.29 b, the torque versus speed characteristic is plotted. -

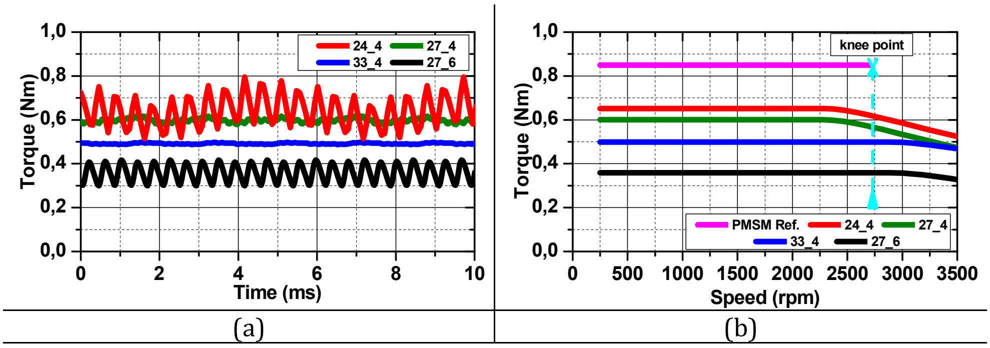

(a) (b)

Figure 3.29 Electromagnetic torque waveforms (a) and torque vs speed for rated current limit (b)

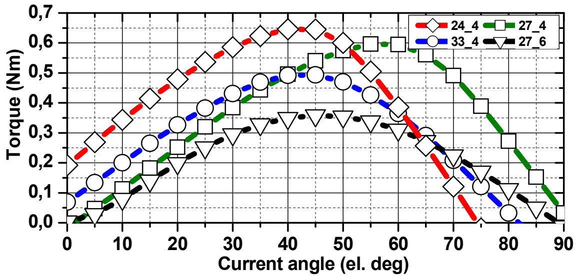

Fig. 3.30 Electromagnetic torque vs current angle, optimum current angle

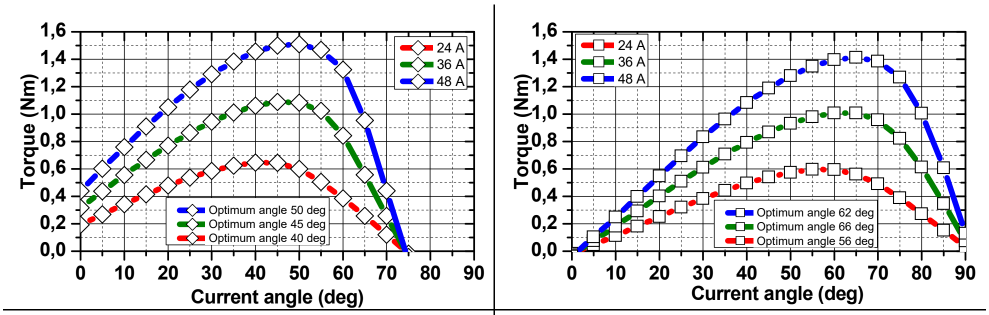

24slots 4-poles design

27 slots 4-poles design

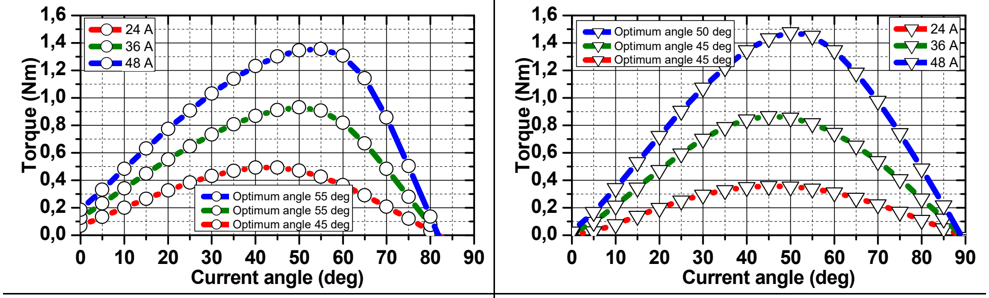

33 slots 4-poles design

27 slots 6-poles design

Fig. 3.31 Torque versus current angle, varying the stator current amplitude

In what concerns the efficiency, in Fig. 3.32 a, it can be noticed that all topologies have almost the same efficiency value more or less equal to 85 % except the 27 slots 6 pole design, which reaches an efficiency at the operating point less than 80 %. The maximum torque per ampere strategy is used to increase the SynRM efficiency. Consequently, an important problem as a drawback is the poor machine power factor. This disadvantage could lead to over-size the inverter, in conclusion the overall costs of the system.

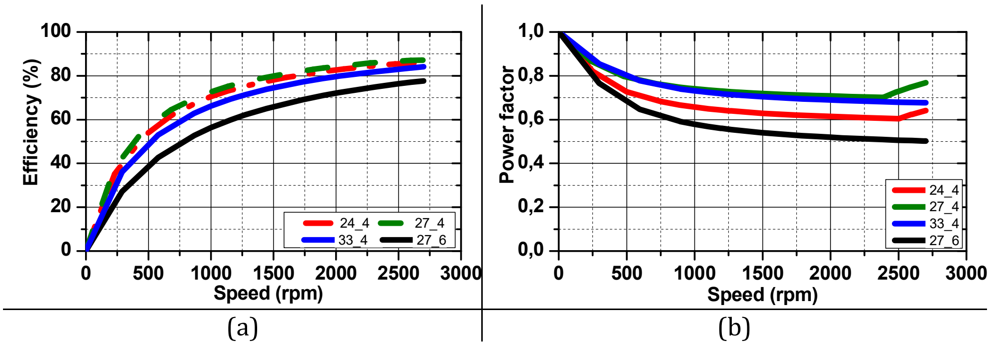

(a)

(b)

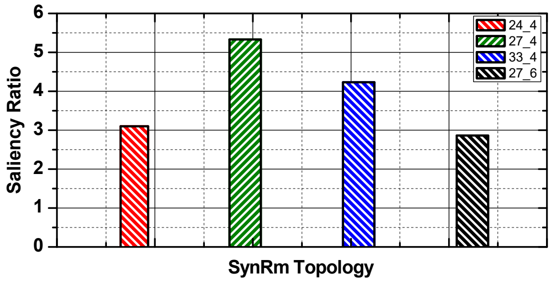

(c)

Fig. 3.32 Calculated Efficiency vs Speed characteristic, Power Factor (b) and Saliency Ratio (c), for rated current

3.5.2 Inductances computation and saturation effect

The DW-SynRM d- and q-axis inductances were calculated by applying the same method used for CW-SynRM designs. The obtained results are shown in Fig. 3.33.

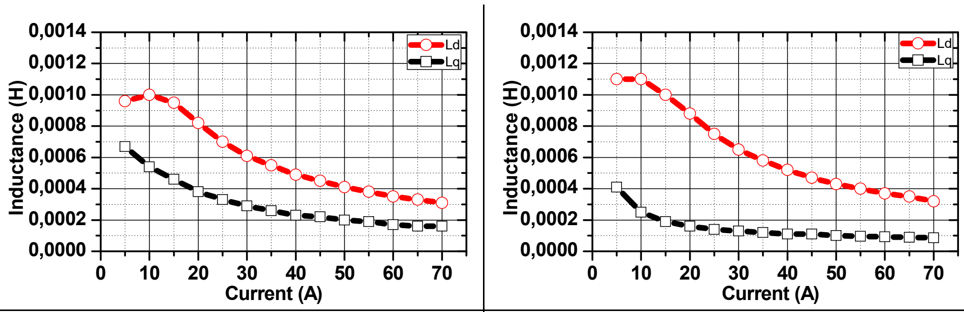

24 slots 4-poles design

27 slots 4-poles design

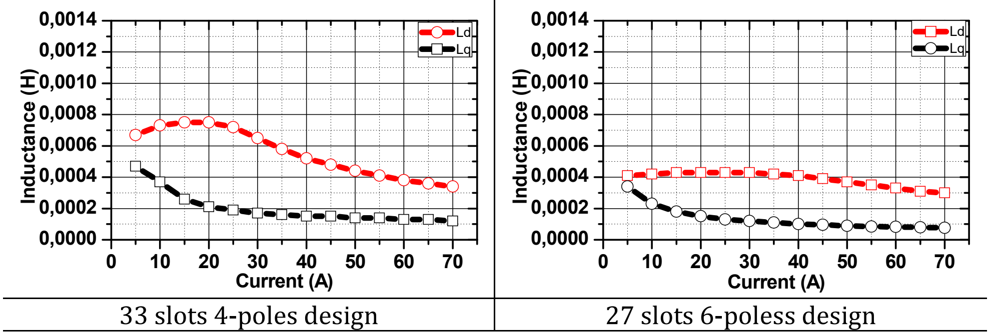

33 slots 4-poles design

27 slots 6-poless design

Fig. 3.33 FEA calculated d- and q-axis inductances

3.5.3 Iron and copper losses

In Fig. 3.34 core loss calculation considering the same lamination material and operating conditions were performed by means of FEA software. The comparison of iron losses is done to 2700 r/min speed (rated speed).

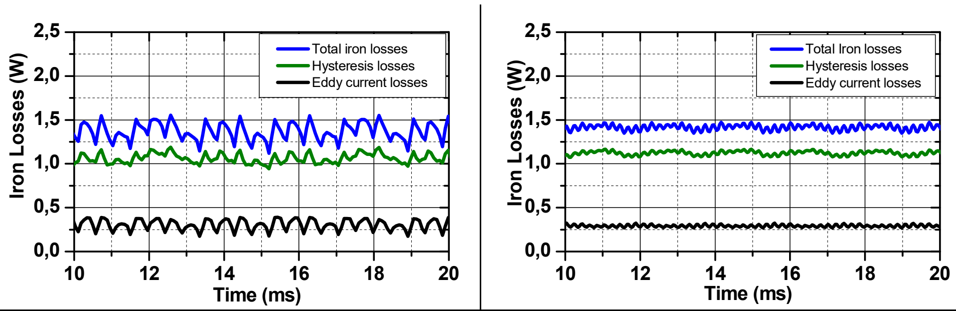

24 slots 4-poles design | 27 slots 4-poles design

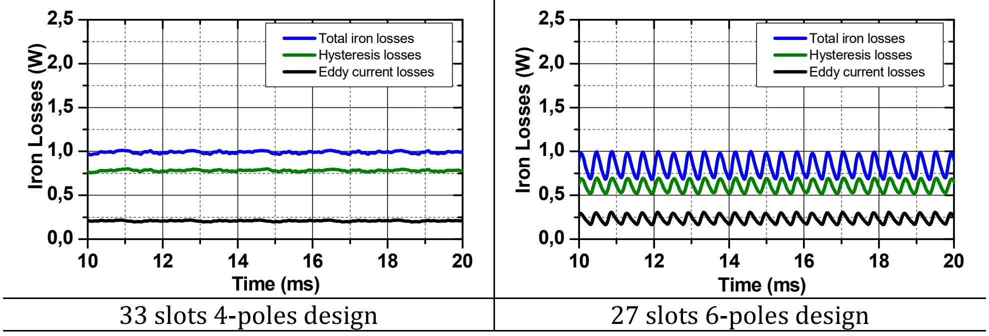

33 slots 4-poles design | 27 slots 6-poles design

Fig. 3.34 Iron core losses results

The results given in Fig. 3.34 are showing that the 27 slots 6-poles topology exhibits the lower values of iron losses. On the other hand, the 27/4 and 24/4 have the highest total iron losses, equal to 1.4 W. Both hysteresis and eddy current losses are analyzed as well for each topology individually.

TABLE 3.6 Total losses (neglecting mechanical losses)

Topology	24s/4p	27s/4p	33s/4p	27s/6p
Copper losses [W]	49.1	23.6	26.7	29.1
Iron losses [W]	1.17	1.19	0.82	0.8
Total losses [W]	50.27	24.79	27.52	29.9

3.6 Performance comparison

If maximum torque capability, minimum torque ripple and maximum power factor represents the main goals for designing a SynRM for the targeted application, a further study will be performed by selecting the best design from each winding topology. By results given in Table 3.8, the 12 slots 4 pole concentrated winding and 27 slots 4 pole distributed winding will be further investigated.

The chosen geometries can still be improved by some fine-tuning ideas. This tuning is basically focused on adjusting the shape of the flux barriers in order to achieve more saliency ratio and in the end a better power factor and higher torque density. Performance comparison between all eight SynRM topologies is shown in TABLE 3.7

TABLE 3.7 Performance comparison for different slot/pole combination

Design type	SynRM CW	SynRM CW	SynRM CW	SynRM CW	SynRM DW	SynRM DW	SynRM DW	SynRM DW
Slots Nr.	6	9	12	9	24	27	27	33
Poles Nr.	4	4	4	6	4	4	6	4
DC voltage [V]	13	13	13	13	13	13	13	13
I rms [A]	17	17	17	17	17	17	17	17
Speed rpm	2700	2700	2700	2700	2700	2700	2700	2700
Length [mm]	18	18	18	18	18	18	18	18
turns/slot	19	18	15	12	6	4	4	3
Parallel branches	1	1	1	1	1	1	1	1
Winding type	Y	Y	Y	Y	Y	Y	Y	Y
Winding factor	0.866	0.617	0.5	0.866	0.966	0.954	0.945	0.954
Filling factor	0.48	0.52	0.63	0.49	0.61	0.54	0.59	0.56
Phase resistance [Ω]	0.0172	0.0217	0.0151	0.0289	0.0568	0.0273	0.0337	0.0309

Air-gap [mm]	0.5	0.5	0.5	0.5	0.5	0.5	0.5	0.5
Saliency ratio	2.5	2.87	3.92	2.5	3.1	5.33	2.86	4.23
Iron losses [W]	0.7	1.5	1.66	1.5	1.17	1.19	0.82	0.8
Copper losses [W]	14.91	18.7	13	25	49.1	23.6	26.7	29.1
Total losses [W]	15.61	20.2	14.66	26.5	50.27	24.79	27.52	29.9
Shaft torque [Nm]	0.45	0.48	0.54	0.3	0.64	0.6	0.35	0.5
Torque ripple [%]	96	24	30	87	43	6	32	2
Power factor	0.5	0.58	0.66	0.4	0.64	0.76	0.5	0.67
Efficiency [%]	89	89	88	88	86	87	79	85

3.7 Best design assessment further investigation

As it was mentioned above, a comparison between best designs obtained, one with concentrated and other with distributed winding is further investigated. The comparison is performed highlighting various key performances indicators both electromagnetic (e.g. torque density and quality) and electromechanical level (e.g. torque/efficiency speed characteristics).

Moreover, both SynRMs will be developed as experimental models, there are some manufacturing requirements, which must be followed. The manufacturer requests a filling factor equal or smaller to 0.45 because the manufacturing motor winding will not employ any automated techniques and the entire winding process will be done manually. Another requirement is the current density (J) in the stator slots. The minimum J value should be equal or less than 6e+6 (A/m2). In consequence, the stator geometry of both designs and the winding resistance will be recalculated according to these constraints.

3.7.1. Re-optimization process

In this section, the analysis is done by allowing both the current and the stack length to exceed the PMSM geometrical and electrical constraints. The only constraint is the outer diameter. Both topologies have been re-analyzed and re-optimized by taking into consideration the manufacturing limitations and torque performance requirements. Afterward, the promising designs are analyzed and used in comparison to the reference PMSM.

A high filling factor is an inherent part to any optimal machine. An approach to achieve the minimum imposed filling factor is done by optimizing the slot area but keeping the same torque quality. An artificial intelligence-based approach using Particle Swarm Optimization (PSO) coupled with FEM models is used for the characterization and design optimization for both SynRMs. A pragmatic two steps approach has been adopted. In the first step, the optimization is performed just on the stator side, whereas in the second step the whole motor is optimized by means of transient FE computation. To do this, two parameters of the stator structure T_Th0 (tooth thickness) and T_Hs1 (tooth height), (for rotor and stator design parameters see Appendices 1) were chosen. In Fig. 3.35 a, the torque variation as function of tooth parameters can be seen.

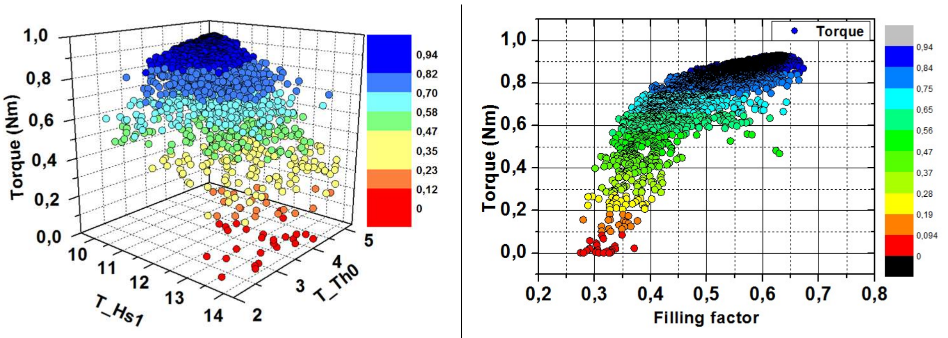

(a) (b)

Fig. 3.35 Stator parameters variation (a) filling factor optimization (b)

Finally, a Pareto-front is obtained, Fig. 3.35 b, with the optimum filling factor and the maximum number of turns. After optimization, from the obtained Pareto-front, the new optimal stator slot geometries are chosen having different number of turns and wire diameter, see TABLE 3.8. It can be observed that the stack length for the 12 slots 4 pole topology has been modified from 18 mm to 26 mm in order to achieve the same torque performances. On the other side, for the DW-design the same stack length value is used as the initial design.

TABLE 3.8 Best stator design obtained from the Pareto-front

	CW-SynRM stator	DW-SynRM stator
Number of turns / slots	12	3
Wire diameter [mm]	2.2	2.4
Conductor area [mm^2]	3.8	4.52
Phase resistance [Ω]	0.0176	0.0138
Stack length [mm]	26	18
Slot area [mm^2]	231.30	67.48
Filling factor	0.3942	0.4

In Fig. 3.36 the initial SynRMs designs (green dot line), the resized one (blue dot line) and the prototyped designs are shown. As it was mentioned above, the slot area was recalculated in order to respect the manufacturer requirements. Major improvements can be observed on 12 slots 4 pole design where the initial filling factor of 0.63 was reduced to 0.39. On the other side, for the 27 slots 4 pole structure, more or less the same improvements have been performed on the geometry side, and the number of turns was reduced from 4 turns/slot to 3 turns slot, in consequence the filling factor was reduced from 0.54 to 0.4 see figure 3.38 b and Table 3.9.

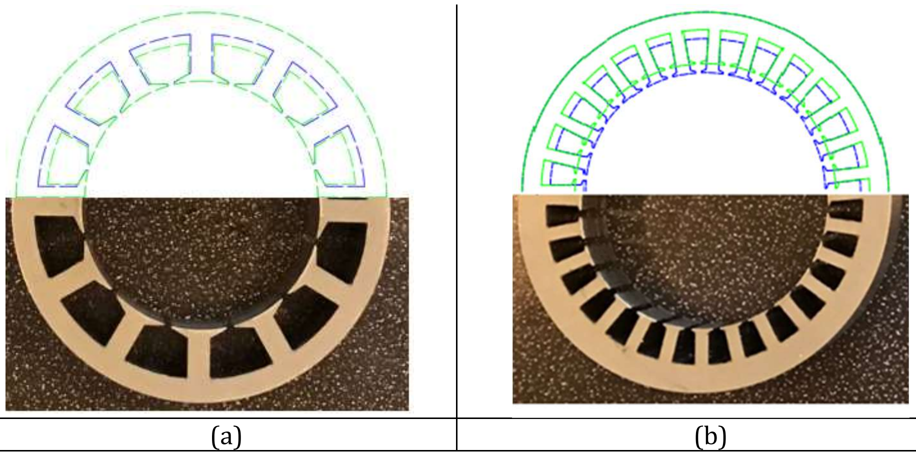

(a) (b)

Fig. 3.36 SynRM obtained before and after optimization CW-design (a) DW-design (b)

In what concerns the winding manufacturing method, as it was mentioned above this it will be done manually. The diameter of the chosen conductors is too big to handle it by hand. In consequence for both topologies a method that involves multiple equivalent wires in parallel for each turn/slot is performed, see TABLE 3.9 and Fig 3.37.

Table 3.9 Equivalent conductors for the chosen design

	CW-SynRM stator	DW-SynRM stator
Number of turns / slots	12	3
Wire diameter [mm]	2.2	2.4
Equivalent conductor [mm]	1	0.75
Nr. of parallel conductors/turn	5	10

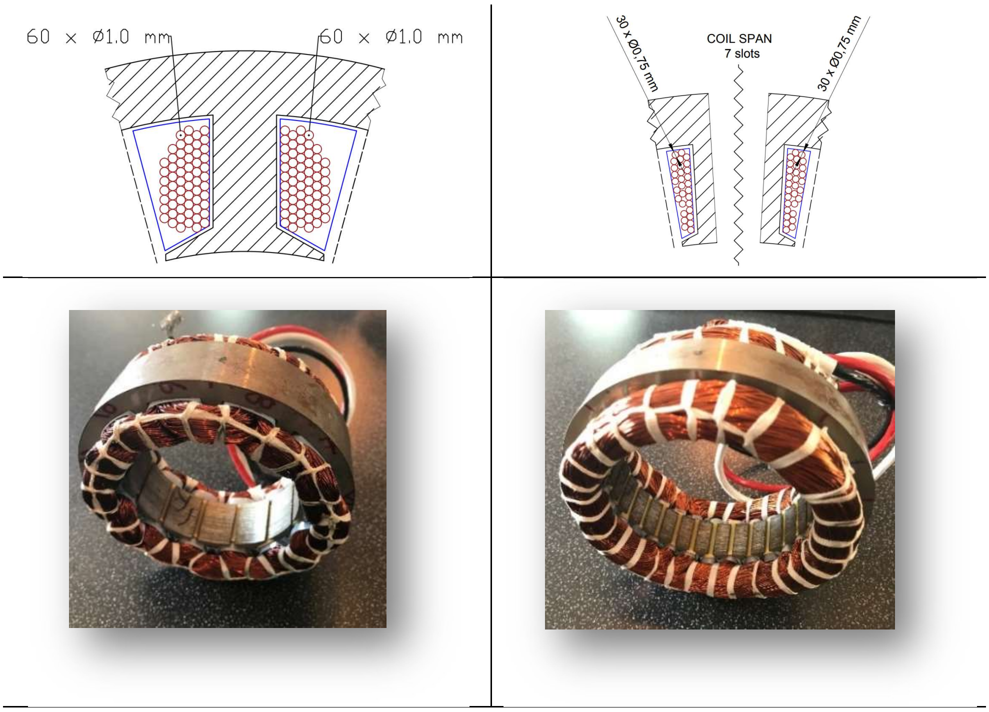

Fig. 3.37 Winding arrangement and the prototyped designs

3.7.2. Key performance indicators

In Fig. 3.38 the torque of the initial SynRMs design and that of resized ones are shown. At first, one can see in magenta line the FE-obtained electromagnetic torque for the PM-based design at rated load conditions. The average torque is 0.85 Nm, while its torque ripple is around 9 %. The torque of the CW-SynRM initial design and that of the resized one are shown in blue and black line, respectively. It can be noticed that if the RMS current is increased with 58 % and the axial length with 44 %, the same performances as the reference PMSM can be reached. The obtained average torque is 0.92 Nm for constant torque region and 0.85 Nm near the base point, while the torque ripple content is 38 %, with 8% larger than the initial design. On the other hand, the DW-SynRM, which results are given in green line for the initial design and red line for the resized one, meets the same performances with 50 % more current, while keeping the same magnetic core length as the PMSM. The average torque is 0.89 Nm for constant torque region and 0.86 Nm near the base point, while the torque ripple is 8 %, with 1% smaller than the reference machine.

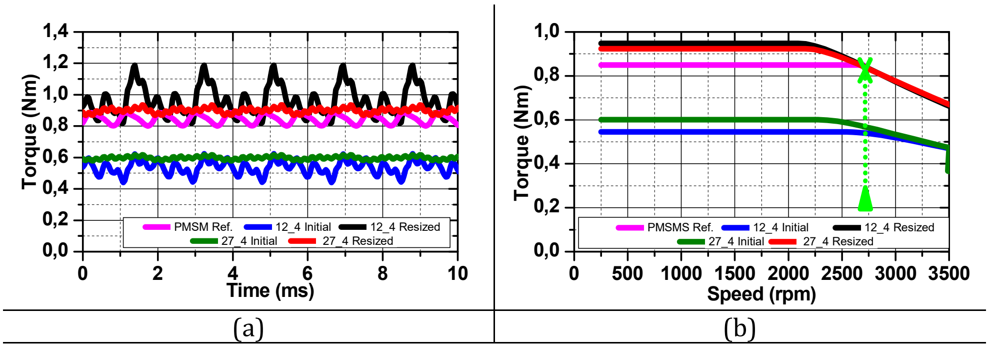

(a) (b)

Figure 3.38 Electromagnetic torque for initial and resized designs (a) and torque vs speed characteristic (b)

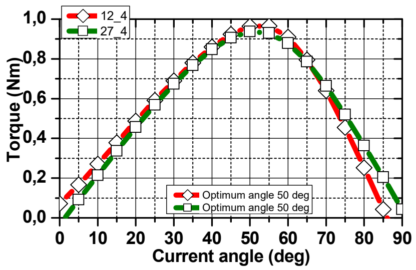

Optimum current angle comparison

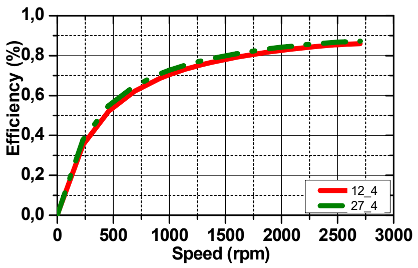

Efficiency comparison

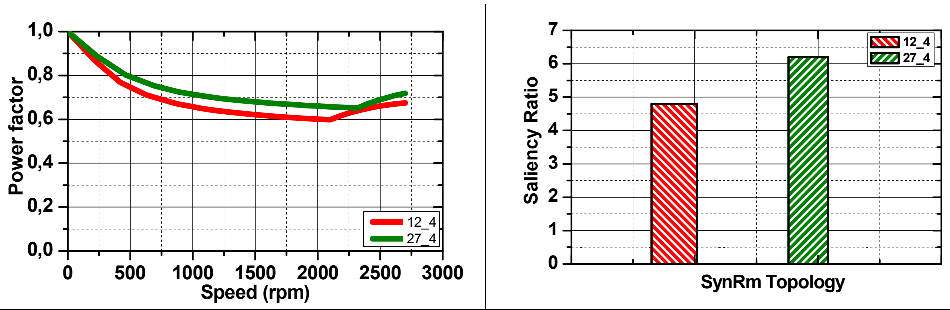

Power factor in function of speed

Saliency ratio comparison

Fig. 3.39 Key performance indicators for both SynRMs

Fig. 3.38 b shows the torque-speed characteristic for all motor topologies discussed in this section. The PMSM generates the highest torque for a constant torque region while for SynRMs it is quite challenging to reach the base point without over-sizing. This happens mainly because, unlike the PMSM, where the operating point can be easily reached by modifying the number of turns and/or the stack length, when it comes for SynRM case employing this degrees of freedom, the saliency can be undesirably alternated due to the non-linearity's of the magnetic circuit. Obviously under this circumstances, higher drive costs are expected as higher current cause higher VA-requirements of the inverter components. In fig. 3.39 power factor and saliency ration comparison are presented.

3.7.3 Comparison between 2D and 3D design

It is worth to mention, that using a 3D model the computation time is one of the biggest issues. One way to reduce the simulation time is to simulate just a part of the machines model. Thus, the 12 slots 4 poles topology has a symmetry of ¼, for this study it will be used only one eight of the machines so as to decrease the rather long computation time required for solving a 3D FEA model. On the other hand, the 27 slots adopted winding has no symmetry. In this case, the considered 3D partial model of the machine was performed by splitting the full model in half in the x-y plane (see Fig. 3.40 b).

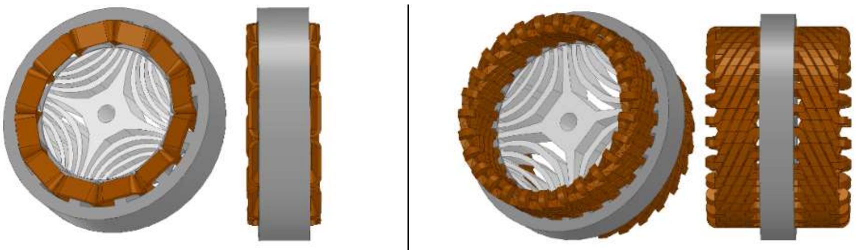

a) full model 12 slots 4 poles

b) full model 27 slots 4 poles

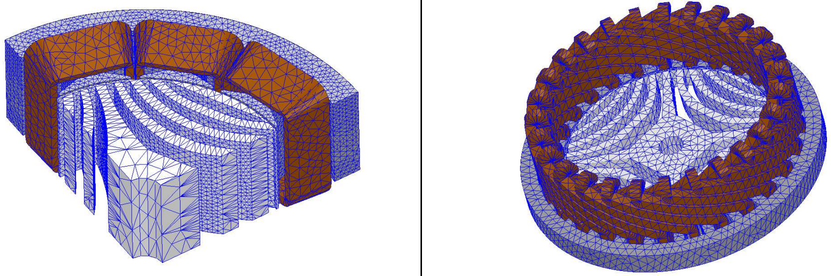

c) ¼, partial model 12 slots 4 poles

d) Half model 27 slots 4 poles

Figure 3.40 3D model of the prototype machines a) concentrated winding and b) distributed winding

In order to quantify the end winding effect, the L_d and L_q inductances as a function of stator current are compared in 2D and 3D FEA. The results are shown in Fig. 3.41, and supplementary, the differences between the obtained torque in 2D and 3D FEA for the same input current are plotted in Fig. 3.42.

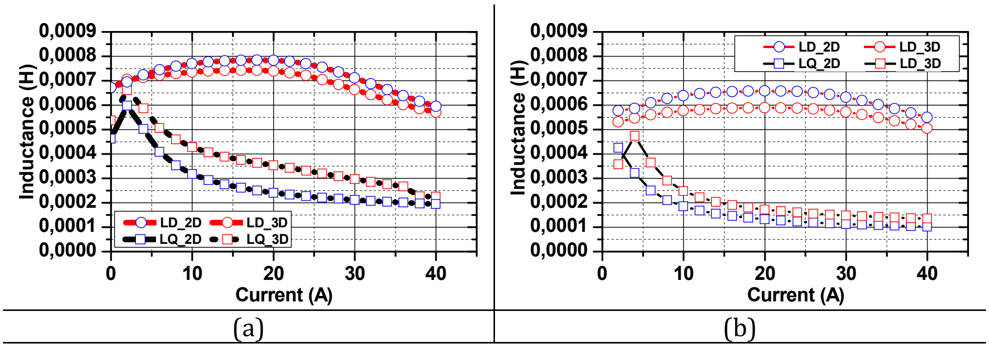

(a)

(b)

Figure 3.41 2D vs 3D FEA calculated d- q- axis inductances a) concentrated windings and b) distributed windings

The differences between the 2D and 3D computed electromagnetic torque can be seen in Fig. 3.44 and Table 3.11.

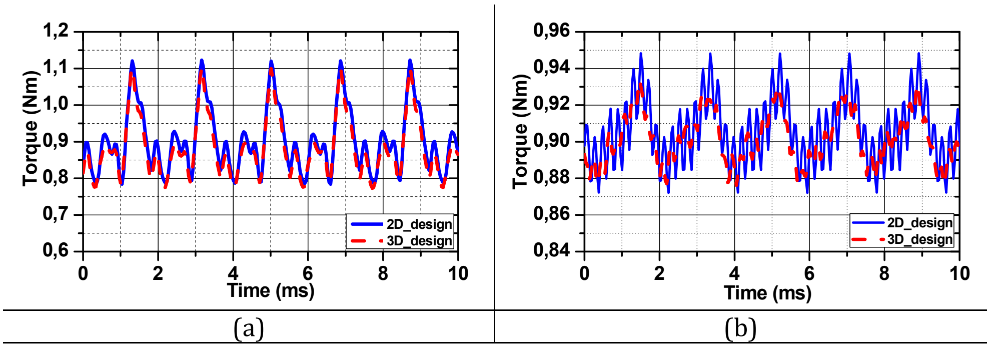

(a) (b)

Figure 3.42 2D vs 3D FEA Torque waveforms a) concentrated windings and b) distributed windings)

The 3D effect has also an impact on the iron losses of the analyzed machines. Figure 3.43 presents a comparative view of the iron losses between the two analyses. The 3D FEA predicts a 4.18 % for CW respectively 13,5 % for the DW, higher total iron losses (both eddy current and hysteresis losses) than the 2D one. As it can be seen in the figure, eddy current losses are not so sensitive as the hysteresis losses. This rise in iron losses can be attributed to the change in magnetic conditions associated to the leakage permeance components.

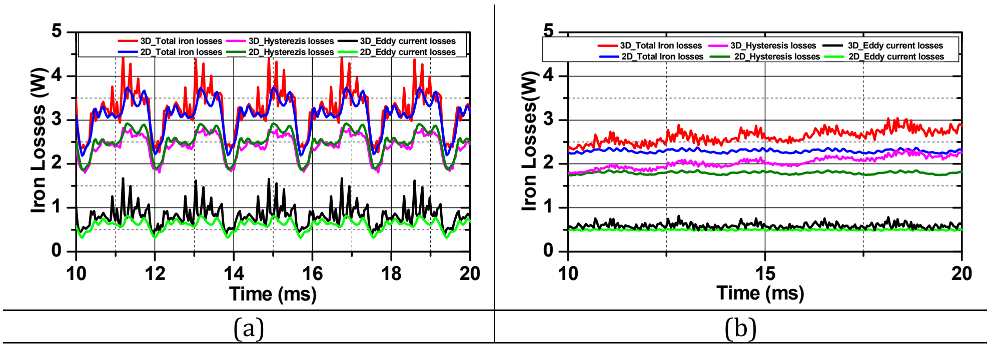

(a) (b)

Fig. 3.43 2D vs 3D FEA Iron losses waveforms a) concentrated windings and b) distributed windings)

In the analysis, the material M800-50A is used with the specific core loss data provided from the supplier. TABLE 3.10 presents the mean values of the iron losses.

TABLE 3.10 2D versus 3D FEA Iron losses

	2D_12_4	3D_12_4	2D_27_4	3D_27_4
Eddy current losses (W)	0.61	0.84	0.49	0.53
Hysteresis losses (W)	2.49	2.4	1.79	2.01
Total iron losses (W)	3.11	3.24	2.29	2.6

However, the 3D modelling shows a minimal impact on performance. 3D simulations are taking considerable computation time (3-4 hours) with respect to the 2D FEA computation where the simulation time is more or less up to 10 min (both simulated for an electrical period).

3.7.4. Active material cost and weight

The weight of the active materials is calculated from CAD models exported from 3D Maxwell software. Following the performance analysis, the material costs are based on market prices (as of calculation in October 2018), where a net cost of 6.5 €/kg, 4 €/kg and 1 €/kg is considered for magnet, copper and lamination material, respectively. No attempt has been made to estimate the manufacturing costs. The costs calculation was performed and reported in TABLE 3.11.

TABLE 3.11 Active material weights and their costs

	RF-PMSM	SynRM-CW	SynRM-DW
Steel [g]	528	1237	953
Copper [g]	164	340	440
Magnet [g]	147	-	-
Total mass [g]	839	1577	1393
Δ mass [%]	0	+ 87	+ 66
Total costs [€]	2.14	2.59	2,71
Δ costs [%]	0	+ 21	+ 26

From the market prices, due to the very small size and power of the compared motors, the PMSM is the lowest cost machine in terms of raw materials. However, due to the fact that the employed magnet in the PMSM is a very cheap one (e.g. ferrite grade 6, 0.6 Tesla), the SynRMs are not necessarily more attractive in terms of costs. Therefore, it can be argued that the CW-SynRM is a lower cost option with a simpler manufacturing process that the other PM-less candidate, DW-SynRM.

Total weight is another issue that SynRMs meet. Both designs are far away from the reference machine weight target, CW-SynRM with 87 % and DW-SynRM with 66 % more weight.

3.8 Conclusions

This chapter presented the sizing methodology and analytical design of the proposed SynRMs for cooling fan application. The stator/rotor geometry, machines electrical and magnetic parameters (e.g. inductances, resistances, winding configuration/specifications) as well as the output functions such as maximum torque, power factor and efficiency were identified. The FEA was proved to be useful and it was shown that this method is a fast and reliable procedure to identify the most important parameters of the SynRMs based on the design specifications.

The geometry of the SynRMs have been build up by using parametrized coordinates within Python scripts. This method allows changes in the machine structure, which represents an advantage mainly during optimization procedure.

As it can be seen from the results depicted in Table 3.8, it is clear that it is hard to match the PMSM torque performances. Obviously, this is a tough requirement due to the lack of the magnets and the lower power factor that this type machine exhibits. To reach the same operating point as the PMSM, a larger value of reactive energy is required (i.e. more current to magnetize the iron core or more voltage when employing the same current but a higher number of turns).

A comparison between best designs obtained, one with concentrated and other with distributed winding was performed. The comparison is done highlighting various key performances indicators both electromagnetic (e.g. torque density and quality) and electromechanical (e.g. torque/efficiency speed characteristics). Both topologies have been re-analyzed and re-optimized by taking into consideration the manufacturing limitations and torque performance requirements. Afterward, the promising designs were compared within the reference PMSM.

The 3D FEA computation enables to model the full geometry of the SynRM and to achieve more precise results (end coil effect is taken in consideration, self and mutual inductances) in comparison within 2D.

4. Structural and vibroacoustic analysis of SynRM

The audible noise produced by electrical machines can be classified in three main categories based on its source: aerodynamic (ventilation), mechanical (bearings) and electromagnetic (radial forces) [89]. Aerodynamic noise is characterized in a large band frequency between 500 to 1000 Hz [90]. On the other hand, mechanical noise can radiate single tones of frequencies larger than 3 kHz. Thus, the noise is transmitted from the source to the recipient (i.e. human being, sensor) through the electrical machine structure or through the air. Human ear has a high sensitivity for frequencies starting from 500 Hz, and up to 3.5 kHz; therefore, electromagnetic source is the dominating one in this frequency range, for low-to medium-power rated machines [91-93].

The vibroacoustic behavior of an electrical machine is the direct response of the excitation of its structure by the electromagnetic force developed under operation. Usually the concern is the stator core and its vibration is mainly induced by the electromagnetic force acting on its inner surface. The radial component of the force is approximately an order of magnitude higher than the tangential component in general therefore the contribution of the last one could be neglected. Modeling electrical machine magnetic noise requires modeling both the electromagnetic exciting force and the mechanical response of the excited structure. Once the vibrations of the structure are known, an acoustic model is necessary to compute the audible magnetic noise radiated by the machine.

Among the three types of magnetic forces occurring in electrical machines (Maxwell forces, Laplace forces, magnetostrictive forces), the only ones assumed to play an important role in acoustic noise radiation are airgap radial Maxwell forces which depend on the airgap radial flux density. Therefore, computing the airgap radial Maxwell forces asks for an accurate electromagnetic model of the machine. This model should be able to compute the airgap radial flux density, thus enabling the study of the influence of different machine design variables on the airgap radial Maxwell forces.

4.1 Rotor dynamic calculation

In this section a brief mechanical analysis of the built experimental models is presented. For both SynRMs the FE-based structural analysis is performed in ANSYS Workbench, in order to evaluate the mechanical stress at maximum speed and over speed (double maximum speed). These simulations are required to confirm the structural integrity of the rotors design for the given speed range. The rotor stress, deformation and safety factor are calculated in this section for each model. The mechanical properties of the material (M800-50A) is shown in TABLE 4.1 [107].

TABLE 4.1 Mechanical properties of M800-50A

	Data sheet value
Yield Strength (MPa)	300
Tensile Strength (MPa)	415
Young Modulus (GPa)	210
Mass Density ($kg \cdot m^3$)	7600

Analysis of mechanical loading of the rotor design is very important, mostly when small parts like tangential or radial ribs that link the rotor structure are part of it. The 4-pole rotor rated speed is Ω_b = 2700 rpm. At this speed, the centrifugal forces are acting on the rotor and causes stress throughout the rotor lamination stack, leading to deformation. In addition, the radial forces extracted from the electromagnetic simulations, are applied on the rotor structure as a radial pressure. If this stress is high enough, the material could yield. Both rotor designs have been imported from ANSYS Electromagnetics, step files, 3D structures. The von-Mises stress is calculated at 2700 rpm and 5400 rpm (twice the rated speed) in order to evaluate the stress distribution and deformation of the prototyped designs and to validate the mechanical integrity of both topologies.

To achieve precise results, the Sphere of influence [112] mesh sizing method is used. Basically, near a Sphere of Influence you can apply different mesh sizing in comparison to the mesh applied inside of the sphere. This method helps to reduce the number of elements for fast computation and accuracy results. For the study, due to the rotor structure design, the mesh is refined around the thinnest parts of the rotor (see Fig. 4.1).

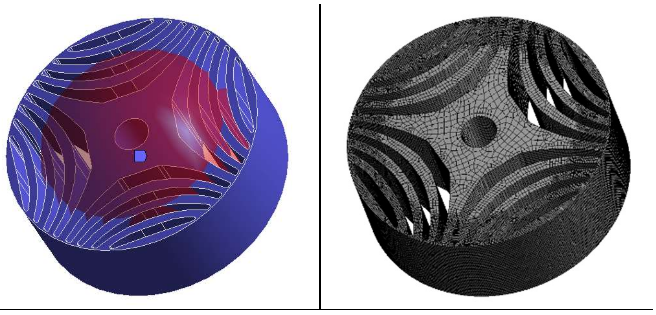

Fig. 4.1 Sphere of influence meshing method

A) Static Structural Analysis – at 2700 rpm (rated speed)

Figure 4.2 shows the results of the maximum von–Mises stress, which in both cases is below the used steels yield point (≤ 300 MPa), when considering a minimum thickness of the tangential bridges of 0,8 mm. In consequence no radial ribs and needed to support the rotor integrity. The maximum calculated von–Mises stress at the rating speed of 2700 rpm is 165 MPa for the CW rotor design and 195 MPa for the DW rotor design, which is located around the tangential ribs. Moreover, the maximum local deformation (see Fig. 4.3) due to the centripetal forces is -9μm (CW-rotor), which is approximately 2% of the airgap. Even so, the deformation is rather low and will have no effect on the mechanical or electromagnetic performances. The minimum deformation located to be around the shaft area as would be expected.

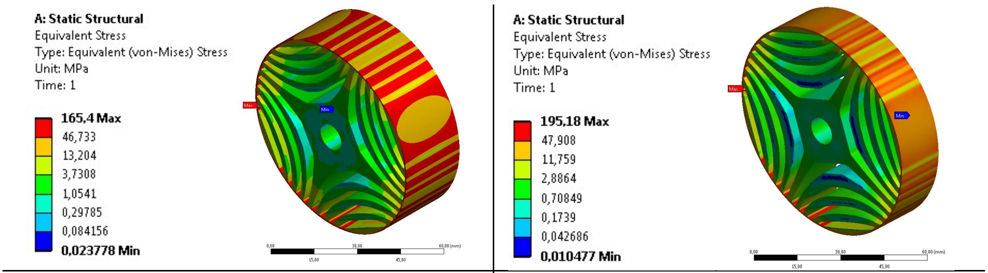

von- Mises stress for 12 slots 4 pole rotor design

von- Mises stress for 27 slots 4 pole rotor design

Fig. 4.2 von- Mises stress at 2700 rpm

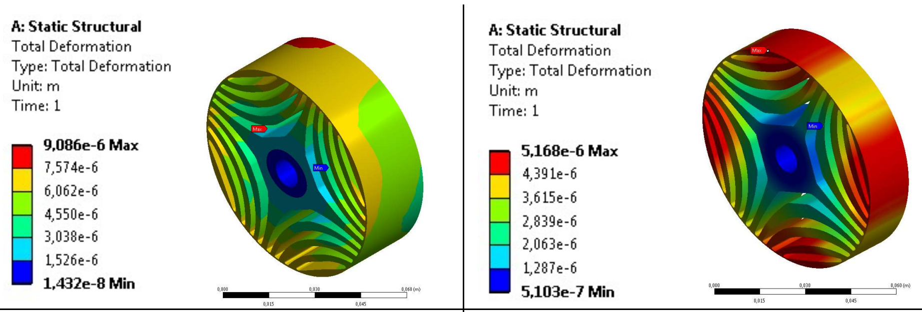

Total deformation for 12 slots 4 pole rotor design

Total deformation for 27 slots 4 pole rotor design

Fig.4.3 Total deformation at 2700 rpm

B) Static Structural Analysis – at 5400 rpm (twice the rated speed)

The stress distribution for 5400 rpm is shown in Fig. 4.4. The resulted von-Mises stress achieves 232 MPa for the CW rotor structure and 255 MPa for the DW rotor structure. As the tensile strength of the lamination material is 300 Mpa, the stress distribution in the rotor structures for this speed is still under the maximum value. On the other hand, at this speed the local deformation is higher, see Fig. 4.5. The maximum calculated deformation at 5400 rpm is 19.7 μm (for CW-rotor), which represents 3.8 % from the airgap width. This deformation is mainly due to the lack of the radial ribs.

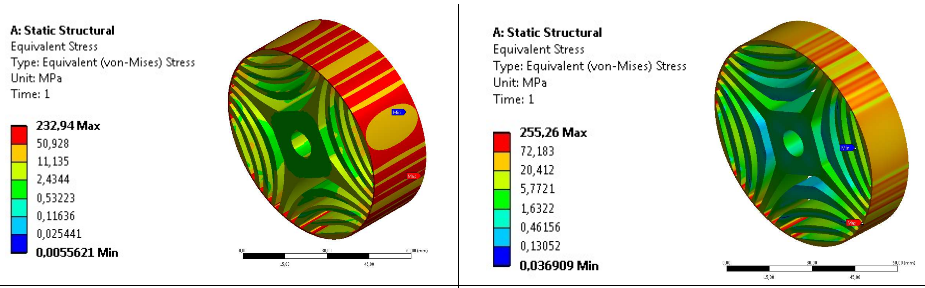

von- Mises stress for 12 slots 4 pole rotor design

von- Mises stress for 27 slots 4 pole rotor design

Fig. 4.4 von- Mises stress at 5400rpm

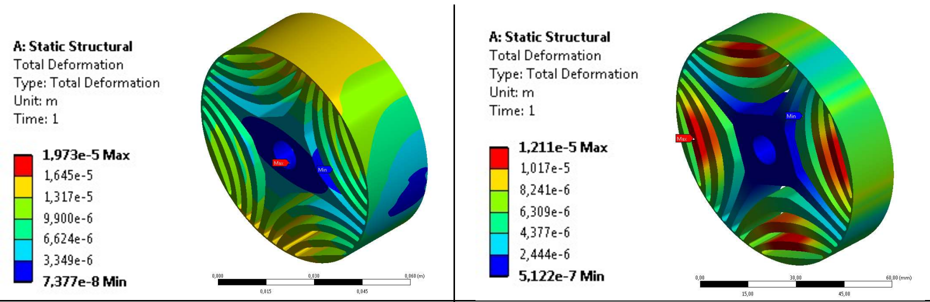

Total deformation for 12 slots 4 pole rotor design

Total deformation for 27 slots 4 pole rotor design

Fig. 4.5 Total deformation at 5400 rpm

4.3 Stator analysis - NVH behavior

Electric motors manufactures are highly focused on low noise and vibration emissions in automotive applications [108]. Accurate analysis of natural frequencies is thus one of the key issues to design an electrical machine with a low noise and vibration content [109-110]. Two important parameters for NVH behavior are the natural frequencies and mode shapes. FE models were used to analyze the influence of the material on the natural frequency. The FE analysis results are consistent with modal tests results, see TABLE 42. Once the radial magnetic forces are given along with their frequencies and space-harmonic, the natural frequencies and vibrational modes of the stator structure can be computed. Any frequency of the radial magnetic force that is close to one of the natural stator frequencies for the same force spatial distribution as vibrational modes, can produce vibration and high tonal nodes. The accuracy of the modal analysis of the stator core allows us to obtain the vibration amplitude and mode shapes of the structure at a corresponding frequency. The analyzed stator structures and the designed parameters are shown in Table 4.3 and Fig. 4.6.

TABLE 4.2. Modal validation Numerical Vs Experimental

	12 Slots FEM	12 Slots Experimental	27 Slots FEM	27 Slots Experimental
MODE 2	1095 Hz	1102 Hz	1531	1517
Mode 3	2876 Hz	2919 Hz	4120	4050
Mode 4	5083 Hz	5310 Hz	-	-

TABLE 4.3 The design data of the stator core

Parameter	12 Slots	27 Slots
Outer Diameter D_{out} [mm]	119	119
Inner diameter D_{in}[mm]	74.8	84.8
Yoke thickness [mm]	6.92	8.68
Slot opening [mm]	2	2.1
Tooth width [mm]	7	4.2

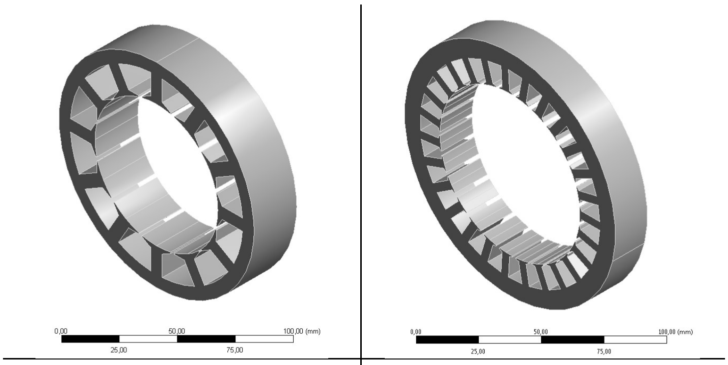

12 slots design	27 slots design

Fig. 4.6 The FEM model of the stator core

4.3.1 Numerical Results

In order to perform NVH analysis, normal modes of the stator structures must be identified. Modal analysis was performed in Ansys Workbench software. The 2nd, 3rd and 4th, 5th and 6th mode shapes, together with their frequencies for the 12/4 design are given in Fig. 4.7 a, b, c, d and e respectively and for the 27/4 variant in Fig. 4.7 f, g and h, respectively. The resulted deformation amplitudes in the figures below are exaggerated in order to highlight the mode shapes.

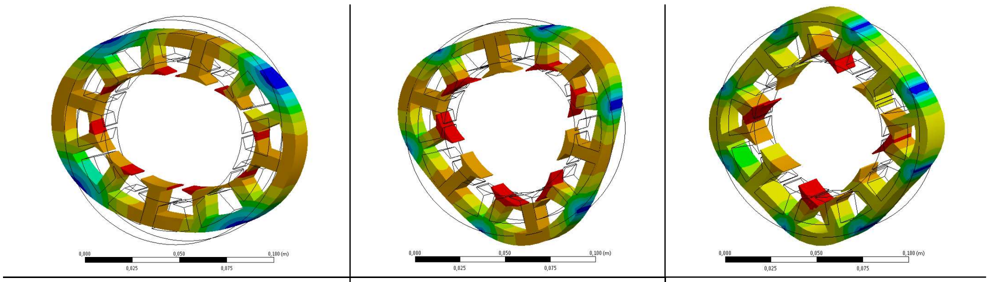

a) Mode 2 – 1095 Hz
b) Mode 3 – 2876 Hz
c) Mode 4 – 5083 Hz

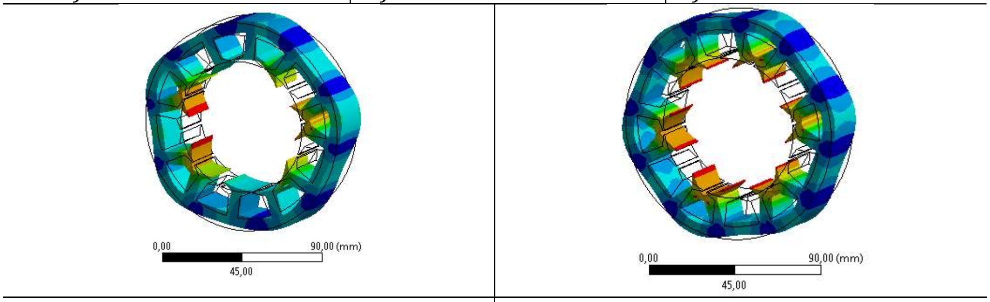

d) Mode 5 – 7118 Hz
e) Mode 6 – 8036 Hz

12/4 stator structure

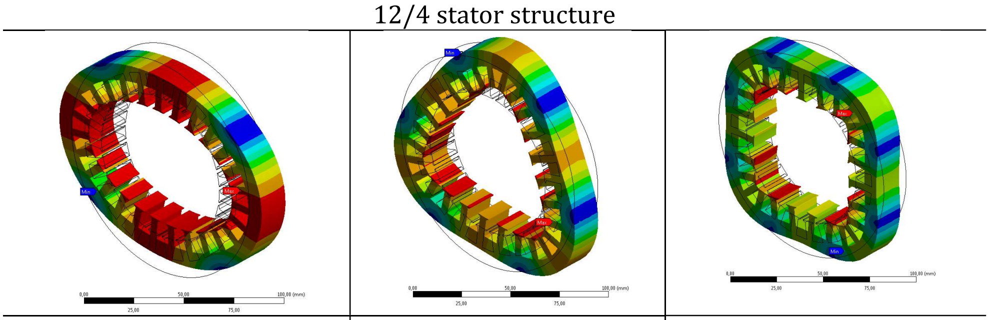

f) Mode 2 – 1531 Hz
g) Mode 3 – 4120Hz
h) Mode 4 – 7416 Hz

27/4 stator structure

Fig. 4.7 Mode shapes of the investigated machines

4.3.2 Experimental results

For the experimental modal analysis, two methods can be used: impulse force hammer or the shaker method. In this study, the hammer method was used since it allowed sufficient accuracy for the test under consideration. The purpose of this study is to validate the numerical values with the experimental results.

In Fig.4.8 it can be seen how the motor structure was prepared for the modal test. In both situations the same fixation frame and the same flexible ropes were used, in order to reproduce free-free testing conditions which are useful to characterize intrinsic modal properties of the machine. In both setups, the vibration acceleration is measured for a number of points on the structure (see Fig. 4.10 a), with the hammer input force.

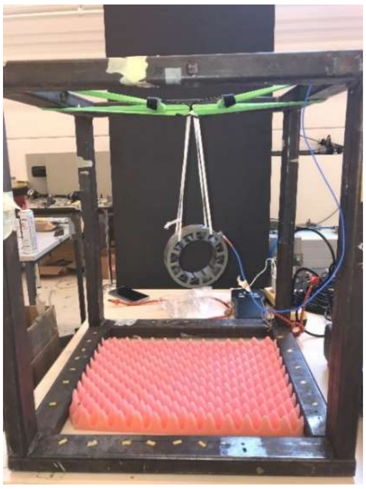

4.8 Structure fixation

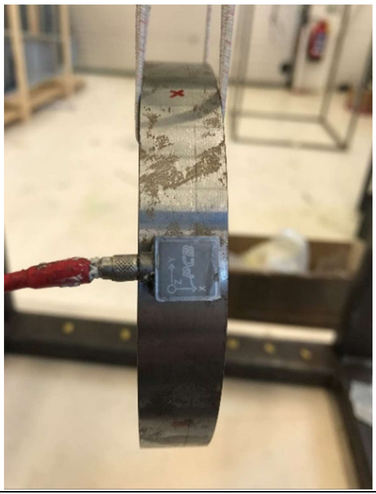

4.9 3-dimensional sensor

A 3-dimensional sensor (see Fig. 4.9), attached to the stator outer diameter permits to measure the vibration acceleration. Then the modal characteristics (modes, natural frequencies, damping, transfer function, etc.) can be extracted using parameter estimation algorithms that curve-fit the measured data to a parametric mathematical model PolyMAX, which is implemented in the commercial software Simcenter TestLab.

Two sets of measurements have been performed: with and without coils (see Fig. 4.10 a and b).

a

b

c

d

Fig. 4.10 Bookmarks for simulation

First, for the 12 slots structure, as it can be seen from Fig. 4.11 a and b, modes and frequencies of the stator core for both sets of measurements (with and without windings) are obtained. Eight Frequency Response Function (FRF) resulted from the measurements (Run1…Run8) are shown. Furthermore, the sum of the (FRF) for both tests can be observed in Fig. 4.11 c, which corresponds to the numerical results. In this situation, 3 FRF peaks corresponding to the 2nd (ovalization), 3rd (triangular) and 4th (square) mode shape are more visible when the stator core has no windings. On the other hand, due to the damping effect of the coils, the resulted FRF are flattened and less pronounced. The same sets of tests have been performed for the 27 slots structure. According to Fig. 4.12 c, we have 2 FRF peaks corresponding for the 2nd (ovalization) and 3rd (triangular) mode shape.

The damping effect is even more visible here due to the high volume of copper and the end windings effect.

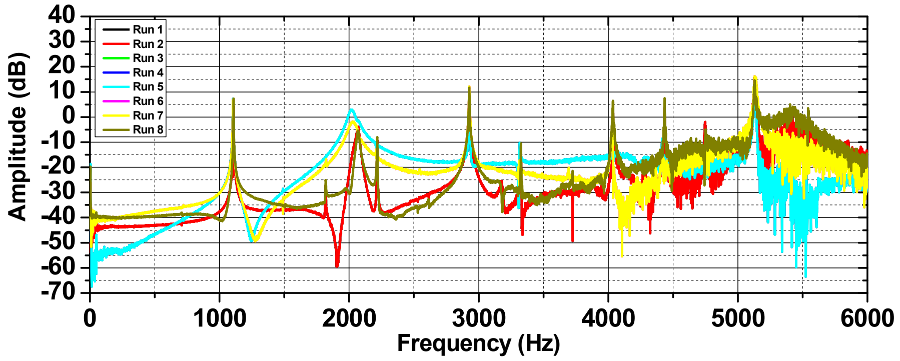

a) FRFs measurements without coils

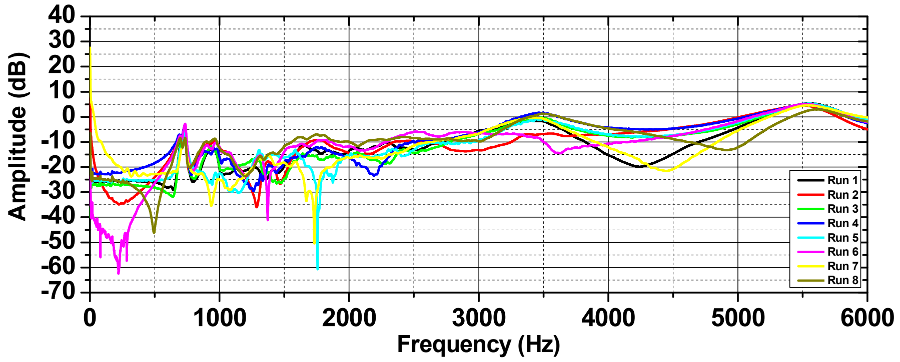

b) FRFs measurements with coils

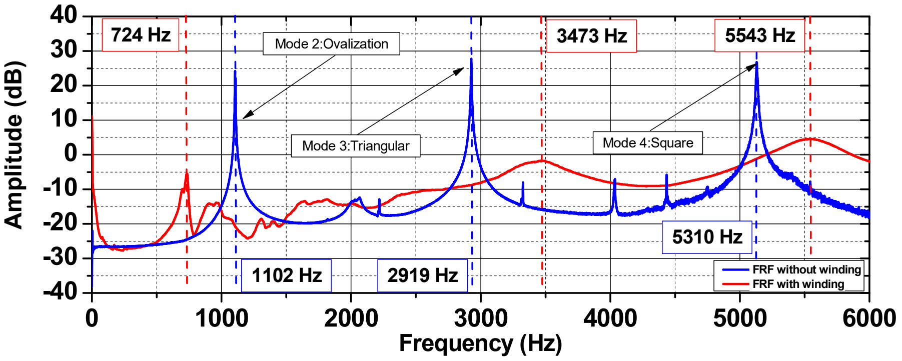

c) Sum of the FRF measurements for both measurements

Fig. 4.11 FRF and sum of FRF resulted from measurements for 12 slots structure

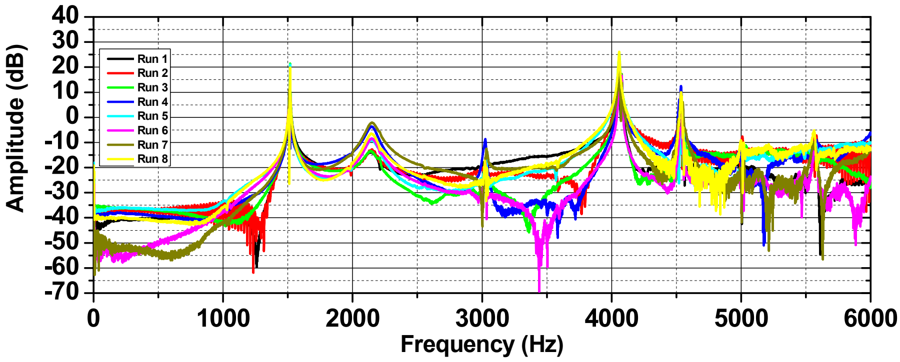

a) FRFs measurements for without coils

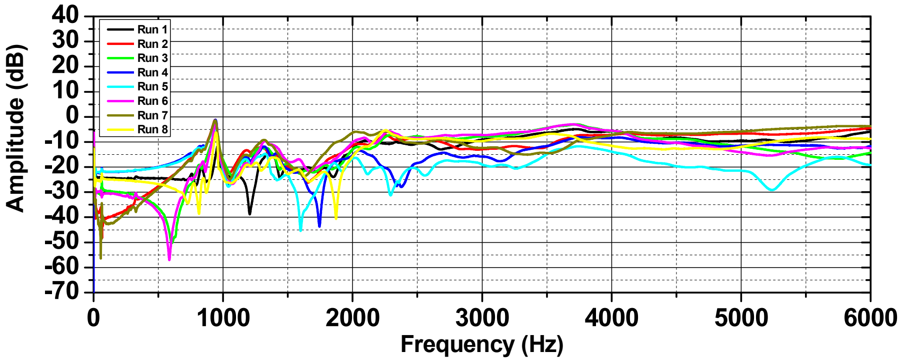

b) FRFs measurements for with coils

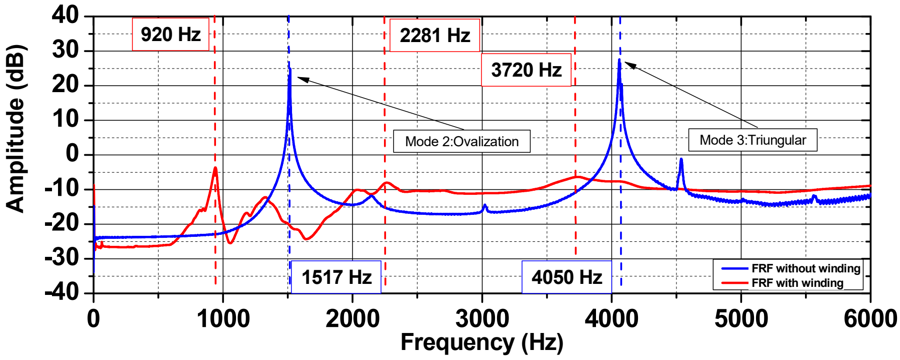

c) Sum of the FRF measurements for both measurements

Fig. 4.12 FRF and sum of FRF resulted from measurements for 27 slots structure

In this situation we have 2 FRF (no winding test) peaks for 27 slots design, which corresponds to the same frequency as the numerical results.

4.5 Conclusions

Rotor dynamic analysis shows that the designed rotor is mechanically feasible for twice the rotor maximum operating speed and the mechanical integrity in terms of stress distribution and total deformation are above the maximum operating speed.

The modal analysis of the stator is of great importance. This analysis allows us to obtain the natural frequencies and the mode shapes. Numerical and experimental results have been analysed and compared.

5. Experimental validation

This chapter presents the experimental testing of the constructed SynRMs. Electromagnetic and vibroacoustic measurements of the machines are performed. Additionally, the reference PMSM machine is tested under the same scenarios. It is mandatory to perform this test in order to validate the functionality of the developed products.

In case of the research performed in frame of this thesis the aim of the laboratory measurements was to validate the design and the FEA simulations results obtained previously.

5.1 Prototype – Fabrication and Assembly

A functional experimental model acts as a "proof of concept" [57], allowing experimental validation of the motor electromagnetic and mechanical design through various dynamic and static tests. The prototype manufacturing was performed by ICPE Bucharest SA. Before the manufacturing, all motor parts have been designed in a 3D CAD model. Fig. 5.1 shows a 3D CAD model of the CW-SynRM. Furthermore, a short description regarding the main parts of all three electrical machines are shown in Fig. 5.2.

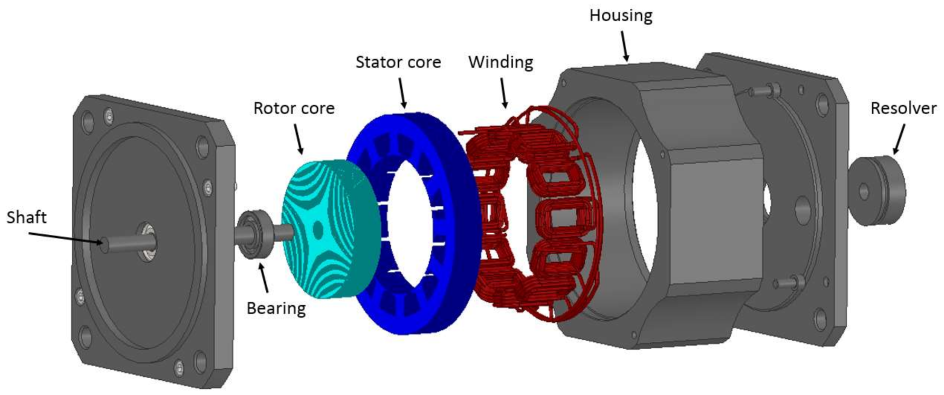

Fig. 5.1 3D CAD model of CW-SynRM

The first stage in the fabrication of the prototype is building the stator and rotor core lamination stacks. Here, the laser cut technology has been used. Before cutting, all the lamination profile has been glued together using a special epoxy in order to hold them together.

Stator DW-SynRM | Stator CW-SynRM | Reference PMSM

Winding + stator DW-SynRM | Winding + stator CW-SynRM | Winding + stator PMSM

Rotor DW-SynRM | Rotor CW-SynRM | Rotor PMSM

Prototype DW-SynRM | Prototype CW-SynRM | Prototype PMSM

Fig. 5.2 Manufactured parts for all studied electrical machines

All 3 experimental models have the same housing. It is a very important to have the same housing when the vibroacoustic measurements will be performed.

Further, as it can be seen in Fig. 5.3, and according to Fig. 5.1 all three electrical machines have a two-pole resolver attached on the end side of the shaft, outside of the housing. Here, the resolver is an excellent component for the positon feedback of the rotor speed. Furthermore, it provides an important signal for the control system through a RS232 port connection.

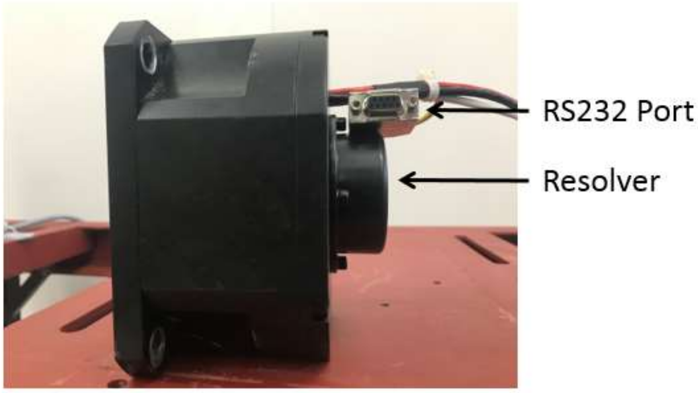

Fig. 5.3 Resolver mounted on the end side of the shaft

5.2 Test bench layout

Test bench specifications are given below:

1. Types of machine that can be tested: 3-phase SynRM and PMSM;
2. Voltage range: 0-13 VDC;
3. Load characteristics: max torque 0.85 Nm, rated speed 2700rpm;
4. Mechanical load description: Reference machine original FAN
5. Acquisition and processing: current, torque, speed, noise, vibration;
6. Control equipment: dSpace MicroLabBox

Fig. 5.4 shows the test bench, which was especially designed and build up in the laboratory of Technical University of Cluj-Napoca for this experimental work. This test bench consists of the following:

(a) test bench structure
(b) the electrical Machine Under Test (MUT)
(c) fixation frame of the MUT
(d) mechanical load (Cooling Fan)
(e) AC/DC variable power supply
(f) 3 phase power converter
(g) dSpace Micro LabBox
(h) Control Desk

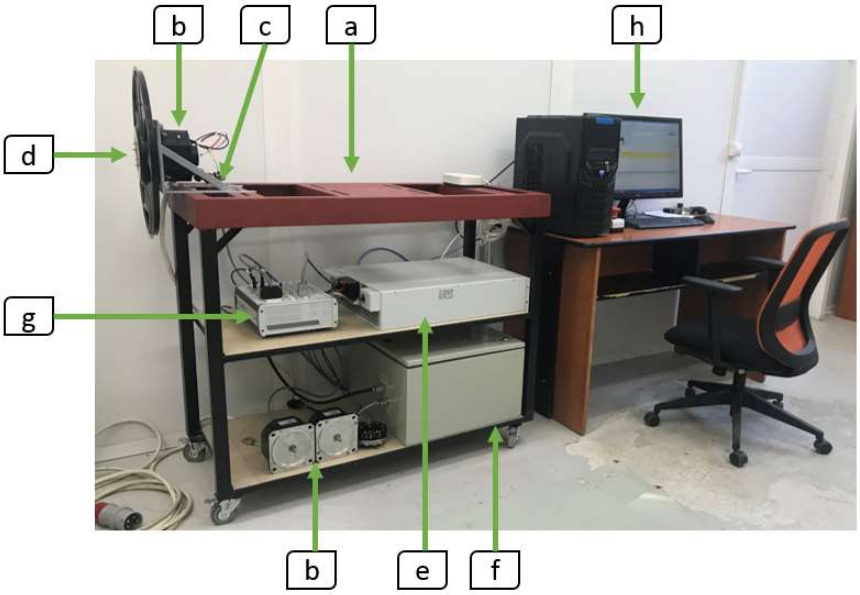

Fig. 5.4 Test bench structure

Its block scheme is given in Fig. 5.5.

The implementation of the testing procedure is done using dSpace MicrolabBox, an all-in-one development system, compact and powerful real-time digital prototyping tool [116]. The combination of dual core processor gives a high computation power and the integrated FPGA chip provides high speed and low latency needed for closed loop control applications. More than 100 I/O channels for various interface types can be found on this operating platform, including 48 bidirectional channels, 32 with high resolution analog input and 16 high-resolution analog output channels. Furthermore, two separate resolver interfaces are available and additionally, several I/O channels are dedicated for electrical machines control purposes like, position sensors, synchronous multichannel or block commutation PWMs. However, in this case, due to the high-performance prototyping platform, the measurements have been performed by using a switching frequency of 10 kHz.

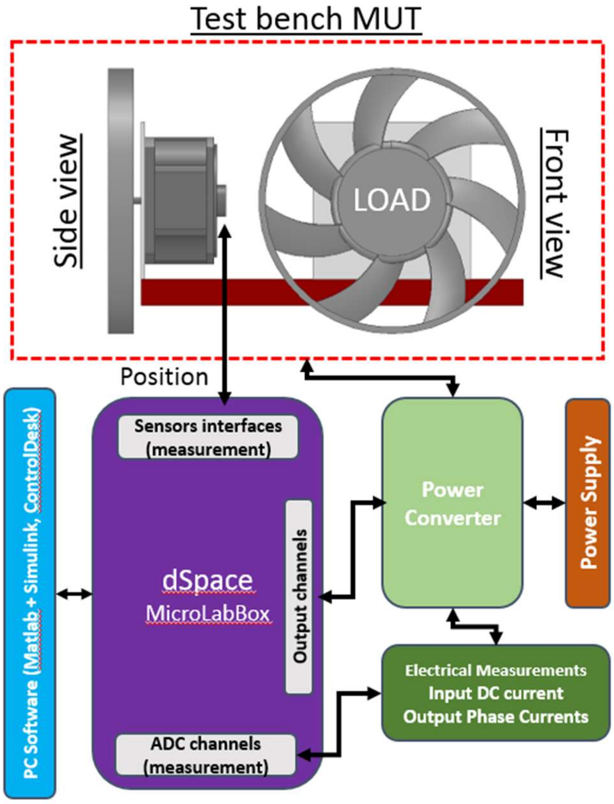

Fig. 5.5 Test bench schematic

The Graphical User Interface (GUI) is done through Control Desk software. Due to this software it is possible to do data acquisition and to visualize or to modify variables in real-time.

Finally, some experimental results with regards to the key performance and vibroacoustic of the studied machines will be given.

5.3 Results of the measurements

5.3.1 Key performance measurements

The results obtained by testing the designed SynRMs and the reference PMSM are performed under rated operating conditions. Therefore, the original fan is used as load. The load torque produced by the fan is proportional to the square of the rotation speed. This type of load exhibits low torque at low speeds than at high speeds, which implies that the load torque is relatively small when starting up. The steady-state torque versus speed characteristic of the analyzed fan is represented in Fig. 6.6. This characteristic can be calculated as follows:

$$k_f = n/\left(\sqrt{T}\right) \tag{5.1}$$

where, k_f is the fan constant, n the speed in rpm and T nominal torque value in Nm.

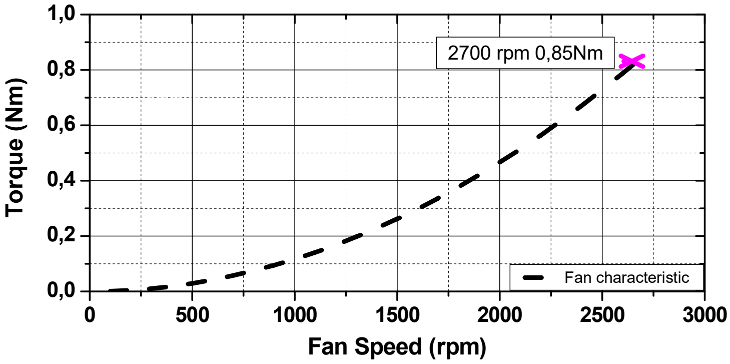

Fig. 5.6 Torque-speed characteristic of the used load Fan

The results under rated operating conditions are given in Fig. 5.7. It can be noticed, from the torque-speed characteristic, that both SynRMs don't reach the rated operating point. A difference of -14 % less torque for the DW-SynRM and -28 % respectively for the CW-SynRM is reported in respect to the operating point. On the other hand, the reference PMSM meets the rated conditions and reaches the operating point of 2700 rpm at 0.85 Nm.

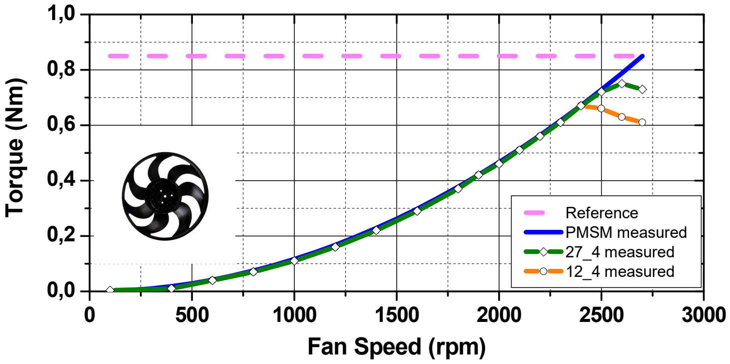

Fig. 5.7 Torque vs. speed characteristic (with Fan load)

In order to go further with the machine behavior another sets of tests were performed. To achieve the CPSR behavior, a different load than the existing cooling fan-type load is needed. For this study, a DC motor is used as load machine. Another additional component for this set of tests is the Torque sensor. For the previous measurements the torque value was estimated in function of the fan speed according to equation 5.1. Furthermore, for this sets of measurements, the original test bench was modified according to Fig. 5.8.

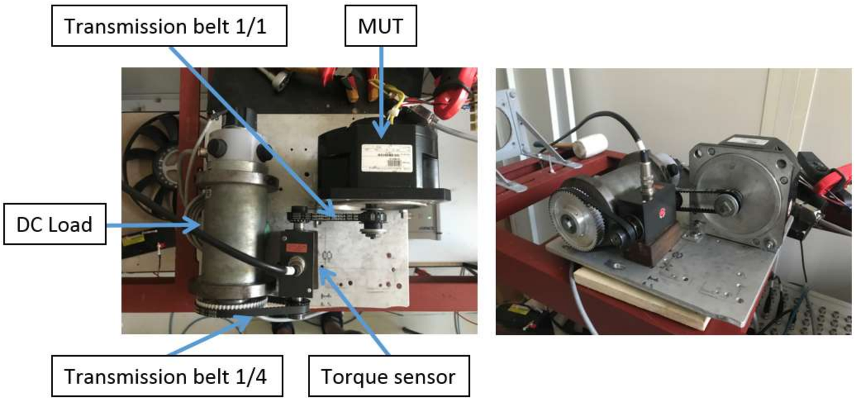

Fig. 5.8 Test bench with DC-load for CPSR study

The second laboratory tests were performed to study key performances of the SynRMs for different operating points as follow:

1. The 1st set is performed at maximum speed achieved for a 0,85 Nm reference load torque;
2. The 2nd set is performed for the rated operating point;

For both SynRMs the measured I_d/I_q currents, phase voltage and mechanical torque were taken into account. A direct comparison between the predicted FEA results against the measured ones is presented.

A) First sets of measurements – maximum speed for 0.85 Nm reference load torque

As it can be seen in Fig. 5.9, the maximum CPSR is around the of 2000 rpm. A comparison between FEA and measured results are presented.

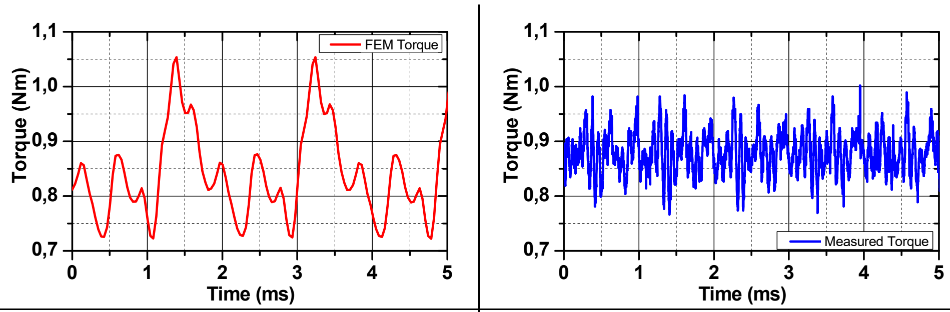

a) FEM electromagnetic torque | b) Measured mechanical torque

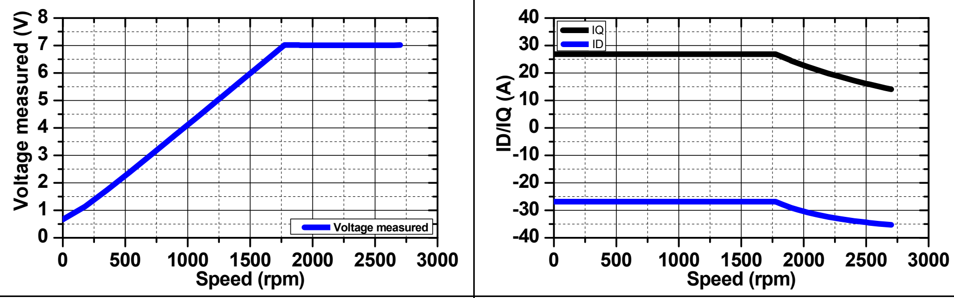

c) Measured Phase Voltage | d)Measured Id/Iq currents

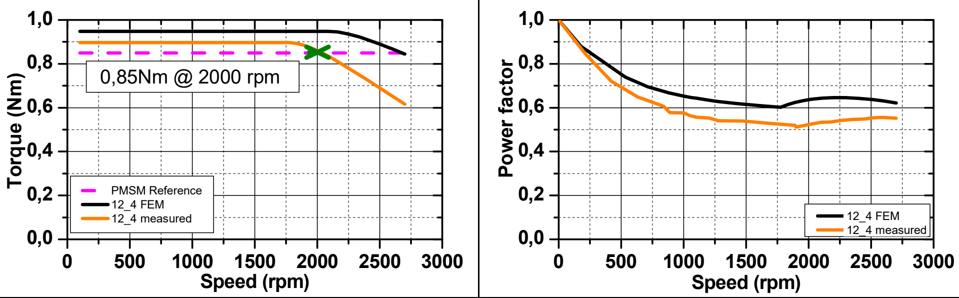

e) Torque vs. speed, FEA vs measured comparison | f) Power factor vs speed, FEA vs measured comparison

Fig. 5.9 FEA and experimental measurements of CW-SynRM performed at 2000 rpm

Moreover, according to Fig. 5.9 a and b, it is obvious that in terms of torque ripple the measurement results are lower than the FEA result. The mean error between the measured and FEA torque ripple waveforms is 56 %. One possible explanation to this may be the equipment accuracy as the rated torque of the transducer is 20 Nm and the sensitivity and accuracy may affect the results at low levels under its rated torque. The device technical specifications indicate a ± 0.1 % error at rated torque (20Nm ± 0.02Nm). Hereafter, the same results are plotted in Fig. 5.10 for the second topology taken into study, the DW-SynRM. The maximum CPSR is around the of 2200 rpm.

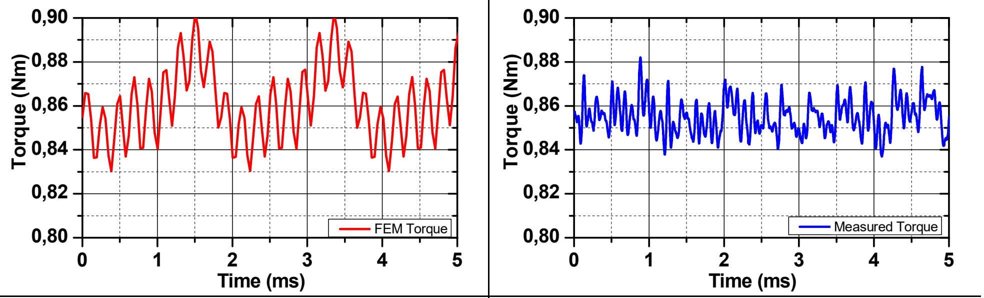

a) FEA electromagnetic torque | b) Measured mechanical torque

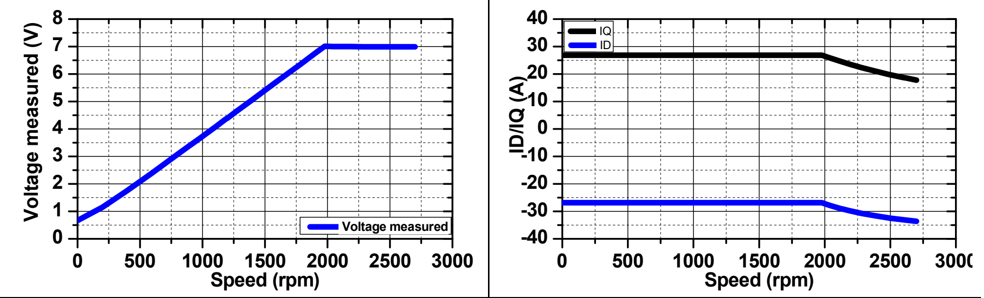

c) Measured Phase Voltage | d)Measured Id/Iq currents

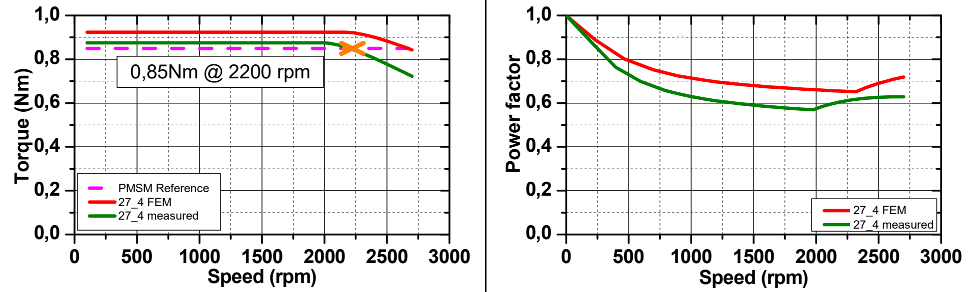

e) Torque vs. speed, FEM vs measured comparison | f) Power factor vs speed, FEM vs measured comparison

Fig. 5.10 FEA and experimental measurements of DW-SynRM performed at 2200 rpm

A) Second sets of measurements – nominal operating point

The tests have been performed in order to obtain the maximum torque given by the SynRMs under the rated speed condition (2700 rpm). In Fig. 5.11 The key performances comparison between FEA results and measured ones is presented. According to the results, it is obvious that both SynRMs don't reach the operating point. A torque difference of 28 % for the CW topology and 15 % for the DW one results in respect to the operating point.

SynRM 12 slots 4 pole | SynRM 27 slots 4 pole

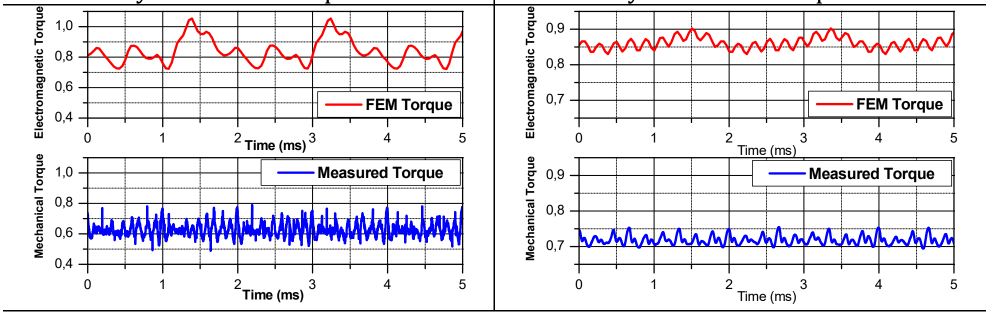

Torque, FEA vs measured at 2700rpm

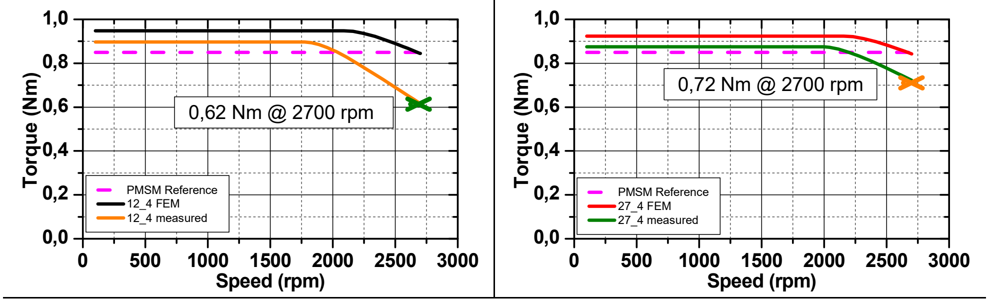

Torque vs. speed, FE vs measured comparison at 2700 rpm

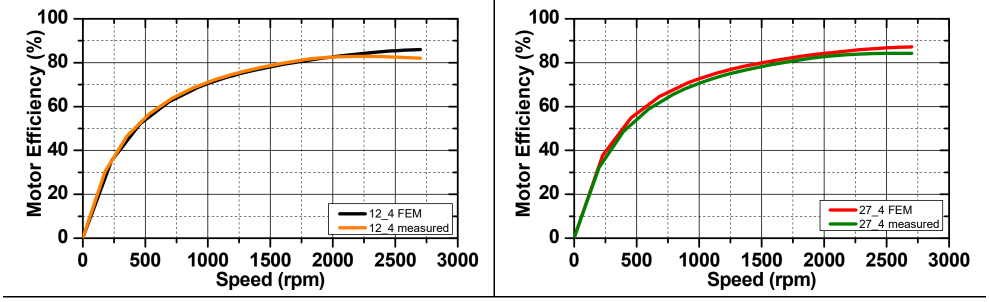

Efficiency vs speed, FEA vs measured comparison at 2700 rpm

Fig. 5.11 Key performances comparison between FEA and measured

A short description regarding the machine's performances are given in Table 5.1 and 5.2.

Table 5.1 CW-SynRM performances resume

Speed_Spec	Torque_Spec	Torque_calc	ΔT	P_spec	P_calc
[RPM]	[Nm]	[Nm]	[%]	[W]	[W]
900	0,85	0,90	5,5%	79	84
1000	0,85	0,90	5,5%	89	94
1100	0,85	0,90	5,5%	98	103
1200	0,85	0,90	5,5%	107	113
1270	0,85	0,90	5,5%	113	119
1900	0,85	0,88	3,9%	169	176
2000	0,85	0,86	1,2%	178	180
2500	0,85	0,69	-18,8%	223	181
2600	0,85	0,65	-23,2%	231,4	177,79
2700	0,85	0,62	-27,5%	240,3	174,21

Table 5.2 DW-SynRM performances resume

Speed_Spec	Torque_Spec	Torque_calc	ΔT	P_spec	P_calc
[RPM]	[Nm]	[Nm]	[%]	[W]	[W]
1000	0,85	0,88	2,9%	79	82
1000	0,85	0,88	2,9%	89	92
1100	0,85	0,88	2,9%	98	101
1200	0,85	0,88	2,9%	107	110
1270	0,85	0,88	2,9%	113	116
1900	0,85	0,88	2,9%	169	174
2000	0,85	0,87	2,9%	178	183
2500	0,85	0,78	-8,5%	223	204
2600	0,85	0,75	-11,7%	231,4	204,24
2700	0,85	0,72	-15,0%	240,3	204,27

5.3.2 Vibroacoustic measurements

For the vibroacoustic measurements, the same test procedure was applied for all three electrical machines discussed in this thesis, the PMSM reference machine and the built CW-SynRM and DW-SynRM experimental models. The tests were run in no-load and load state of the machines. Both tests were used to investigate the influence of switching frequency on noise and vibration level of the machines. The procedure has three steps:

1. The machine speeds up until a given reference speed in 25 seconds.
2. Once the reference speed is reached, the speed is kept at a constant value for another 10 seconds.
3. The machine decelerates until 0 rpm. Deceleration time depends on the machine type. For PMSM the deceleration time is larger than for SynRM due to the cogging torque. The profile of the speed is given in Fig. 5.13.

The vibration acquisition was done by three one-direction PCB piezotronics accelerometers, mounted on the machine housing. Furthermore, one microphone was placed in the immediate proximity of the MUT and another one at a certain distance from it (1 meter). For data acquisition a *SCADAS Mobile* unit was used to record the measured data. The *Test.Lab* software was used for computing and post-processing the signal delivered by the accelerometers and microphones. A short description about test components for N&V analysis are presented in Fig. 5.12.

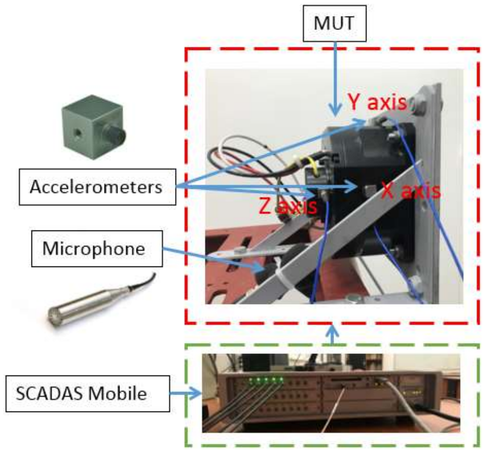

Fig. 5.12 N&V test equipment

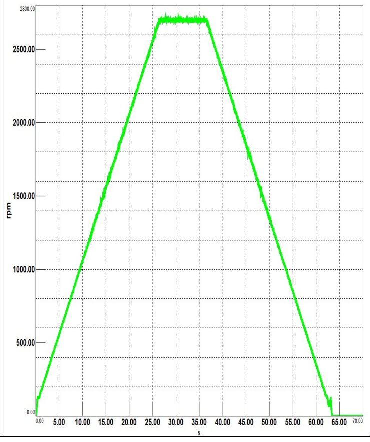

Fig. 5.13 Speed Test -Profile

For no-load condition, in Fig. 5.14 the waterfall diagram of the vibration signal for all three tested electrical machines is presented. A vibration at 10 kHz is visible, which is due to the inverter switching frequency. This vibration has a second harmonic, at 20 kHz visible on the same waterfall diagram. This is caused by the PMW signal whose harmonics contribute to the vibration and noise signal.

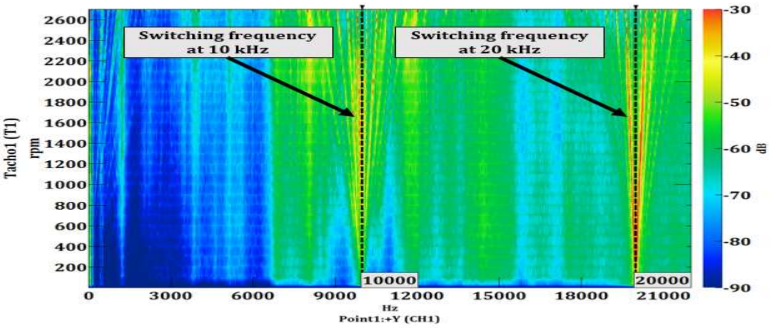

PMSM 12 slots_8 pole

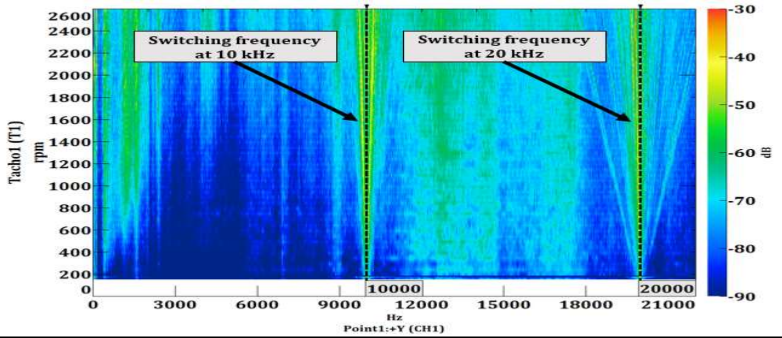

SynRM 12 slots_4 pole

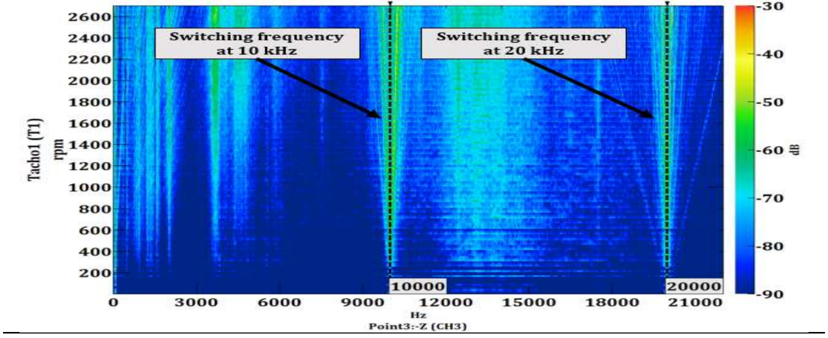

SynRM 27 slots_4 pole

Fig. 5.14 Vibration spectrum for 10 kHz switching frequency for no-load condition

Further, in Fig. 5.15 the oblique lines show the motors harmonics frequencies order. In case of the PMSM the first order is 8, related to the rotor poles number and for both SynRM due to the rotor design with 4 poles, the first order is 4.

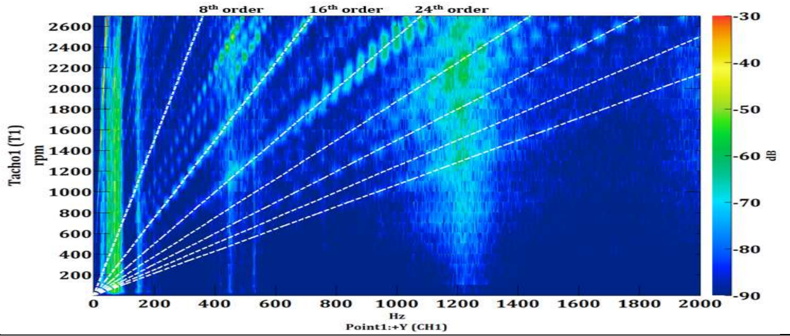

PMSM 12 slots_8 pole

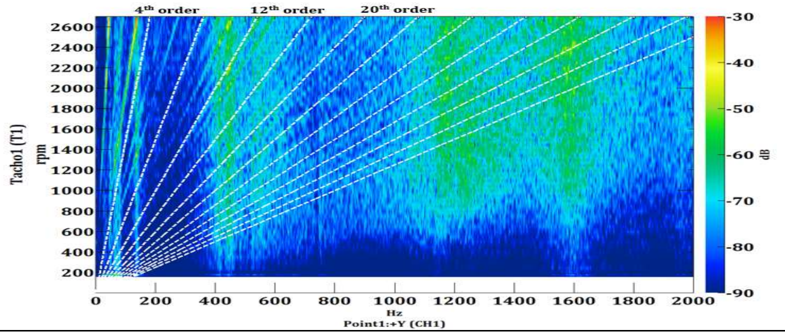

SynRM 12 slots_4 pole

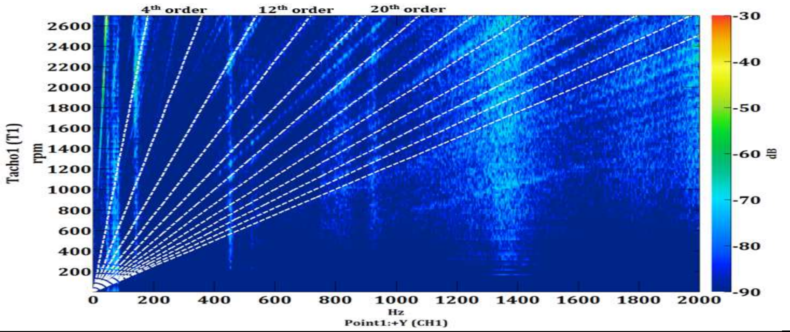

SynRM 27 slots_4 pole

Fig. 5.15 Orders of harmonics frequencies of the analyzed machines band width 0-2kHz

Stators natural frequencies can be identified by analyzing the Fig. 5.16. The resonance frequencies are represented as vertical lines. One can see the dominant modes of the stator for all three motors: ovalization, triangular and square mode. Other modes like pentagon and hexagon can be seen for the 12 slots structure (PSMS and SynRM).

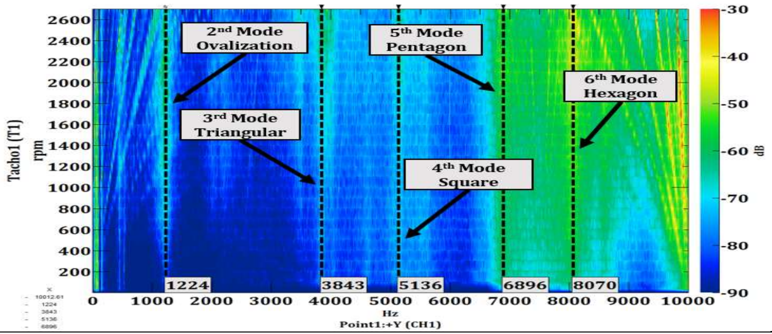

PMSM 12 slots_8 pole

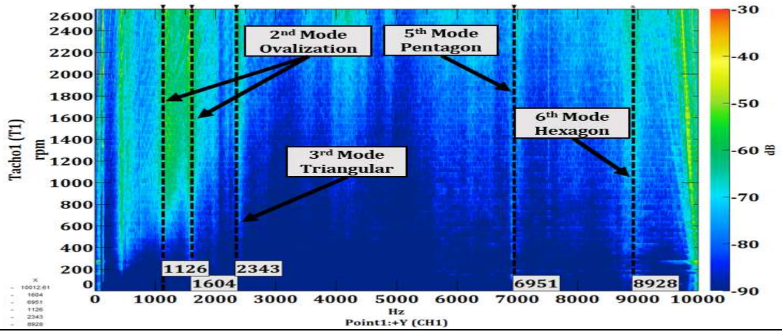

SynRM 12 slots_4 pole

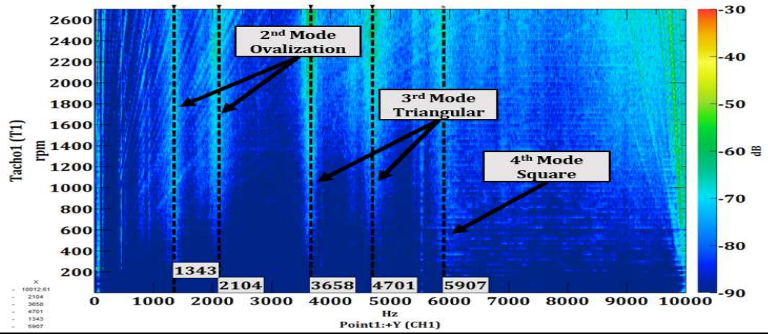

SynRM 27 slots_4 pole

Fig. 5.16 Frequency spectrum of vibration signal with machine orders, band width 0-10 kHz

The generated noise is presented in Fig. 5.17 and Fig. 5.18. The waterfall diagram of acoustic signal under no-load condition is measured by two microphones, one is placed at one-meter distance from the MUT and the second one close to the motor (fixed on the MUT). One can see the noise contribution of the switching frequency and its harmonics and the dominant modes for the acoustic signal of both measurements.

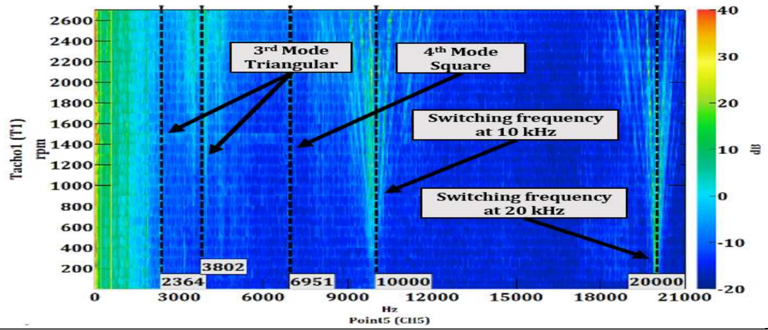

PMSM 12 slots_8 pole 1st microphone results

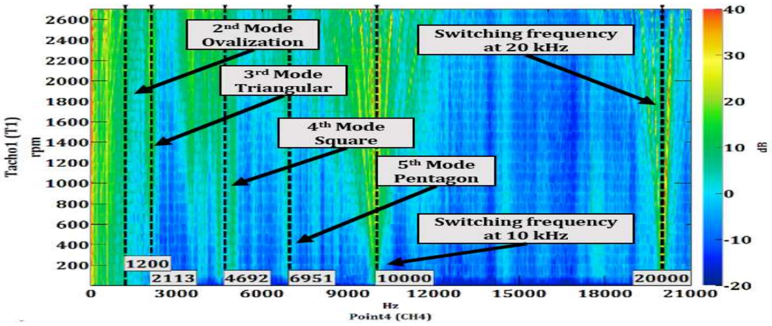

PMSM 12 slots_8 pole 1st microphone results

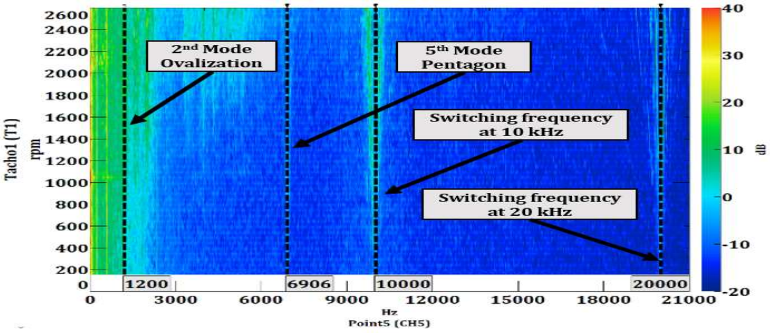

SynRM 27 slots_4 pole 1st microphone results

Fig. 5.17 Frequency spectrum of acoustic signal for the microphone placed at 1 m away from MUT, band width 0-22 kHz, under no load test

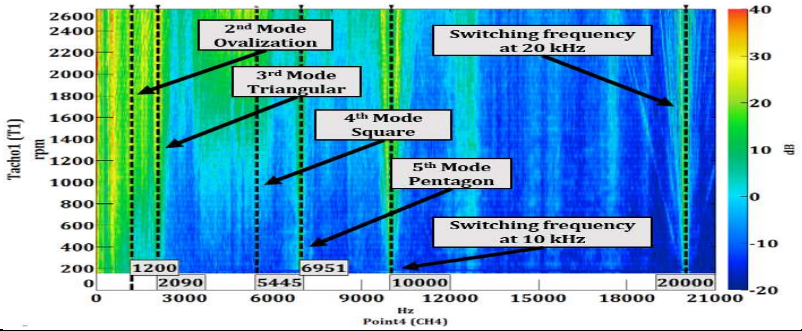

SynRM 12 slots_4 pole 2nd microphone results

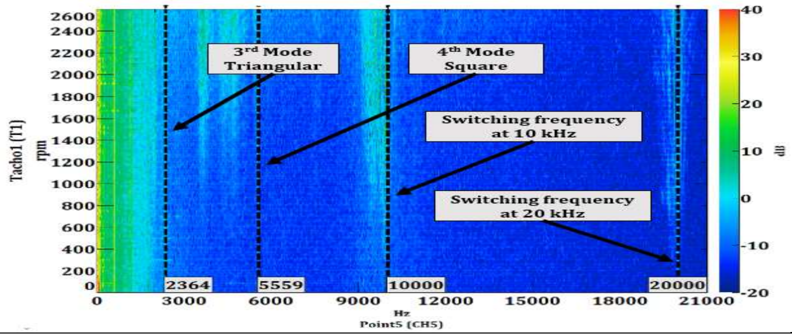

SynRM 12 slots_4 pole 2nd microphone results

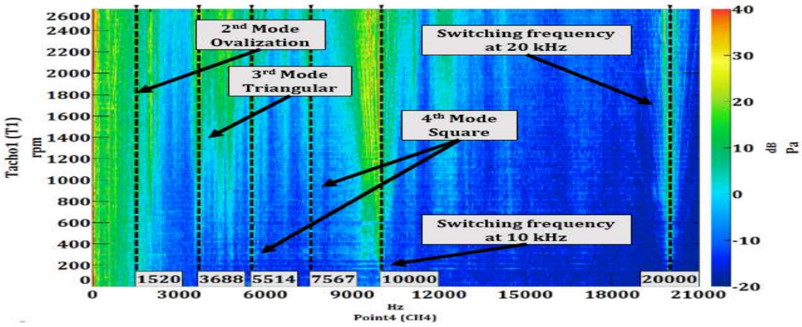

SynRM 27 slots_4 pole 2nd microphone results

Fig. 5.18 Frequency spectrum of acoustic signal for the microphone fixed on the MUT, band width 0-22 kHz, under no load test

The second types of test are performed under load conditions. Here the fan is attached on the MUT. Furthermore, the same measurements have been performed like no-load. The results are shown in Fig. 5.19.

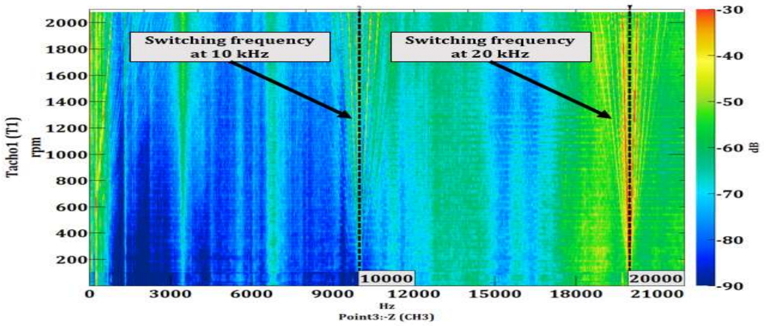

PMSM 12 slots_8 pole

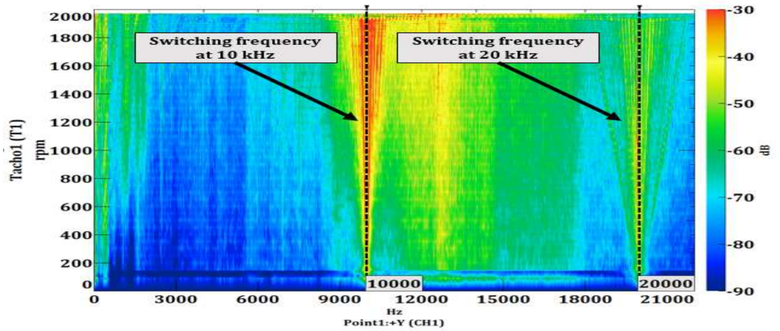

SynRM 12 slots_4 pole

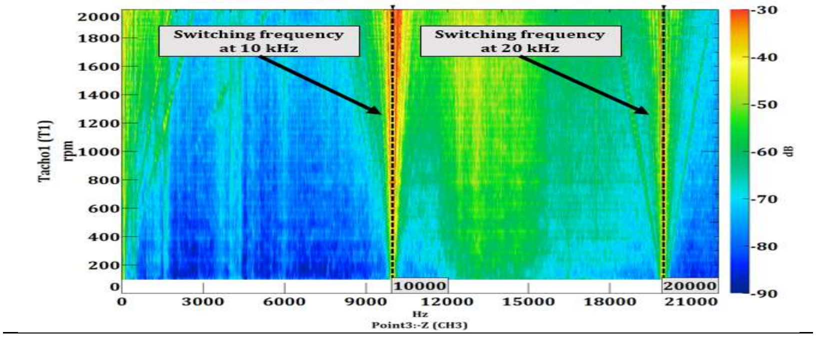

SynRM 27 slots_4 pole

Fig. 5.19 Vibration spectrum for 10 kHz for load condition

Under load conditions, the same dominant modes can be identified, at a similar or close frequency as the ones under no load conditions. For the PMSM structure it can be noticed according Fig. 5.20 that the 3rd and 5th mode is the most predominant. The same remark can be done about the 12 slots SynRM structure were the 3rd mode shape is the most visible.

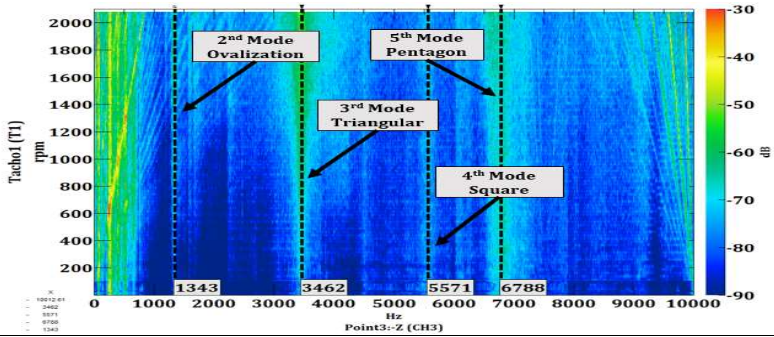

PMSM 12 slots_8 pole

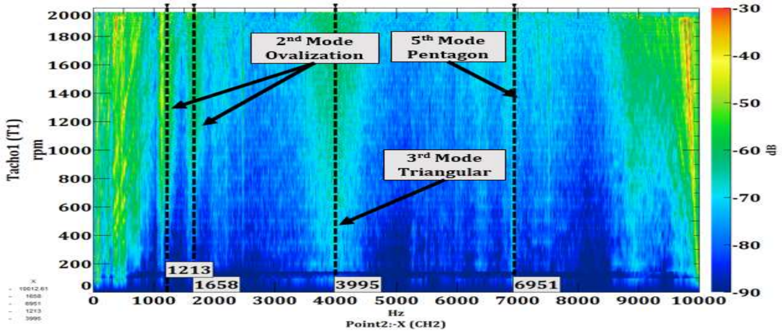

SynRM 12 slots_4 pole

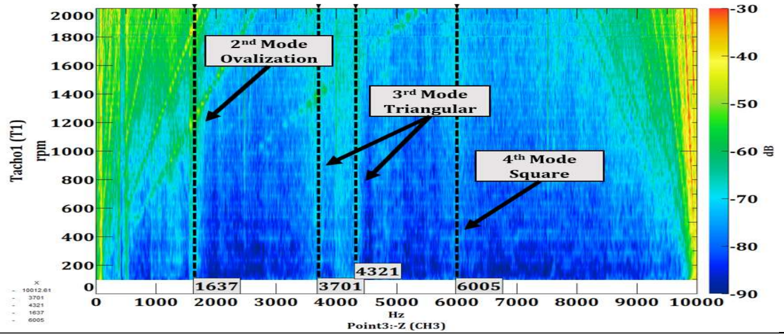

SynRM 27 slots_4 pole

Fig. 5.20 Frequency spectrum of vibration signal with machine orders

On the other hand, according to the same figure, for the 27 slots SynRM, the dominant mode is close to the 2nd mode shape (ovalization). But at the same time the 3rd and the 4th mode are visible.

Next, the acoustic results for both installed microphones under load condition are shown in Fig. 5.21 and Fig. 5.22 respectively.

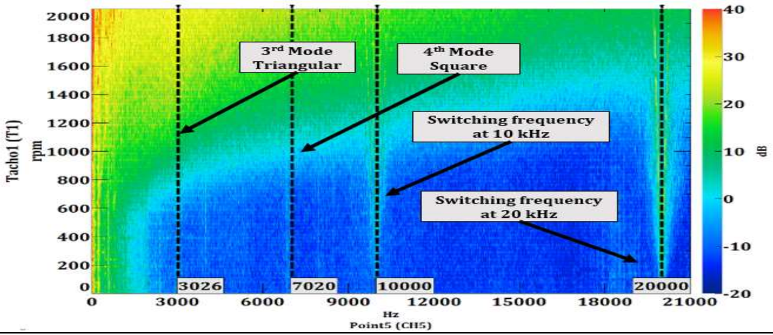

PMSM 12 slots_8 pole 1st microphone results

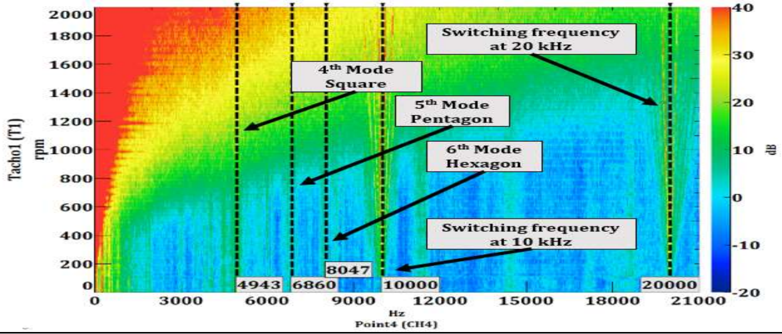

PMSM 12 slots_8 pole 1st microphone results

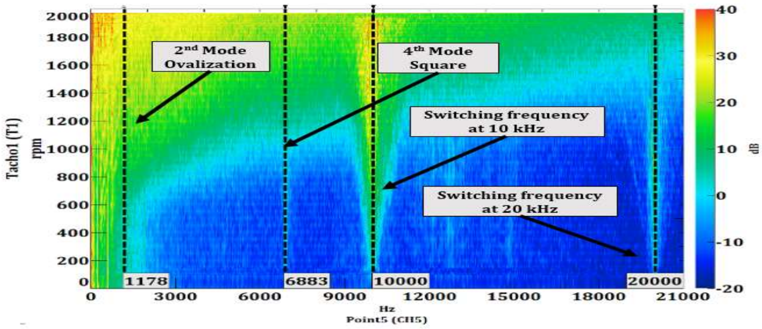

SynRM 12 slots_4 pole 1st microphone results

Fig. 5.21 Frequency spectrum of acoustic signal for the microphone placed at 1 m away from MUT, band width 0-22 kHz, under load test

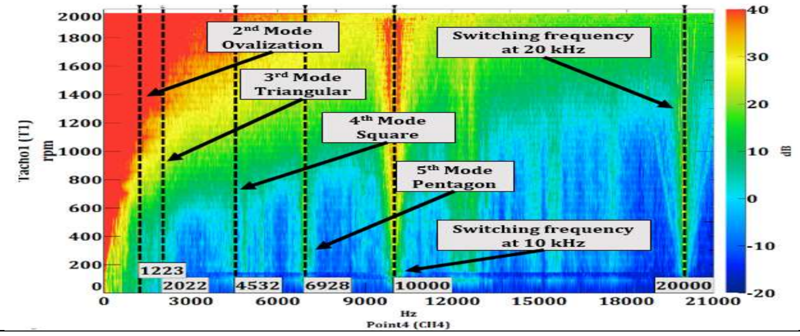

SynRM 12 slots_4 pole 2nd microphone results

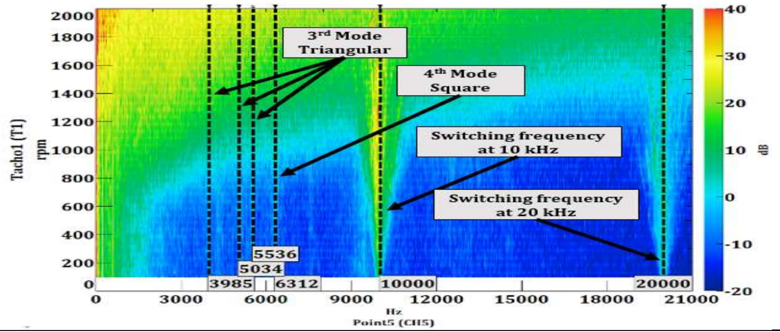

SynRM 27 slots_4 pole 2nd microphone results

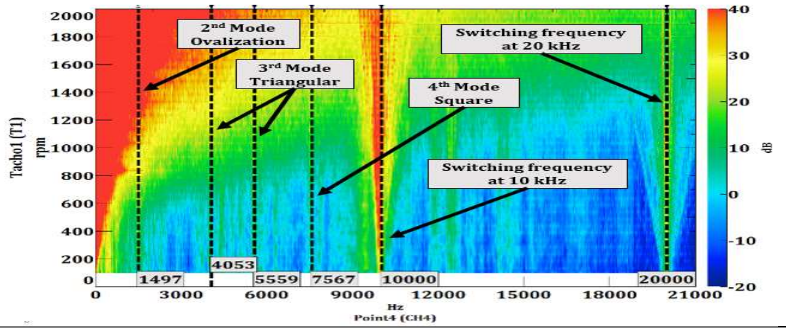

SynRM 27 slots_4 pole 2nd microphone results

Fig. 5.22 Frequency spectrum of acoustic signal for the microphone fixed on the MUT, band width 0-22 kHz, under load test

According to Fig. 5.21 and Fig. 5.22, under both microphones' tests, it is noticeable that the fan noise is the dominating one in all waterfall diagram. Even so, from the acoustic spectrum it can be extracted the natural mode shapes for all three electrical machines. One can see the noise of the switching frequency and its harmonics and the dominant modes for the acoustic signal of both microphones' measurements.

5.4 Conclusions

This chapter has presented the results and verification of the FEA modeled SynRMs design through static (structural analysis) and dynamic measurements (real-time simulation) on the prototyped motors. Laboratory testing it is a “must-have” in the development of an electrical drive system.

In the frame of the thesis the real-time simulation testing approach was applied to validate the design and the simulations results of both developed SynRMs (CW and DW). The measurements are performed in order to highlighting various key performances indicators (mechanical torque, toque ripple, power factor and efficiency).

In addition, the SynRMs were also tested from vibroacoustic point of view, since one of the aims of the thesis was to develop a low noise SynRM used in automotive application. The tests were run in no-load and load state of the machines. Both tests were used to investigate the influence of switching frequency on noise and vibration level of the machines.

6. Final conclusions, contributions and future work

6.1 Final conclusions

This thesis is dedicated to the study and performance enhancement of a SynRM based drive system for low power automotive application. The first Chapter of the thesis puts the work into context highlighting different electrical drives systems. The key requirements and several specifications for such applications are shown. The state of the art and the reason for choosing the SynRM are discussed in the first chapter as well.

The operating principle of the SynRM within the mathematical model, vector diagram and the main design characteristics, have been presented in Chapter 2. In addition, guidelines for slot pole selection, winding configuration and proposed topologies for performance improvements for SynRM are described. After a literature study, in the field of SynRMs design, most of the efforts are being done on proposing different innovative solutions for distributed winding (integral slot) versions. With few exceptions [25, 26], much less attention is being paid to the FSCW-SynRM. Therefore, one of the aims of this thesis is to comprehensively analyze the various attributes of the FSCW-SynRM.

The 3rd Chapter starts with an investigation around a suitable barrier shape design by mean of FEM. The main goal is to reveal the most important design parameters of the rotor structure that affects the machine torque performances. Here, different rotor topologies with one and multi-barrier design have been taken into study.

Further, this chapter reveals a comparative study between eight topologies with different winding pattern (CW and DW) by means of FEM while keeping the same electrical and geometrical parameters in respect to the reference machine (PMSM). The geometry of the SynRMs have been build up by using parametrized coordinates within Python scripts. For better understanding the capabilities of the proposed CW-SynRM designs, they are compared at different stages with the DW-SynRM and ultimately with a CW-PMSM. This chapter has brought many results on the sensitivity analysis that was performed on all the SynRMs structures.

According to the obtained results, it is hard to reach the PMSM torque performances. Obviously, this is a tough requirement due to the lack of the magnets and the lower power factor that this type machine exhibits. To reach the same operating point as the PMSM, a larger value of reactive energy is required (i.e. more current to magnetize the iron core or more voltage when employing the same current but a higher number of turns). Moreover, a comparison between best designs obtained, one with CW and other with DW was performed. The comparison is done highlighting various key performances indicators both electromagnetic (e.g. torque density and quality) and electromechanical level (e.g. torque/efficiency speed characteristics). Both topologies have been re-analyzed and re-optimized in order to achieve the same output power as the reference PMSM. Afterward, the promising designs were compared within the reference PMSM.

Chapter 4 deals with the structural analysis of the machines. A further topic, which is becoming increasingly important in the context of modern electrical drives, is the NVH-behavior. The latter has been addressed both at theoretical and practical level. Numerical and experimental results have been analyzed and compared.

The 5th chapter of this thesis is dedicated to the presentation of the prototyped SynRMs, the experimental setup and the obtained results. A wide range of tests were performed as they were focused on key performances and vibroacoustic measurements, respectively.

In conclusion, the study reached its objective: an overview of SynRMs used for a low power cooling fan automotive application.

6.2 Personal contribution

The main contributions of this work are outlined as follows:

- Summarizing a comprehensive overview of some representative types of auxiliary electric drives, based on case studies used in automotive industry.
- Identifying the design specification for a SynRM applied for a cooling fan used for low-power automotive applications.
- Guidelines for slot pole selection, winding configuration and different topologies for performance improvements for SynRM.

- Investigation around a suitable barrier shape design by means of the FEA.
- Developing parametric 2D FEA models for all analyzed SynRM.
- Integrating the parametrized models in an optimization loop in order to optimize their key-performance indicators.
- A comparative study between all chosen topologies by means of FE-based electromagnetic analyses has been performed.
- Inductance computation using FEA in order to evaluate their dependence with the saturation.
- A comparison between best designs obtained, one with concentrated and other with distributed winding by means of FEA was performed.
- Performing a comparative study of the machines electromagnetic torque and inductances computation via 2D and 3D FEA.
- Performing multiphysics analysis for computing the total deformation of the SynRM stator and rotor core. Theoretically and experimentally analysis have been performed and compared by means of structural behavior of both prototyped designs.
- Contribution to the development of the test bench used for the SynRMs measurements.
- Developing by means of the Contro Desk software of the GUI needed for SynRM testing.
- Testing the developed SynRMs under different operating conditions.

6.3 Future Work

In recent years, axial flux motors (AFMs) have gained attention in automotive, particularly for applications, where there are stringent limitations regarding the axial length (e.g. fans, pumps and in-wheel motors). In this context AFMs can compete against the commonly RF-machines, thanks to their compact geometrical shape and excellent power/weight ratio.

The future work aims to design and optimize an Axial Flux SynRM. According to the literature, there are no previous attempts neither to design nor to manufacture such a motor.

REFERENCES

[1] A. Siemens, "Como - Facts Trends and Stories on Integrated Mobility", September 2014.

[2] C. Early, "Volvo's EV push hints at China's electric ambition," China dialogue, 2017.

[3] E. E. Institute, "Transportation Electrification Utility Fleets Leading the Charge," June 2014.

[4] R. B. GmbH, Bosch Automotive Handbook - 9th Edition, Robert Bosch GmbH, 2017.

[5] Martin Weiss a, "On the electrification of road transportation – A review of the environmental, economic, and social performance of electric two-wheelers," pp. 348-366, 2015.

[6] G. Meyer, "European Roadmap: Electrification of Road Transport." 2nd version," pp. 6-8, 2010.

[7] Eshani, M., Gao, Y., Gay, S. E., & Emadi, A. (2005). Modern electric, hybrid electric and fuel cell vehicles. Fundamentals, Theory, and Design. Boca Raton, FL: CRC

[8] Z. Schlanger, Quartz, May 18, 2017.

[9] C. Atiyeh, "Everything You Need to Know about the VW Diesel-Emissions Scandal," May 11, 2017.

[10] Nesbit, M., Fergusson, M., Colsa, A., Ohlendorf, J., Hayes, C., Paquel, K., & Schweitzer, J. P. (2016). Comparative study on the differences between the EU and US legislation on emissions in the automotive sector. European Parliament Directorate General for Internal Policies, B-1047, Brussels, Belgium, 1-90.

[11] O. M. Bernhard Klein, "48 Volt Technology," DIE BIBLIOTHEK DER TECHNIK, vol. 388, no. Continental, 2016.

[12] Vidal, "www.theguardian.com," 21 April 2005. [Online]. Available: https://www.theguardian.com/science/2005/apr/21/oilandpetrol.news.

[13] N. E. BOUDETTE, "Tesla's First Mass-Market Car, the Model 3, Hits Production This Week," 3 07 2017. [Online]. Available:

https://www.nytimes.com/2017/07/03/business/tesla-model-3-elon-musk.html?mcubz=1.

[14] M. Duvall, Discussions of the benefits and impacts of plug in hybrid and battery electric vehicles, MIT Energy Initiative, 2010.

[15] Larminie, J., & Lowry, J. (2012). Electric vehicle technology explained. John Wiley & Sons.

[16] B. Lequesne, "Automotive electrification: The nonhybrid story," IEEE Transactions on Transportation Electrification, pp. 40–53, 2015.

[17] J. De Santiago, H. Bernhoff, B. Ekergard, S. Eriksson, S. Ferhatovic, R. Waters, & M. Leijon, "Electrical motor drivelines in commercial allelectric vehicles: A review," IEEE Transactions on vehicular technology, vol. 61(2), 475-484, 2012

[18] A. C. Pop and J. J. C. Gyselinck and D. E. Pinto and I. Vintiloiu, "Optimization of Low-Power Brushless PM-Machines for Automotive Applications With Focus on High-Volume Mass Production", IEEE Transactions on Industrial Electronics, vol. 64, pp. 9767–9775, 2017

[19] S. Taghavi," Design of Synchronous Reluctance Machines for Automotive Applications", Doctoral dissertation, Concordia University, 2015.

[20] S. Ruoho, Demagnetisation of permanent magnets in electrical machines, OH presentation, Helsinki University, 2007.

[21] Conrad, F. (1913). Electrical equipment of gasoline automobiles. Proceedings of the American Institute of Electrical Engineers, 32(11), 1995-2005.

[22] Charette, R. N. (2009). This car runs on code. IEEE spectrum, 46(3), 3.

[23] Press release: IAA 2017: Brose showcases "Competence in Mechatronics" for the vehicles of tomorrow http://www.presseportal.de/pm/33971/3734810

[24] Pop, A. C., Petrus, V., Martis, C. S., Iancu, V., & Gyselinck, J. (2012, May). Comparative study of different torque sharing

functions for losses minimization in Switched Reluctance Motors used in electric vehicles propulsion. In 2012 13th International Conference on Optimization of Electrical and Electronic Equipment (OPTIM) (pp. 356-365). IEEE.

[25] Donaghy-Spargo, C. M. (2016). Synchronous reluctance motors with fractional slot-concentrated windings (Doctoral dissertation, Newcastle University).

[26] Spargo, C. M., Mecrow, B. C., & Widmer, J. D. (2014). Higher pole number synchronous reluctance machines with fractional slot concentrated windings.

[27] Kamper, M. (2013, July). Reluctance synchronous machine drives-a viable alternative? In IEEE Joint IAS/PELS/IES Chapter Meeting (p. 69).

[28] K.Wang, Z.Q. Zhu, G. Ombach, M. Koch, S. Yhang, J. XU, "Optimal Slot/Pole and Flux-Barrier Layer Number Combination for Synchronous Reluctance Machine", Ecological Vehicles and Renewable Energies (EVER), 2013 8th International Conference, 2013

[29] Staton, D. A., Miller, T. J. E., & Wood, S. E. (1993, July). Maximising the saliency ratio of the synchronous reluctance motor. In IEE Proceedings B-Electric Power Applications (Vol. 140, No. 4, pp. 249-259). IET.

[30] Kostko, ":Polyphase Reaction Synchronous Motor", Journal of AIEE, vol 42, 1923, pp. 1162-1168

[31] Small step, big impact –energy efficiency and dynamic performance, Available: https://www.industry.siemens.com

[32] REEL SuPremE® motor: Premium IE5/IE4 efficiency without magnets, Available: https://www.ksb.com/REEL-en/

[33] R. Moghaddam, "Synchronous Reluctance Machine (SynRM) in Variable Speed Drives (VSD) Applications", Doctoral Thesis, Stockholm, Sweden 2011

[34] **Pop, F. P., Popa, D. C., Marţiş, R., Marţiş, C., & Pop, A. C. (2017, June). Comparative analysis of rare earth-less electrical machines for 48V automotive cooling fan applications. In 2017 14th International Conference on**

Engineering of Modern Electric Systems (EMES) (pp. 180-183). IEEE.

[35] **Florin, P. P., Mircea, R., Adrian-Cornel, P., Martis, R., & Martis, C. (2018, September). Comparative Analysis for an Electric Power Steering System. In 2018 XIII International Conference on Electrical Machines (ICEM) (pp. 590-596). IEEE.**

[36] Bumby, J., Crossland, S., & Carter, J. (2006). Electrically assisted turbochargers: Their potential for energy recovery.

[37] H. Hofmann and S. R. Sanders, "High-speed synchronous reluctance machine with minimized rotor losses," in IEEE Transactions on Industry Applications, vol. 36, no. 2, pp. 531-539, March-April 2000. doi: 10.1109/28.833771

[38] M. E. Hadi Zaim, "High-Speed Solid Rotor Synchronous Reluctance Machine Design and Optimization," in IEEE Transactions on Magnetics, vol. 45, no. 3, pp. 1796-1799, March 2009. doi: 10.1109/TMAG.2009.2012824

[39] M. Palmieri, M. Perta and F. Cupertino, "Design of a 50.000 rpm synchronous reluctance machine for an aeronautic diesel engine compressor," 2014 IEEE Energy Conversion Congress and Exposition (ECCE), Pittsburgh, PA, 2014, pp. 5138-5143. doi: 10.1109/ECCE.2014.6954106

[40] Tiberiu, R., Adrian-Cornel, P., & Loránd, S. (2016). Noise Harshness and Vibration Characterization of Switched Reluctance Motors. Journal of Computer Science and Control Systems, 9(2), 34.

[41] https://www.auto-data.net/en/tesla-model-s-85-362hp-18611

[42] Zwei die elektroindutrie Voltage classes for electric Mobility

Available https://www.zvei.org/fileadmin/user_upload/Presse_und_Medien/Publikationen/2014/april/Voltage_Classes_for_Electric_Mobility/Voltage_Classes_for_Electric_Mobility.pdf

[43] Xue, X. D., Cheng, K. W. E., & Cheung, N. C. (2008, December). Selection of electric motor drives for electric vehicles. In

Power Engineering Conference, 2008. AUPEC'08. Australasian Universities (pp. 1-6). IEEE.

[44] http://www.eurocarnews.com/0/0/43/0/2010-audi-a3-drivetrain-and-steering-in-detail.html

[45] https://www.vi-grade.com/en/solutions/electric_power_steering/

[46] N. Bianchi, S. Bolognani, E. Carraro, M. Castiello and E. Fornasiero, "Electric Vehicle Traction Based on Synchronous Reluctance Motors," in IEEE Transactions on Industry Applications, vol. 52, no. 6, pp. 4762-4769, Nov.-Dec. 2016. doi: 10.1109/TIA.2016.2599850

[47] F.Melzer,U.Hesse,G.Rocklage, andM. Schmitt, “Thermomanagement,” presented at the SAE World Congr., Detroit, MI, USA, Mar. 1999, Paper 1999-01-0238.

[48] https://www.aa1car.com/library/electric_cooling_fan.htm

[49] S. Tahi, R. Ibtiouen i M. Bounekhla, „Design Optimization of Two Synchronous Reluctance Machine Structures with Maximized Torque and Power Factor,” Progress in Electromagnetics Research, 2011.

[50] Huynh, T. A., & Hsieh, M. F. (2017). Comparative study of PM-assisted SynRM and IPMSM on constant power speed range for EV applications. IEEE Transactions on Magnetics, 53(11), 1-6.

[51] J.-K. Lee, D.-H. Jung, J. Lim, Y. J. Oh, K.-D. Lee i J. Lee, „Rotor Open-Rib Design for Power Density Improvement in Synchronous Reluctance Motor,” Journal of Magnetics, 2018.

[52] S. Tahi, R. Ibtiouen i M. Bounekhla, „Design Optimization of Two Synchronous Reluctance Machine Structures with Maximized Torque and Power Factor,” Progress in Electromagnetics Research, 2011.

[53] Pyrhonen, J., Jokinen, T., & Hrabovcova, V. (2013). Design of rotating electrical machines. John Wiley & Sons.

[54] Niazi, P., Toliyat, H. A., & Goodarzi, A. (2007). Robust maximum torque per ampere (MTPA) control of PM-assisted SynRM for

traction applications. IEEE transactions on vehicular technology, 56(4), 1538-1545.

[55] Moghaddam, R. R., & Gyllensten, F. (2013). Novel high-performance SynRM design method: An easy approach for a complicated rotor topology. IEEE Transactions on Industrial Electronics, 61(9), 5058-5065.

[56] Vartanian, R., & Toliyat, H. A. (2009, April). Design and comparison of an optimized permanent magnet-assisted synchronous reluctance motor (PMa-SynRM) with an induction motor with identical NEMA Frame stators. In 2009 IEEE Electric Ship Technologies Symposium (pp. 107-112). IEEE.

[57] Taghavi, S., & Pillay, P. (2014, October). A comparative study of synchronous reluctance machine performance with different pole numbers for automotive applications. In IECON 2014-40th Annual Conference of the IEEE Industrial Electronics Society (pp. 3812-3818). IEEE.

[58] Hendershot, J. R. (1989). U.S. Patent No. 4,883,999. Washington, DC: U.S. Patent and Trademark Office.

[59] Available: https://www.emetor.com/windings/

[60] Boldea, I., & Tutelea, L. (2018). Reluctance Electric Machines: Design and Control. CRC Press.

[61] Stator/Rotor Pole combinations and winding configurations of variable flux reluctance machines, X. Liu, Z. Q. Zhu

[62] Florence Meier, "*Permanent-Magnet Synchronous Machines with Non-Overlapping Concentrated Windings for Low-Speed Direct-Drive Applications.*" Ph D Theses, Stockholm 2008

[63] J. Cros and P. Viarouge, "*Synthesis of high-performance PM motors with concentrated windings*," in IEEE Trans. on Energy Conversion, vol. 17, no. 2, pp. 248-253, 2002.

[64] A. EL-Refaie, "*High speed operation of permanent magnet machines*." Doctoral thesis, University of Wisconsin-Madison, USA, 2005

[65] M. Cistelecan, B. Cosan, and M. Popescu, "*Tooth Concentrated Fractional Windings for low speed three phase a.c. machines*,"

in Proc. of Int. Conf. on Electrical Machines, (ICEM), paper no. 362, 2006.

[66] Germishuizen, "*Design and performance characteristics of IPM machines with single layer non-overlapping concentrated windings*," in Proc. of IEEE Industry Applications Society Conf., pp. 141-147, 2007

[67] **Pop, F. P., Marţiş, R., Dărămus, A., Marţiş, C., Pop, A. C., & Vintiloiu, I. (2016, October). Design and analysis of slot-pole combination for synchronous reluctance machine with concentrated windings for automotive applications. In 2016 International Conference and Exposition on Electrical and Power Engineering (EPE) (pp. 229-234). IEEE.**

[68] P. Salminen, M. Niemel¨a, and J. Pyrh¨onen, "*Performance analysis of fractional slot wound PM-motors for low speed applications*," in Proc. of IEEE Industry Applications Society Conf., vol. 2, pp. 1032-1037, 2005.

[69] N. Bianchi, S. Bolognani, and M. D. Pr´e, "*Magnetic loading of fractional-slot threephase PM motors with non-overlapped coils*," in Proc. of IEEE Industry Applications Society Conf., vol. 1, pp. 37-43, 2006.

[70] E. Armando, P. Guglielmi, G. Pellegrino, M. Pastorelli, A. Vagati, "Accurate Modeling and Performance Analysis of IPM-PMASR Motors", IEEE Transactions on Industry Applications, vol. 45, Issue 1, Jan.-Feb. 2009, pp. 123-130.

[71] Iga, Y., Takahashi, K., & Yamamoto, Y. (2016). Finite element modelling of turbine generator stator end windings for vibration analysis. IET Electric Power Applications, 10(2), 75-81.

[72] Cheng, R., & Jin, Y. (2015). A social learning particle swarm optimization algorithm for scalable optimization. Information Sciences, 291, 43-60.

[73] Lee, J. H., Kim, J. W., Song, J. Y., Kim, Y. J., & Jung, S. Y. (2015). A novel memetic algorithm using modified particle swarm optimization and mesh adaptive direct search for PMSM design. IEEE Transactions on Magnetics, 52(3), 1-4.

[74] López, C., Michalski, T., Espinosa, A., & Romeral, L. (2016, September). Rotor of synchronous reluctance motor optimization by means reluctance network and genetic algorithm. In 2016 XXII International Conference on Electrical Machines (ICEM) (pp. 2052-2058). IEEE.

[75] J.-K. Lee, D.-H. Jung, J. Lim, Y. J. Oh, K.-D. Lee i J. Lee, „Rotor Open-Rib Design for Power Density Improvement in Synchronous Reluctance Motor," Journal of Magnetics, 2018.

[76] F. Daldaban, & E. Cetin, "Prototyping of Axial Flux Permanent Magnet Motors," 3rd International Symposium on Innovative Technologies in Engineering and Science, vol. 13, 2015.

[77] A. Cavagnino, M. Lazzari, F. Profumo, & A. Tenconi, "A comparison between the axial flux and the radial flux structures for PM synchronous motors," IEEE transactions on industry applications, vol. 38(6), pp. 1517-1524, 2002

[78] W. E. Jara Montecinos, "Axial Flux Permanent Magnet MachinesDevelopment of Optimal Design Strategies", Acta Universitatis Lappeenrantaensis, 2016.

[79] F. Daldaban, & E. Cetin, E., "Prototyping of Axial Flux Permanent Magnet Motors," in 3rd International Symposium on Innovative Technologies in Engineering and Science, ISITES A (Vol. 13), 2015

[80] W. E. Jara Montecinos, "Axial Flux Permanent Magnet MachinesDevelopment of Optimal Design Strategies," Acta Universitatis Lappeenrantaensis, 2016.

[81] I. Boldea, Z. X. Fu, & S. A. Nasar, "Performance evaluation of axiallylaminated anisotropic (ALA) rotor reluctance synchronous motors", IEEE Industry

[82] B. Scheerlinck, H. De Gersem, & P. Sergeant, "3-D Eddy Current and Fringing-Flux Distribution in an Axial-Flux Permanent-Magnet Synchronous Machine With Stator in Laminated Iron or SMC.", IEEE Transactions on Magnetics, vol. 51(11), pp. 1–4 2015.

[83] L. O. Hultman, A. G. Jack, "Soft magnetic composites-materials and applications," IEEE International Electric Machines and Drives Conference, (IEMDC'03), vol.1, pp. 516-522, 2003

[84] G. Lei, J. G. Zhu, Y. G. Guo, J. F. Hu, W. Xu & K. R. Shao, ”Robust Design Optimization of PM-SMC Motors for Six Sigma Quality Manufacturing,” in IEEE

[85] O. Andersson, P. Hofecker, ”Advances in Soft Magnetic Composites Materials and Applications”, PowderMet2009, 2009.

[86] P. Pszola, M. Pszola, ”Stack System of an Electric Machine, Electric Machine, and Method for Producing the Stack System,” patent application number PCT/EP2017/054942, 2017.

[87] J. Gyselinck, C. Geuzaine, & R. V. Sabariego,” Considering laminated cores and eddy currents in 2D and 3D finite element simulation of electrical machines”, in Proceedings of the 18th Conference on the Computation of Electromagnetic Fields (COMPUMAG2011), Sydney, Australia. 2011.

[88] R. V. Sabariego, I. Niyonzima, J. Gyselinck & C. Geuzaine, ”Comparison of two nonlinear finite-element homogenization methods for laminated iron cores”, 2013.

[89] Fang, H., Li, D., Qu, R., & Yan, P. (2018). Modulation effect of slotted structure on vibration response in electrical machines. IEEE Transactions on Industrial Electronics, 66(4), 2998-3007.

[90] Vaks, N., Zarate, N., & Xiaoqi, W. A. N. G. (2019). U.S. Patent No. 10,199,976. Washington, DC: U.S. Patent and Trademark Office.

[91] Takiguchi, M., Sugimoto, H., Kurihara, N., & Chiba, A. (2015). Acoustic noise and vibration reduction of SRM by elimination of third harmonic component in sum of radial forces. IEEE Transactions on Energy Conversion, 30(3), 883-891.

[92] Islam, R., & Husain, I. (2010). Analytical model for predicting noise and vibration in permanent-magnet synchronous motors. IEEE Transactions on industry applications, 46(6), 2346-2354.

[93] Verez, G., Barakat, G., Amara, Y., & Hoblos, G. (2015). Impact of pole and slot combination on vibrations and noise of electromagnetic origins in permanent magnet synchronous motors. IEEE Transactions on Magnetics, 51(3), 1-4.

[94] Rezig, A., Mekideche, M. R., & Djerdir, A. (2010). Effect of rotor eccentricity faults on noise generation in permanent magnet synchronous motors. Progress In Electromagnetics Research, 15, 117-132.

[95] Gieras, J. F., Wang, C., Joseph, C. L., & Ertugrul, N. (2007, May). Analytical prediction of noise of magnetic origin produced by permanent magnet brushless motors. In 2007 IEEE International Electric Machines & Drives Conference (Vol. 1, pp. 148-152). IEEE.

[96] Ebrahimi, B. M., Roshtkhari, M. J., Faiz, J., & Khatami, S. V. (2013). Advanced eccentricity fault recognition in permanent magnet synchronous motors using stator current signature analysis. IEEE Transactions on Industrial Electronics, 61(4), 2041-2052.

[97] Yacamini, R., & Chang, S. C. (1995). Noise and vibration from induction machines fed from harmonic sources. IEEE Transactions on energy conversion, 10(2), 286-292.

[98] Jung, J. W., Lee, S. H., Lee, G. H., Hong, J. P., Lee, D. H., & Kim, K. N. (2010). Reduction design of vibration and noise in IPMSM type integrated starter and generator for HEV. IEEE Transactions on Magnetics, 46(6), 2454-2457.

[99] Gieras, J. F., Wang, C., & Lai, J. C. (2018). Noise of polyphase electric motors. CRC press.

[100] methods used to calculate the forces acting between the rotor and the stator boundary (air-gap)

[101] Tenhunen, A., Benedetti, T., Holopainen, T. P., & Arkkio, A. (2003). Electromagnetic forces of the cage rotor in conical whirling motion. IEE Proceedings-Electric Power Applications, 150(5), 563-568.

[102] Vijayraghavan, P., & Krishnan, R. (1999). Noise in electric machines: A review. IEEE Transactions on Industry Applications, 35(5), 1007-1013.

[103] Tenhunen, A., Benedetti, T., Holopainen, T. P., & Arkkio, A. (2003). Electromagnetic forces of the cage rotor in conical whirling motion. IEE Proceedings-Electric Power Applications, 150(5), 563-568.

[104] Gulez, K., Adam, A. A., & Pastaci, H. (2008). Torque ripple and EMI noise minimization in PMSM using active filter topology and field-oriented control. IEEE Transactions on Industrial Electronics, 55(1), 251-257.

[105] Girgis, R. S., & Vermas, S. P. (1981, January). Method for accurate determination of resonant frequencies and vibration behaviour of stators of electrical machines. In IEE Proceedings B (Electric Power Applications) (Vol. 128, No. 1, pp. 1-11). IET Digital Library.

[106] Saito, A., Kuroishi, M., & Nakai, H. (2016, September). Vibration prediction method of electric machines by using experimental transfer function and magnetostatic finite element analysis. In Journal of Physics: Conference Series (Vol. 744, No. 1, p. 012088). IOP Publishing.

[107] Available : https://cogent-power.com/cms data/downloads/m800-50a.pdf

[108] **Piglesan, F. P., Martis, R., Martis, C., Faria, C., & Chauvicourt, F. (2018, October). Electromagnetic and NVH study for low power Synchronous Reluctance Machine. In 2018 AEIT International Annual Conference (pp. 1-6). IEEE.**

[109] Qatu, M. S., Abdelhamid, M. K., Pang, J., & Sheng, G. (2009). Overview of automotive noise and vibration. International Journal of Vehicle Noise and Vibration, 5(1-2), 1-35.

[110] Faria, C., Santos, F., Chauvicourt, F., & Orlando, S. (2015). Noise emissions on switched reluctance motors: evaluation of different structural models. World Electric Vehicle Journal, 7(2), 179-186.

[111] **Pop, F. P., Popa, D. C., Marţiş, R., Marţiş, C., & Pop, A. C. (2017, June). Comparative analysis of rare earth-less electrical machines for 48V automotive cooling fan applications. In Engineering of Modern Electric Systems (EMES), 2017 14th International Conference on (pp. 180-183). IEEE.**

[112] http://37signals.com/svn/images/audi_r8_draw_07_1.png

LIST OF FIGURES

Fig. 1.1 The auxiliaries power consumptions in common automobiles

Fig. 1.2 Overview of automotive electric drives application

Fig. 1.3 SynRM rotor design: (a) Simple salient pole (SP) rotor, (b) Axially laminated anisotropic (ALA) rotor, (c) Transversally laminated anisotropic (TLA) rotor

Fig. 1.4 The electromechanical subsystems on board [19]

Fig. 1.5 Choices of drivetrain system in an EV [43]

Fig. 1.6 Required Torque vs Speed characteristic for an BMW I3 powertrain [44]

Fig. 1.7 Electric Power Assisted Steering system [44], [45]

Fig. 1.8 Required Torque vs Speed characteristic for an electric power assisted steering

Fig. 1.9 Engine cooling system diagram [47]

Fig. 1.10 Required Torque vs Speed characteristic for a CFM

Fig. 2.1 Reluctance concept explained

Fig. 2.2 Magnetic field and reluctance torque production

Fig. 2.3 Variation of inductance with respect to rotor position

Fig. 2.4 d-axis (left) and q-axis (right) equivalent circuit of SynRM

Fig. 2.5 SynRM phasor diagram

Fig. 2.6 Stator current position in d/q frame

Fig. 2.7 12 slots / 4 poles CW layout

Fig. 2.8 12 Slots/4 poles topology stator design with one (a) and (b) double layer

Fig. 2.9 Needle winding technique for CW-machines [62]

Fig. 2.10 27 slots / 4 poles concentrated winding layout

Fig. 2.11 Slots / 4 poles topology stator design with one (a) and (b) double layer distribution

Fig. 2.12 (a, b, c, d, e and f) Historical evolutions of different alternative rotor geometries [29]

Fig. 2.13 Current market of SynRM [27,31,32]

Fig. 2.14 4-pole TLA SynRM rotor design

Fig. 2.15 Multiphysics workflow for studied SynRM

Fig. 2.16 Flowchart of the optimization process

Fig. 3.1 Parameter definition for one barrier sizing and position in d-q axis

Fig. 3.2 Flux barrier parameters

Fig. 3.3 Electromagnetic torque for different barrier thickness in q-axis (left) and simulated designs (right)

Fig. 3.4 Average torque and torque ripple for all simulated scenarios

Fig. 3.5 Electromagnetic torque for different barrier position in q-axis (left) and simulated designs (right)

Fig. 3.6 Average torque and torque ripple for all simulated scenarios

Fig. 3.7 Electromagnetic torque for different barrier angle (left) and simulated designs (right)

Fig. 3.8 Average torque and torque ripple for all simulated scenarios

Fig. 3.9 Inductances in d and q-axis for different number of flux barriers

Fig. 3.10 Electromagnetic torque from 1 until 4 flux barriers per pole (left) and simulated designs (right)

Fig. 3.11 Electromagnetic torque from 5 until 8 flux barriers per pole (left) and simulated designs (right)

Fig. 3.12 Effect of number of barriers on torque ripple (left) and saliency ratio (right) in respect to electromagnetic torque

Fig. 3.13 Cross-section of the analyzed PMSM-spoke design

Fig. 3.14 Cross section of the analyzed SyRMs

Fig. 3.15 Maximum number of turns per slot CW

Fig. 3.16 Circuit diagram of the current source simulation method

Fig. 3.17 The mesh in the air-gap region

Fig. 3.18 Flux density and flux lines in aligned position at RMS phase current 17A

Fig. 3.19 Electromagnetic torque waveforms (a) and torque vs speed for rated current limit (b)

Fig. 3.20 Electromagnetic torque vs current angle, optimum current angle

Fig. 3.21 Torque versus current angle, varying the stator current amplitude

Fig. 3.22 Calculated Efficiency vs Speed characteristic, Power Factor (b) and Saliency Ratio (c), for rated current

Fig. 3.23 FEA calculated d- and q-axis inductances

Fig. 3.24 BH-Curve and the Specific core losses versus magnetic flux density plots for M800-50A lamination

Fig. 3.25 Iron core losses results

Fig. 3.26 Cross section of the analyzed DW-SyRMs

Fig. 3.27 Maximum number of turns per slot

Fig. 3.28 Flux density and flux lines in aligned position at RMS phase current 17A

Fig. 3.29 Electromagnetic torque waveforms (a) and torque vs speed for rated current limit (b)

Fig. 3.30 Electromagnetic torque vs current angle, optimum current angle

Fig. 3.31 Torque versus current angle, varying the stator current amplitude

Fig. 3.32 Calculated Efficiency vs Speed characteristic, Power Factor (b) and Saliency Ratio (c), for rated current

Fig. 3.33 FEA calculated d- and q-axis inductances

Fig. 3.34 Iron core losses results

Fig. 3.35 Stator parameters variation (a) filling factor optimization (b)

Fig. 3.36 SynRM obtained before and after optimization CW-design (a) DW-design (b)

Fig. 3.37 Winding arrangement and the prototyped designs

Fig. 3.48 Electromagnetic torque for initial and resized designs (a) and torque vs speed characteristic (b)

Fig. 3.39 Key performance indicators for both SynRMs

Fig. 3.40 3D model of the prototype machines a) concentrated winding and b) distributed winding

Fig. 3.41 2D vs 3D FEA calculated d- q- axis inductances a) concentrated windings and b) distributed windings

Fig. 3.42 2D vs 3D FEA Torque waveforms a) concentrated windings and b) distributed windings)

Fig. 3.43 Iron losses waveforms a) concentrated windings and b) distributed windings)

Fig. 4.1 Sphere of influence meshing method

Fig. 4.2 von- Mises stress at 2700 rpm

Fig. 4.3 Total deformation at 2700 rpm

Fig. 4.4 von- Mises stress at 5400rpm

Fig. 4.5 Total deformation at 5400 rpm

Fig. 4.6 The FEM model of the stator core

Fig. 4.7 Mode shapes of the investigated machines

Fig. 4.8 Structure fixation
Fig. 4.9 3-dimensional sensor
Fig. 4.10 Bookmarks for simulation
Fig. 4.11 FRF and sum of FRF resulted from measurements for 12 slots structure
Fig. 4.12 FRF and sum of FRF resulted from measurements for 27 slots structure
Fig. 5.1 3D CAD model of prototype CW-SynRM
Fig. 5.2 Manufacturing parts for all studied electrical machines
Fig. 5.3 Resolver mounted on the end side of the shaft
Fig. 5.4 Test bench structure
Fig. 5.5 Test bench schematic
Fig. 5.6 Torque-speed characteristic of the used load Fan
Fig. 5.7 Torque vs. speed characteristic (with Fan load)
Fig. 5.8 Test bench with DC-load for CPSR study
Fig. 5.9 FEA and experimental measurements of CW-SynRM performed at 2000 rpm
Fig. 5.10 FEA and experimental measurements of DW-SynRM performed at 2200 rpm
Fig. 5.11 Key performances comparison between FEA and measured
Fig. 5.12 N&V test equipment
Fig. 5.13 Speed Test -Profile
Fig. 5.14 Vibration spectrum for 10 kHz and 20 kHz switching frequency for no-load condition
Fig. 5.15 Orders of harmonics frequencies of the analyzed machines
Fig. 5.16 Frequency spectrum of vibration signal with machine orders

Fig. 5.17 Frequency spectrum of acoustic signal for the microphone placed at 1 m away from MUT, band width 0-22 kHz, under no load test

Fig. 5.18 Frequency spectrum of acoustic signal for the microphone fixed on the MUT, band width 0-22 kHz, under no load test

Fig. 5.19 Vibration spectrum for 10 kHz for load condition

Fig. 5.20 Frequency spectrum of vibration signal with machine orders

Fig. 5.21 Frequency spectrum of acoustic signal for the microphone placed at 1 m away from MUT, band width 0-22 kHz, under load test

Fig. 5.22 Frequency spectrum of acoustic signal for the microphone fixed on the MUT, band width 0-22 kHz, under load test

Fig. 1A (a) Stator geometrical parameters in the FE model

Fig. 2A (b) Rotor geometrical parameters in the FE model

Fig. 3A Flowchart of the optimization process

Fig. 4A Pareto front sensitivity analysis for different geometric parameters with impact on the motor structure

Fig. 5A Scatter plot of 10.000 candidate optimized with PSO quantifying the improvements of SynRM

Fig. 6A Pareto front of flux barriers parameters optimized with PSO

Fig. 7A SynRM geometries obtained before (green line) and after optimization process (blue dotted line)

Fig. 8A (a) Torque vs Speed characteristic - plotted area of the initial and optimized design (b) Saliency ratio and power factor comparison

LIST OF TABLES

TABLE 1.1 Machine technologies comparison
TABLE 1.2 The electromechanical subsystems on board explained
TABLE 1.3 Requirements of several electric drives in automotive applications
TABLE 1.4 Technical specifications of electric vehicles [47]
TABLE 1.5 Vehicles and power categories considered
TABLE 1.6 Specification data for an BMW I3 42.2 kWh
TABLE 1.7 Specification data for the electric motor for an electric power assisted steering [35]
TABLE 1.8 Specification data for a cooling fan motor [54]
TABLE 2.1 Phase number for balanced windings
TABLE 2.2 Slot and pole combination for three phase balanced windings
TABLE 2.3 Comparison between selected winding types
TABLE 2.4 Comparison between single and double – layer concentrated windings
TABLE 3.1 Main geometrical and electrical parameters for the studied SynRM
TABLE 3.2 Configurations, magnetic materials and electrical circuit parameters of the reference motor
TABLE 3.3 Winding parameters for CW-SynRM
TABLE 3.4 Total losses (neglecting mechanical losses)
TABLE 3.5 Winding parameters for DW-SynRM
TABLE 3.6 Total losses (neglecting mechanical losses)
TABLE 3.7 Performance comparison for different slot/pole combination
TABLE 3.8 Best stator design obtained from the Pareto-front

TABLE 3.9 Equivalent conductors for the chosen design
TABLE 3.10 10 12 2D versus 3D FEA Iron losses
TABLE 3.11 Active material weights and their costs
TABLE 4.1 Mechanical properties of M800-50A
TABLE 4.2 Modal validation Numerical Vs Experimental
TABLE 4.3 The design data of the stator core
TABLE 5.1 CW-SynRM performance resume
TABLE 5.2 DW-SynRM performance resume
Table 1A Stator geometrical parameters
Table 2A Rotor geometrical parameters
Table 3A Considered parameters in the optimization loop along with their bounded values

APPENDICES

A. Parametric 2D FEM and optimization process

The numeric field computation by means of FEA can be done by using dedicated software packages with integrated libraries for different fields domains. Nowadays, there are several software packages that are available on the market, as Flux 2D and 3D, Motor-Cad, JMAG, ANSYS Maxwell, etc. In this thesis, the non-linear behavior of the SynRM was entirely studied via transient simulations, using ANSYS Maxwell software.

As a first step, the geometry of the electrical machine taken into study needs to be drawn. There are two different ways to do it. A first approach is to use direct the graphical editor from the FEA software package or it can be done by scripting the design (using iron Python) and then run the script in ANSYS (developing a FEA parametrized model). In both cases the entire structure is parametrized but depends on the user how to implement it. Considering the dimensional variables given in the cross section of the SynRM shown in Fig. A1, A2, it is very easy to modify the topology of the machine if any geometrical limitations (space constraints) or any other changes are imposed.

Designing a FE parametrized model opens the opportunity to include the created model into geometry optimization loops, so as to optimize the motor topology in terms of torque performance (e.g. high average torque, low torque ripple content), minimize the machines mass or even materials cost reduction. The same geometrical parameters are used for all the topologies that will be analyzed in this thesis. For a better understanding the optimization process will be performed on one SynRM structure. The geometric design parameters given in the next figure are used to create FE parameterized structure of the SynRM. The example given is for a 12 slots 4 poles, concentrated winding design. Both geometrical parts stator (a) and rotor (b) are described in Table 1A and 2A, as follow:

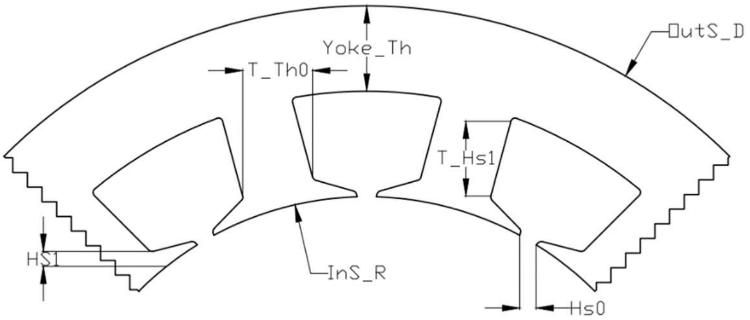

Fig. 1A (a) Stator geometrical parameters in the FE model

Table 1A Stator geometrical parameters

Nr.	Name	Unit	Description
1	OutS_D	mm	Stator outer diameter
2	Yoke_Th	mm	Yoke thickness
3	T_Th0	mm	Tooth thickness
4	T_Hs1	mm	Tooth height
5	Hs0	mm	Slot opening width
6	Hs1	mm	Slot opening height
7	InS_R	mm	Stator inside radius

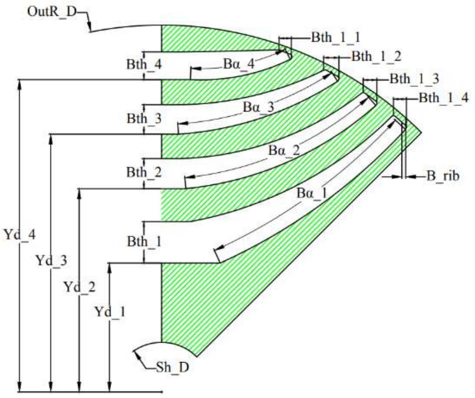

Fig. 2A (b) Rotor geometrical parameters in the FE model

Table 2A Rotor geometrical parameters

Nr.	Name	Unit	Description
1	Bth_1…4	mm	Base barrier thickness
2	Bth_1…4_1	mm	Edge barrier thickness
3	Bα_1…4	deg.	Barrier angle
4	Yd_1…4	mm	Barrier position
5	B_rib	mm	Bridge thickness
6	OutR_D	mm	Rotor outer diameter
7	Sh_D	mm	Shaft diameter

Design Optimization

The key performance characteristics of the SynRM is directly related to the geometry of the machine. Due to the complex rotor structure of this machine, an advanced design optimization based on different techniques [74], [75], [76], [77] is implemented. The main objective of the optimization process is to maximize the average torque while minimizing the torque ripple. As described above, the parametrized design was done in order to integrate the electromagnetic analysis in an optimization loop in respect to different objective functions. An artificial intelligence-based approach using Particle Swarm Optimization (PSO) coupled with FE models is used for the characterization and design optimization for all studied SynRMs. This part of the study will present the optimization process and the obtained results just for the 12 slots 4 –pole SynRM design. The values used for the dimensional parameters mentioned above in this chapter are bounded between an upper limit and a lower limit as shown in Table 3A. The geometrical parameters used in the FE-model are considered as degrees of freedom (DOF) for the optimization process. The importance of each parameter for the geometry will be discussed hereafter.

Table 3A Considered parameters in the optimization loop along with their bounded values

Geometrical parameters	12 slots – 4pole design	
	Lower limit	Upper limit
T_Th0 [mm]	2	5
Hs1 [mm]	0.5	1.5
T_Hs1 [mm]	10	15
Hs0 [mm]	0.5	3
Bth_1 [mm]	2	5
Bth_2 [mm]	2	5
Bth_3 [mm]	2	5
Bth_4 [mm]	2	5
Bth_1_1 [mm]	2	4
Bth_2_1 [mm]	2	5
Bth_3_1 [mm]	2	5
Bth_4_1 [mm]	2	5
Yd_1 [mm]	11	15
Yd_2 [mm]	17	24
Yd_3 [mm]	21	29
Yd_4 [mm]	26	36
Bα_1 [deg]	1	5
Bα_2 [deg]	7	11
Bα_3 [deg]	12	18
Bα_4 [deg]	19	26
B_rib [mm]	0.45	1
OutR_D [mm]	35	41

Fig. 3A shows the proposed optimization procedure where the parametrized FE model is coupled with the optimization algorithm. The implementation was done in Python code in the scripting language of the ANSYS/Maxwell software, which is employed as the FEA computational software.

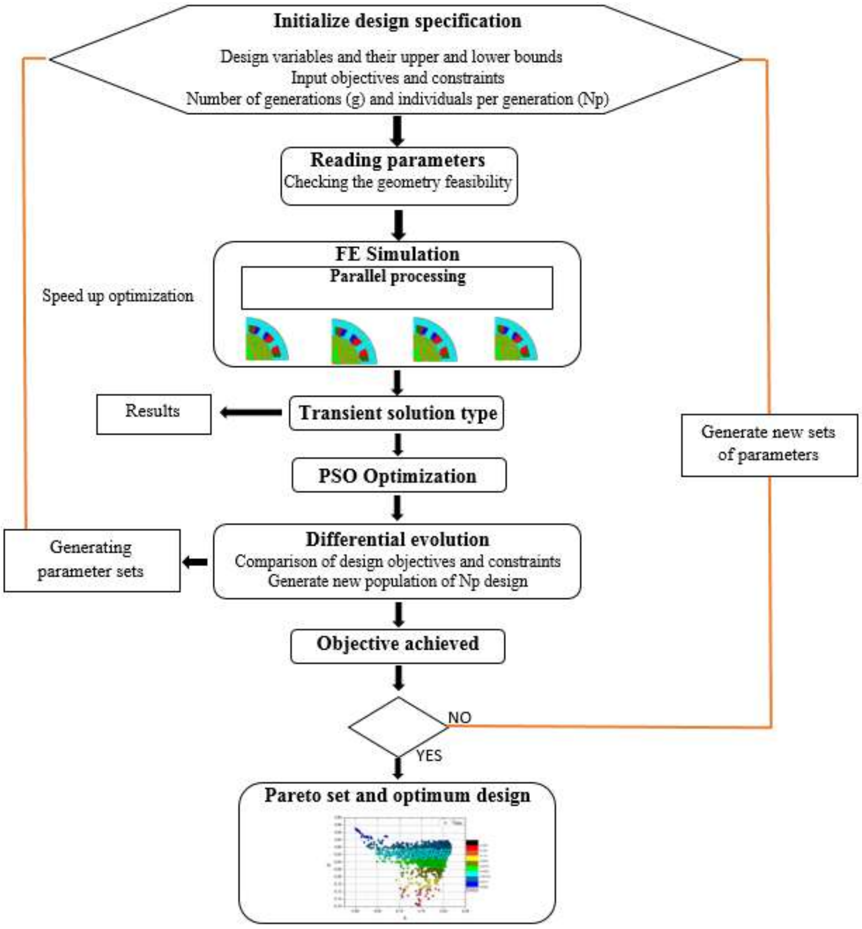

Fig. 3A Flowchart of the optimization process

Before the optimization process starts, the geometrical parameters from the 2D FE model are checked against creating a non-valid model. If a non-valid structure is created the simulation is aborted and new design is created to be analyzed.

A Python script is used to handle this problem by updating the parameters inside the FE design. Further, if the design is feasible from the geometrical point of view, simulations are performed. For a faster computation, parallel processing can be used to speed up the optimization. After the simulations are done, the output results (e.g. average torque, torque ripple) are sent to the optimization software (OptisLang). Here, a comparison of design objectives and constrains is performed and further generates the parameter sets. There is a large variety of optimization algorithms that can be used to perform such an operation, but in this case particle swarm optimization algorithm technique is employed.

PSO is an evolutionary computation technique algorithm developed by Kennedy and Eberhart in 1995 [78]. This technique mimics the behavior of a flock of birds where the information is spread among the individuals of the population.

Before the optimization process starts, a set of sensitivity analysis needs to be done in order to evaluate the influence of each parameter on the SynRM structure. The main goal of this analysis is to find the most significant geometrical parameters of the rotor and stator structure that affect the machine torque capability. Scatter plots of more than 2000 candidates (simulations) can be seen in Fig. 4A, where Pareto-front sensitivity analysis for different geometric parameters is presented.

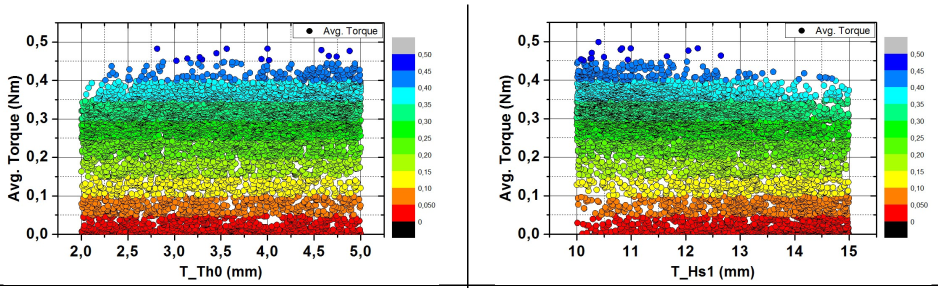

(a) Sensitivity analysis for Tooth thickness

(b) Sensitivity analysis for Tooth height

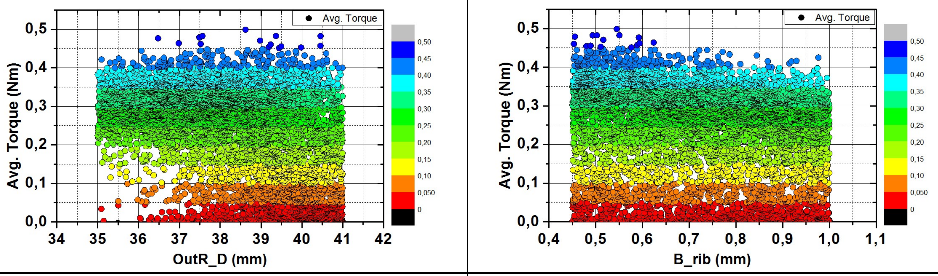

(c) Sensitivity analysis for Outer Rotor Diameter

(d) Sensitivity analysis for Bridge thickness

Fig. 4A Pareto front sensitivity analysis for different geometric parameters with impact on the motor structure

This method is efficient to find out the influence of each parameter on motor performance. Thus, it can be stated that the rotor outer diameter and the tooth height have a 100 % influence, and the tooth thickness and the bridge thickness have 67 % according to sensitivity analysis results.

Throughout the optimization process, the machine length, the outer diameter and the winding current density have been maintained constant. One hundred generations, each one with 100 individuals, have been considered in the PSO algorithm, resulting 10,000 candidate design for 12 slots 4 pole topology. The same parameters as the previous study are analyzed, but this time PSO is applied. The obtained results are plotted in Fig. 5A.

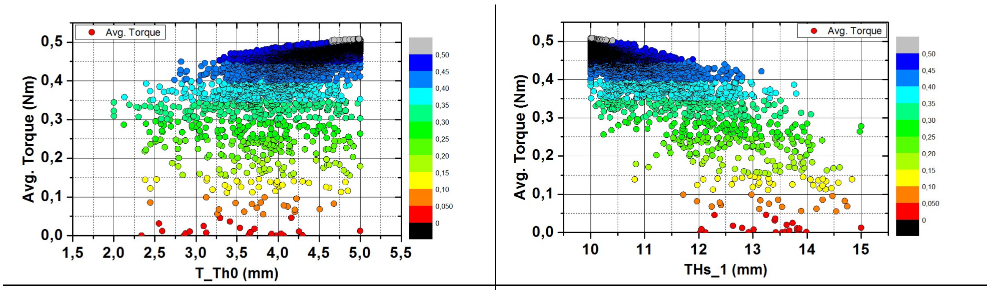

(a) PSO for Tooth thickness

(b) PSO for Tooth height

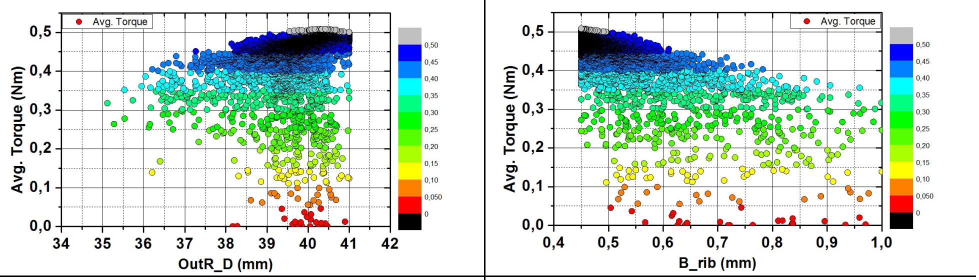

(c) PSO for Outer Rotor Diameter

(d) PSO for Bridge thickness

Fig. 5A Scatter plot of 10.000 candidate optimized with PSO quantifying the improvements of SynRM

Based on the graphs it can be stated that to achieve a higher torque density, the outer rotor diameter should vary between 39 mm to 41 mm where the maximum torque is obtained. Moreover, the tooth thickness reaches the maximum upper limit value, between 4.5 to 5 mm. Decreasing the tooth height makes directly to increase the yoke thickness which it leads to a lower saturation level present in stator structure.

From the electromagnetic point of view, the bridge thickness should have the smallest value as possible in order to reach the saturation level in a short time. But at the same time it has to ensure the rotor robustness to achieve a good mechanical behavior. To avoid any mechanical problems, the lower limit of the bridge was imposed to 0.5 mm.

A further study was focused to see the influence of the flux barriers design on the average torque of the machine, see Fig. 6A. The most important parameters that defines a flux barrier have been considered in this optimization process.

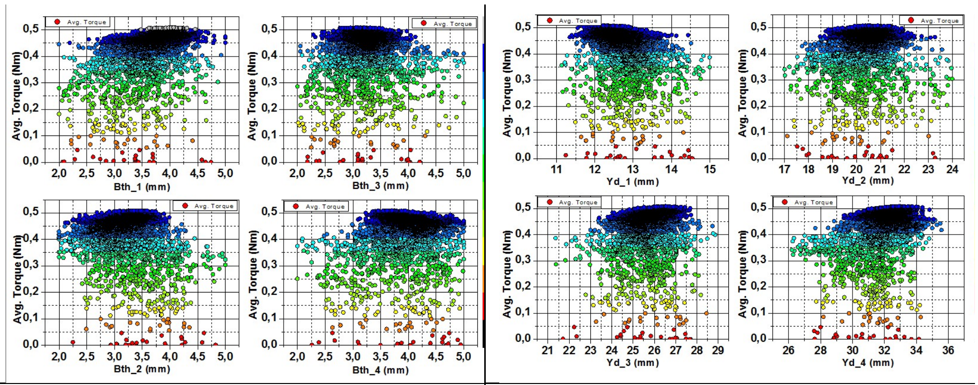

(a) PSO for the base flux barrier thickness

(b) PSO for the flux barrier position

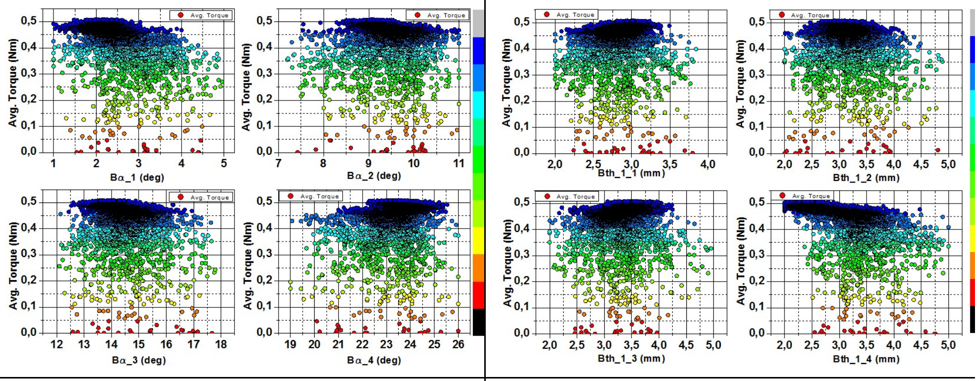

(c) PSO for the base flux barrier angle

(d) PSO for the edge flux barrier thickness

Fig. 6A Pareto front of flux barriers parameters optimized with PSO

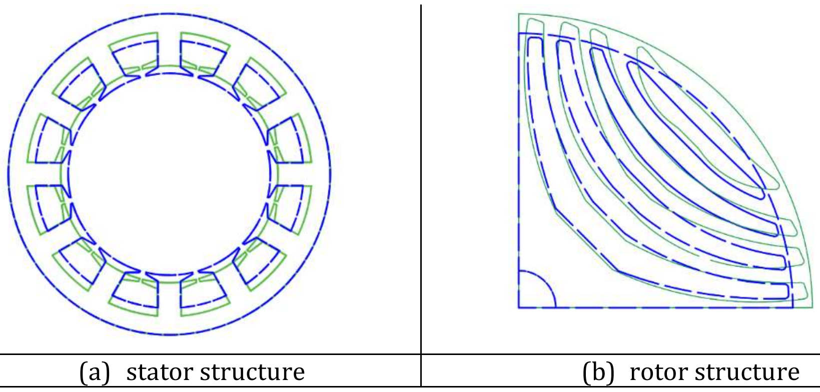

(a) stator structure

(b) rotor structure

Fig.7A SynRM geometries obtained before (green line) and after optimization process (blue dotted line)

The obtained electromagnetic torque vs speed characteristic for the initial pre-design and the optimized design of the SynRM topologies are shown in Fig. 8A (a).

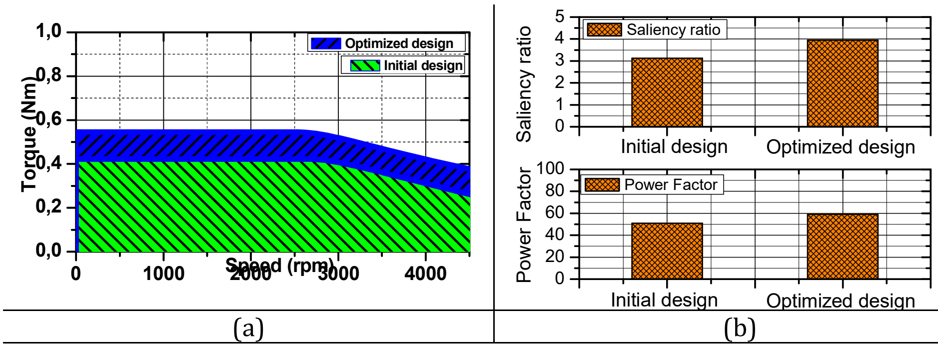

(a)

(b)

Fig.8A (a) Torque vs Speed characteristic - plotted area of the initial and optimized design

(b) Saliency ratio and power factor comparison

As it can be seen, the average torque developed by the initial SynRM was rather low, 0.42 Nm. Hence, after PSO a significant increase of 20 % torque is reported. Keeping the same electrical input values and geometrical constraints (outer diameter and stack length) the reason can be explained through the Fig. 8A (b), which represents the effect of the rotor and stator design on the machine saliency ratio. Also, the machine power factor is strongly depended to inductances ratio, saliency ratio (L_d/L_q).

LIST OF PUBLICATIONS

Year 2014

1. **F.P. Pop,** Claudia Martis, Florin Jurca, Claudiu Oprea,“Permanent magnet synchronous machine design for low-noise drive systems”, *“International Conference on Noise and Vibration Engineering” ISMA, Leuven, Belgium 2014.*

2. Jurca, F. N., Mircea, R., Martis, C., Martis, R., & **F.P. Pop.** ,“Synchronous reluctance motors for small electric traction vehicle*” Electrical and Power Engineering (EPE), 2014 International Conference and Exposition on (pp. 317-321). IEEE.*

Year 2016

3. **F. P. Pop**, R. Marţiş, A. Dărămus, C. Marţiş, A. C. Pop and I. Vintiloiu, "Design and analysis of slot-pole combination for synchronous reluctance machine with concentrated windings for automotive applications," *2016 International Conference and Exposition on Electrical and Power Engineering (EPE), Iasi, 2016, pp. 229-234.*

Year 2017

4. **F. P. Pop**, D. C. Popa, R. Marţiş, C. Marţiş and A. C. Pop, "Comparative analysis of rare earth-less electrical machines for 48V automotive cooling fan applications," *2017 14th International Conference on Engineering of Modern Electric Systems (EMES), Oradea, 2017, pp. 180-183*

5. **F.P. Pop**, A.C. Pop, R.Martis, I. Vintiloiu, and C. Martis, “Synchronous Reluctance Motor vs. Permanent Magnet Synchronous Motor Comparative Study for Automotive Applications”,*17th International Conference on Energy Efficiency in Motor Driven Systems EEMODS’17, Rome, Italy, 2017.*

Year 2018

6. M. Ruba, , R. Nemes, **F.P. Pop**, C. Martis, “Complete electric power steering system real-time model in the loop simulator”, *12th Internationl Conference ELEKTRO 2018, 21-23 May, Mikulov, Czech Republic.*

7. M. Ruba, **F.P. Pop**, R. Nemes, H. Hedesiu, C. Martis, “Comparison of electric power steering assistant motor structures using real-time model in the loop analysis”, *International Conference on Automation, Quality and Testing, Robotics AQTR 2018, 24-26 May, Cluj-Napoca, Romania.*

8. **F.P. Pop**, M. Ruba, R. Nemes, A.C. Pop, C. Martis, “Real-time Model in the Loop analysis of PMSM for electric power steering system based on FPGA implementation” *2018 International Symposium on power Electronics, Electrical Drives, Automation and Motion, SPEEDAM 2018, Amalfi, Italy, 2018.*

9. **F.P. Pop**, M. Ruba, A.C. Pop, R. Martis, C. Martis, “Comparative analysis for an electric power steering system” *XXIIIrd International Conference on Electrical Machines (ICEM'2018), Alexandroupoli, Greece,2018.*

10. **F.P. Pop**., Martis, R., Martis, C., Faria, C., & Chauvicourt, F. (2018, October). Electromagnetic and NVH study for low power Synchronous Reluctance Machine. In *2018 AEIT International Annual Conference*,Italy

11. A. Pop, **F.P. Pop**, R. Martis, I. Vintiloiu and C. Martis, "First Insights on the Electromagnetic Design of Axial-Flux Synchronous-Reluctance Maschine," *IECON 2018 - 44th Annual Conference of the IEEE Industrial Electronics Society, Washington, DC, 2018, pp. 5702-5709. doi: 10.1109/IECON.2018.8591235*

12. A. Pop, T. Rusu, R. Martis, **F.P. Pop**, I. Vintiloiu and C. Martis, "Optimal Design of SRMs for Comparable Output with PMSMs," *IECON 2018 - 44th Annual Conference of the IEEE Industrial Electronics Society, Washington, DC, 2018, pp. 5716-5722. doi: 10.1109/IECON.2018.8591049*

13. R. Marţiş, **F.P. Pop**, C. Marţiş, L. Szabo and M. Ruba, "Design and Optimization Platform for Synchronous Motors," 2018 *International Symposium on Power Electronics, Electrical Drives, Automation and Motion (SPEEDAM), Amalfi, 2018, pp. 314-318. doi: 10.1109/SPEEDAM.2018.8445210*

Year 2019

14. Văscan, I., **F.P. Pop**, Marţiş, C., & Bârsan, I. (2019, October). PMSM Rotor Topologies for Automotive HVAC System. *In 2019 Electric Vehicles International Conference (EV) (pp. 1-4). IEEE.*

15. Radu, R., Popa, D. C., Piglesan, F. P., & Martis, C. (2019, March). Electrical Machines for Mobile Charging Station Propulsion Systems–Comparative Study. *In 2019 11th International Symposium on Advanced Topics in Electrical Engineering (ATEE) (pp. 1-6). IEEE.*